AFRL-VS-HA-TR-2008-1139

Investigation of Plasma Phenomena in the Ionosphere Under Natural Conditions and Under Conditions Artificially Perturbed by *HAARP*

James A. Secan
L. J. Nickisch
Dennis L. Knepp
A. Lee Snyder
Edward J. Kennedy

NorthWest Research Associates, Inc.
4118 148th Ave NE
Redmond, WA 98052

Final Report

31 August 2008

AIR FORCE RESEARCH LABORATORY
Space Vehicles Directorate
29 Randolph Road
AIR FORCE MATERIEL COMMAND
Hanscom AFB, MA 01731-3010

AFRL-RV-HA-TR-2008-1139

This technical report has been reviewed and is approved for publication.

/ signed /	/ signed /
James C. Battis	Dwight T. Decker, Chief
Contract Manager	Space Weather Center of Excellence

This report has been reviewed by the ESC Public Affairs Office (PA) and is releasable to the National Technical Information Service (NTIS).

Qualified requestors may obtain additional copies from the Defense Technical Information Center (DTIC). All other requestors should apply to the National Technical Information Service (NTIS).

If your address has changed, if you wish to be removed from the mailing list, or if the addressee is no longer employed by your organization, please notify AFRL/RVIM, 29 Randolph Road, Hanscom AFB, MA 01731-3010. This will assist us in maintaining a current mailing list.

Do not return copies of this report unless contractual obligations or notices on a specific document require that it be returned.

REPORT DOCUMENTATION PAGE

Form Approved
OMB No. 0704-0188

1. REPORT DATE *(DD-MM-YYYY)*	2. REPORT TYPE	3. DATES COVERED *(From - To)*
31-08-2008	Final Report	18-08-2005 to 31-07-2008

4. TITLE AND SUBTITLE

Investigation of Plasma Phenomena in the Ionosphere Under Natural Conditions and Under Conditions Artificially Perturbed by *HAARP*

5a. CONTRACT NUMBER
FA8718-04-C-0001

5b. GRANT NUMBER

5c. PROGRAM ELEMENT NUMBER

6. AUTHOR(S)

J.A. Secan, L. J. Nickisch, D. L. Knepp, A.L. Snyder, E. J. Kennedy

5d. PROJECT NUMBER
4827

5e. TASK NUMBER
HR

5f. WORK UNIT NUMBER
A1

7. PERFORMING ORGANIZATION NAME(S) AND ADDRESS(ES)

NorthWest Research Associates, Inc.
4118 148th Ave NE
Redmond, WA 98052

8. PERFORMING ORGANIZATION REPORT NUMBER

NWRA-BELL-05-R376

9. SPONSORING / MONITORING AGENCY NAME(S) AND ADDRESS(ES)

Air Force Research Laboratory
29 Randolph Road
Hanscom AFB, MA 01731-3010

10. SPONSOR/MONITOR'S ACRONYM(S)

AFRL/RVBXI

11. SPONSOR/MONITOR'S REPORT NUMBER(S)
AFRL-RV-HA-TR-2008-1139

12. DISTRIBUTION / AVAILABILITY STATEMENT

Approved for Public Release; Distribution Unlimited.

13. SUPPLEMENTARY NOTES

14. ABSTRACT

During the report period, NorthWest Research Associates (NWRA) conducted ionospheric measurements at several Air Force research and operational locations and analyzed the data collected thereby. The measurements were performed using a variety of radiowave techniques, most involving transionospheric radio propagation, and included observations of ionospheric perturbations via high-power transmissions under the High frequency Active Auroral Research Program (HAARP). Total Electron Content (TEC) from a chain of stations in Alaska were inverted tomographically to produce altitude versus latitude images of plasma density. By these and other means, ionospheric features such as the main F-layer trough and polar patches were characterized for application to Air Force environmental models. Studies of ionospheric scintillation focused on the performance of models for scintillation were conducted. A number of studies were undertaken to develop better means of partitioning GPS TEC data in altitude and to assess uncertainties in TEC derived from GPS observations.

15. SUBJECT TERMS

Ionosphere, Ionospheric tomography, Total Electron Content (TEC), Ionospheric scintillation, Incoherent Scatter Radar (ISR), Riometer, Auroral ionosphere, Global Positioning System (GPS)

16. SECURITY CLASSIFICATION OF: None			17. LIMITATION OF ABSTRACT	18. NUMBER OF PAGES	19a. NAME OF RESPONSIBLE PERSON
a. REPORT	b. ABSTRACT	c. THIS PAGE			Mr. James Battis
U	U	U	SAR		19b. TELEPHONE NUMBER *(include area code)* 781-377-4669

Standard Form 298 (Rev. 8-98)
Prescribed by ANSI Std. Z39.18

Contents

Figures

Tables

Preface and Acknowledgements

This report summarizes work completed during the period 18 August 2005 through 31 July 2008 on a project to investigate ionospheric plasma phenomenology in both the naturally occurring and artificially stimulated ionosphere. Most of the observations were made at, or in conjunction with, the High-frequency Active Auroral Research Program (HAARP) facility located near Gakona, AK. This work was completed by employees and consultants of NorthWest Research Associates, Inc. (NWRA).

In addition to the authors listed on this report, other contributors of material for this report and contributors to the activities described in this report include NWRA employees John Begenisich, Mark Begenisich, Eric Collins, Andrew Mazzella, Jr., Susan Rao, and student interns Troy Lawlor and Haley Crow, as well as NWRA consultants Elizabeth Holland, Spencer Kuo, William Gordon, John Rasmussen, Allan Schell, Jens Ostergaard, and J. Francis Smith.

1. INTRODUCTION

Under this contract, Northwest Research Associates (NWRA) is performing measurements of the ionosphere in order to investigate plasma phenomena in both the natural ionosphere and in the ionosphere perturbed by the High-frequency Active Auroral Research Program (HAARP) high-frequency heater. The research being conducted falls within Hanscom Technical Areas 3(a), "Ionospheric Effects Research and Department of Defense Systems," and 3(b), "Ionospheric Research Technology," of the Broad Agency Announcement VS-03-01 released by the Air Force Research Laboratory (AFRL).

As a contribution to Technical Area 3(b), we collaborated with scientists and engineers from AFRL, the Naval Research Laboratory (NRL), and other research organizations in the application of diagnostic instrumentation to HAARP. Among the HAARP instruments that we applied to ionospheric research are four NWRA ITS10S coherent radio receiving systems for measuring relative Total Electron Content (TEC) and recording scintillation, a mobile NWRA ITS30m coherent radio receiving system for recording TEC and scintillation in support of HAARP campaign activities, and an Ashtech Model Z-FX GPS receiver for measuring absolute TEC. TEC from these instruments, and phase-scintillation records from the ITS10S receivers, are posted on the HAARP web site for telescience applications and for decision-making during active experiments, and the TEC data were inverted using NWRA's tomography software to produce images of the F layer over Alaska, with the resulting images posted on the HAARP web site. Research topics under the foregoing objectives are reported in Section 2 and Appendixes A, B, and C.

In Technical Area 3(a), topics of research were (1) studies pertinent to improvement of ionospheric scintillation models, (2) various tasks focused on developing techniques for partitioning ionospheric TEC derived from GPS measurements into ionospheric and plasmaspheric content and employing them to study the behavior of the plasmapause and plasmaspheric TEC using GPS measurements of TEC, and (3) studies of the sources and magnitude of uncertainty in TEC derived from GPS measurements. Research topics under the foregoing objectives are reported in Section 3.

Note that work accomplished during the period 17 February 2004 through 17 August 2005 were covered by Scientific Report No. 1 (*Secan et al.,* 2005). Materials presented in that report will not be repeated here with the exception of changes that have been made during the work completed since the end of that report. We will refer to that report as SR1 in this document.

2. HAARP TOPICS – TECHNICAL AREA 3(B)

Under this contract, NWRA coordinated installation of enhanced diagnostic instrumentation and participated in research employing some of them. Our activities aimed at enhancing HAARP diagnostics were carried out primarily by NWRA consultants A. Lee Snyder, Edward J. Kennedy, Jens Ostergaard, and Spencer Kuo. NWRA also employed two summer student interns, Mr. Troy Lawlor and Ms. Hayley Crow, who worked with AFRL personnel at Hanscom AFB and at the HAARP site.

2.1. Summary of HAARP Data Collection Activities

NWRA's HAARP research activities centered on collection and analysis of transionospheric radiowave data. Transmission of two or more phase-coherent radio signals from satellites above the ionosphere to receivers on the ground permits measurement of the path integral of plasma density (so-called total electron content, or TEC) through the ionosphere. TEC is proportional to the dispersive (differential) phase between the two signals (and, with less precision but greater certainty, to differential group delay). Recording of rapid fluctuations in dispersive phase and in received signal strength yields measurement of trans-ionosphere radiowave scintillation.

Under this contract, NWRA measured TEC on slowly moving paths penetrating the entire ionosphere by recording dispersive phase and differential group delay registered on signals transmitted from satellites of the Global Positioning System (GPS) to Gakona, AK. We also measured both TEC and scintillation on paths between satellites moving rapidly over Alaska in high-inclination, low-earth orbits (LEO) just above the main ionospheric (F) layer and several ground stations. Collection and analysis of the LEO data sets is presented in Section 2.1.1., and collection and analysis of the GPS data sets is presented in Section 2.1.2. All of the data and displays described in these two sections are archived on either the HAARP computer network at the HAARP facility near Gakona, AK, or on servers at NWRA's Bellevue office.

2.1.1. LEO Satellite and Tomography Data Sets

NWRA operates NWRA ITS10S receiver systems at four sites in Alaska in support of HAARP operations: Cordova, Gakona (at the HAARP facility), Delta Junction, and Arctic Village. In addition, we obtain data from two University of Texas at Austin (UTA) CIDR receivers operated by the University of Alaska Geophysical Institute (UAF GI) at two sites in Alaska: Ft. Yukon and Kaktovik. Figure 1 shows the locations of these sites on a map of Alaska. The site at Arctic Village was established during the current contract, and is an important additional site in the tomography chain. Data from LEO satellite passes collected at NWRA's four sites are all displayed in this format on the HAARP web site, accessible through that site's Data Index page.

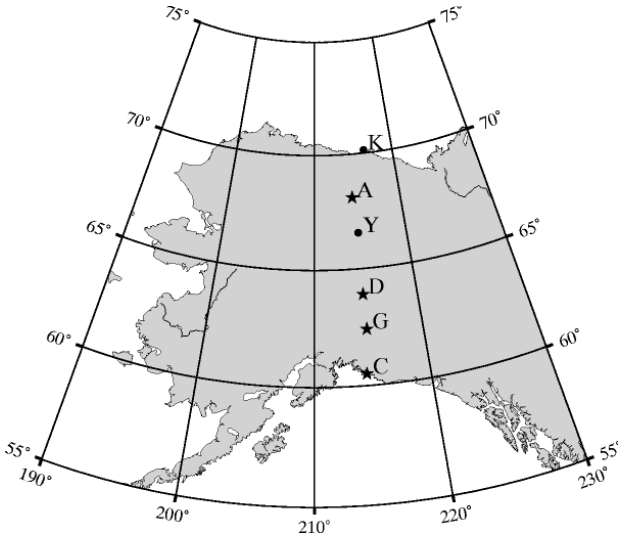

Figure 1. Location of LEO receiver sites in Alaska. Sites indicated by stars (C: Cordova, G: Gakona, D: Delta, A: Artic Village) have NWRA ITS10S receivers. Sites indicated by circles (Y: Ft. Yukon, K: Kaktovic) have UTA CIDR receivers.

Data from these sites are transferred to both HAARP facility computers and to NWRA's Bellevue office for generation of displays as shown in Figure A1 and tomographic analyses. Descriptions of the tomographic processor used to generate images and the criteria used to select passes for tomographic analysis can be found in *Andreasen et al.* (2004) and *Fremouw et al.* (1992, 1994). The implementation of the processing algorithms and the associated data preprocessing was described in detail in SR1, and examples of the various products (data files and displays) generated during the processing were also described in that document.

Under the present contract, we produced 7,772 images from LEO passes over the HAARP tomography chain covering the interval 15 February 2004 through 31 July 2008, all of which were posted on the HAARP web site. Tables summarizing the image coverage over this period can be found in Appendix A.

One change of significance that has been made to the tomography analyses posted on the HAARP Web site is the inclusion of (a) estimates of uncertainty in the plots of TEC and f_oF2 derived from the tomography images, and (b) observations of f_oF2 from the Gakona and College Digisondes when they are available at times near the image time. The uncertainty bars are based on the algorithm described later in this report. Figure 2 is an example of the tomography results as they are now plotted on the HAARP web site showing these new additions. The asterisks on the f_oF2 plot section of the figure are from the Gakona and College Digisonde (from left to right on the figure). The times given are the times the ionograms were made for the different f_oF2 estimates.

2.1.2. GPS Data Sets

NWRA operated an Ashtech Z-FX Continuously Operating Reference Station (CORS), consisting of a 12-channel GPS receiver and an antenna, at the HAARP Gakona facility for the entire period covered by this report. Data collection is performed by means of the NWRA GPS Ionospheric Observation System (GIOS) program, supplemented by a real-time process to convert raw data records from the GIOS software into calibrated estimates of equivalent vertical TEC (VTEC) using the SCORE (Self-Calibration of Range Errors) process developed by NWRA for the USAF Ionospheric Measuring System (IMS) instruments (*Bishop et al.*, 1995). These data are stored in a database and are used to generate plots of absolute TEC displayed on the HAARP Web site. Examples of the products generated in this processing were given in SR1.

In addition to the Ashtech Z-FX system, NWRA also operates a GPS-based CNS clock as a time standard for the NWRA ITS10S receiver located at Gakona. This clock uses a single-frequency GPS receiver chip set that can also provide estimates of the receiver location. We use these data to measure the position error in these estimates by comparing the instantaneous position estimates to estimates derived from long-term averages of the receiver location. The departures of the instantaneous positions from the average positions, both in the horizontal and vertical directions, are shown in the plots. These plots show up to 36 hours of data, and the horizontal data are fitted by an rms-based error ellipse.

All of the GPS data described in this section are archived at either the HAARP site or on servers at NWRA's Bellevue office.

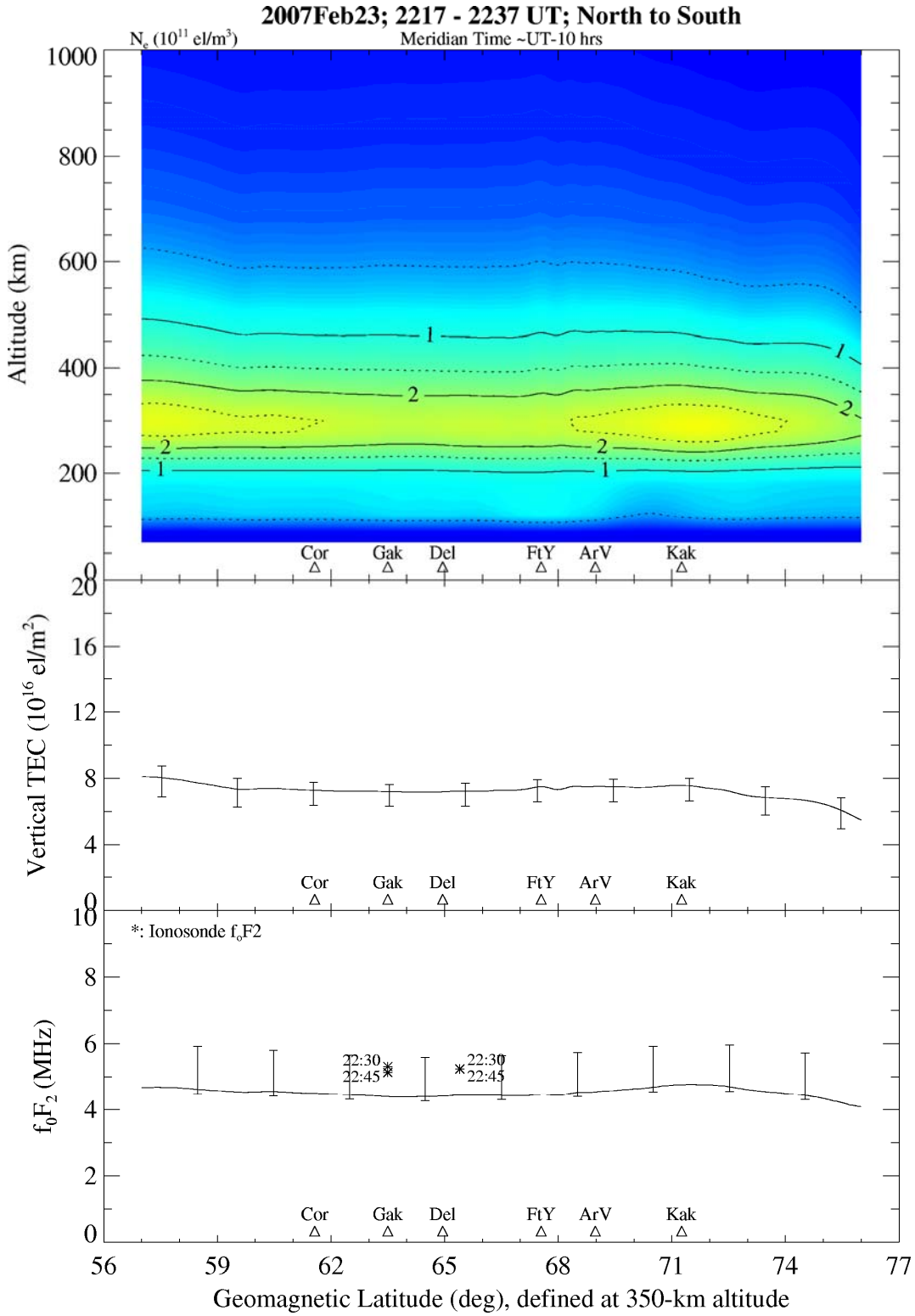

Figure 2. Sample updated tomography output graphic. The top panel shows the tomography-derived electron density latitude-by-altitude map across eastern Alaska, the center panel the vertical TEC calculated from the electron-density profiles output by the tomography processor, and the lower panel is the f_oF2 estimates from the profiles.

2.1.3. Mobile LEO Satellite Receiver System

The NWRA ITS30m Receiver System was conceived as a mobile system wherein the user could operate from an ordinary SUV-type vehicle, and program the sample rate. The concept was to modify the current NWRA ITS30 receiver design as little as possible to allow for mobile operations. The system is also designed for variable data collection rates to allow a wider range of application, particularly for observing small-scale ionospheric irregularities.

Variable Sample-Rate Design

Current series of ITS receivers have a fixed sample rate of 50 Hz. One of these was modified to allow for collection of data at a 2,000-Hz rate, but that was a breadboard implementation rather than a design modification. It is simple to adjust the sample rate from a computer, as the A/D card used to digitize the input analog data stream is under computer control. However, as in any data sampling scheme, the analog signal to be digitized must be filtered to prevent aliasing. In the case of a 50-Hz sample rate, the filter is a 25-Hz 4-pole low-pass filter. The design effort, then, was to adjust the cutoff frequency of the anti-aliasing filter at the same time as the digitizing rate was changed.

The central component in this design is a digitally controlled potentiometer (pot). The filter parameters are set with capacitors and resistors, and so a digitally controlled resistor can be used to affect the necessary tuning. This was done in three steps:

1. Identify a digital pot that would work at the voltages present in the existing circuit. Many digital pots are available, but the great majority of them work at 5 volts whereas the existing circuit works at +/- 15 volts. One such pot was found from MAXIM, an electronic component manufacturer.

2. Change the component values of the remaining resistors and capacitors in the filter so that the filter characteristics (the 'shape' of the filter cutoff) would remain the same at any value of the digital pot. This was accomplished with the aid of a circuit simulation program from Linear Technology, a leading semiconductor manufacturer.

3. Rework the circuit board artwork to accommodate the new design.

With a few sample boards fabricated, the concept was tested, and a number of design defects were discovered, a usual occurrence. The test board was modified with cuts and jumper wires to correct the defects and continue testing until the design was verified. Based on the testing, new artwork was prepared.

Note that this design was specifically adapted to the use of a certain A/D data input card from National Instruments, the 6052E/6024E. This card is in use in all of the existing ITS receiver stations. At about this time, we began to consider that the 6052E/6024E cards had been in production for about 12 years, which is about as long as hardware of this kind is supported by the manufacturer. Discussions with the manufacturer, National Instruments, indicated that the card is a popular one, so that production will likely continue for some time longer, but no firm prediction was made as to how long that would be. In view of the above, it was decided to take another step in the design of the variable-sample-rate system to incorporate a more modern A/D input card, the USB 6009 (also from National Instruments).

The resulting design, now in production, allows the Receiver Detector Module (the item of receiver hardware that is the focus of the variable-sample-rate concept) to be built to interface with either the 6052E or the USB 6009, and to be built with or without the variable-sample-rate feature. The actual receiver, ITS30-15m, is fitted with a Detector configured for variable sampling and the 6024E.

Mobile Operation

By Mobile Operation, we refer to the operation of an ITS system from a vehicle such as an automobile or SUV. To achieve mobile operation, three issues needed to be addressed: the computer, power and the antenna.

1. Mobile Computer. While there is no functional reason why the standard ITS configuration could not be used in a mobile operation, the power consumption and unwieldy physical aspects of having a desktop computer, monitor, keyboard and mouse indicated a better solution. In this we were fortunate that the A/D input card discussed above (6024E) also comes in a PCMCIA version; that is, a version that fits into a special card slot that is standard on most Laptop computers. Therefore, the mobile computer is simply a laptop computer with ITS software and a PCMCIA 6024E installed.

2. Mobile Power. All of the components of the mobile system, receiver, computer and GPS clock, come standard operating from 120 VAC. In another stroke of good fortune, none of these components are overly sensitive to the 'cleanliness' of that power. Therefore, it seemed feasible to create a power system using the host vehicle's 12-volt power system, and a 12-volt DC to 120 VAC power inverter. Such a power inverter was obtained, and the system was tested at the Bellevue laboratory by first operating from 120 VAC from an extension cord, and then operating from the vehicle's 12-volt DC system through the power inverter. No difference was detected and so that inverter system is now in use.

3. Mobile Antenna. There were two aspects to the mobile antenna configuration: the adequacy of having only the vehicle roof as a groundplane and the operational issue of handling the ITS antenna. Originally, it was thought that a large ground-plane structure would need to be fabricated that would fit atop the mobile vehicle. Considering that every campaign in which this system was likely to be deployed would involve a different (rented) vehicle, this was seen as a challenge. It was then observed that ITS receivers operating in Taiwan were consistently using a 1-m x 1-m ground plane. This gives these users an adequate antenna pattern, and gave us the idea that an SUV rooftop might be sufficient. Once again, testing of this idea indicated that at relatively high satellite elevations, the SUV roof ground plane was sufficient.

Handling of the ITS antenna system is awkward because the antenna mast is about 30 inches tall, with four 18-inch elements radiating from the top of the mast structure, four 7-inch elements radiating from a point about 12 inches from the base, and four more 2-inch elements about 4 inches from the base. The solution was to make each of the upper 8 elements into 2 pieces threaded together. In transport, all of the elements project only 2 inches from the center of the mast. When set-up, the upper and middle element sets have appropriately sized element extensions screwed into the 2-inch stubs to form a full-sized antenna. The mast itself is affixed to an 18” x 24” flat aluminum plate which, in turn, is placed on the vehicle rooftop.

Testing and Operation

Three tests of the mobile system were conducted. The first two were developmental testing, and were not intended to have any scientific value. The final test involved mobile operations that were integrated into the science campaign.

The first test was conducted at the HAARP site at a location approximately 50 feet away from the fixed ITS station there. It demonstrated that the concept was sound: the mobile data was roughly similar to the fixed station data. It also revealed a circuit design defect that required further testing at the Bellevue lab to locate and correct. It was at this test that the idea of having the antenna elements be removable was conceived.

The next test was also conducted at the HAARP site environment, this time in actual off-site deployment mode. The receiver performed correctly, but two more operational issues were revealed. The first was that synchronizing the time on the mobile computer to UTC was very awkward and, at best, inaccurate. The solution was to include a GPS clock into the suite of equipment used for the mobile operation. The clock used was the CNS clock that is part of the Bellevue lab station, and a small GPS patch antenna.

The second operational issue was that finding the remote site where the mobile station was to be located was very clumsy using simply a GPS position indicator. To solve this problem, it was necessary to plot the satellite path on a map that also showed the roadways in the vicinity, and then actually visit the remote site location early enough to find a suitable place to pull off of the highway and set up the station. By the last test, the TOPO software package, from National Geographic, was used which allowed the satellite ground path to be plotted on a map, and then the resulting map to be printed out.

The final test was a fully operational part of a science campaign. All the planned sites were located, the station set up and operated, and data collected. In several cases, the satellite that was the subject of observation was either not transmitting, or had an inadequate transmitting antenna pattern. Therefore, not all the data sought was collected or useful. Samples of data collected from this mobile receiver during the campaign will be presented later in this report.

During this final test, another operational issue was discovered. A second ITS30 system, owned and operated by personnel from AFRL, was deployed alongside the NWRA ITS30m system during the campaign. The AFRL system was different in that it was not a variable data rate system, and it made use of a different antenna system than the NWRA system. Otherwise, it had a similar receiver and a laptop computer. The subject operational issue was discovered when the AFRL people placed the antenna LNA/preselector module inside the vehicle. It is normally positioned close to the antenna but, since the antenna was so close to the receiver (in this mobile configuration), the module was brought inside the SUV. In this arrangement, the cables from the antenna to the LNA and the cables from the LNA to the receiver were close together and formed a feedback loop. No signal was detectable under these conditions. (Note that there were other problems with the AFRL receiver, so that system would not have performed well in any case, but the feedback problem was instructive to the future operation of the mobile receiver concept.)

To provide assurance that the feedback situation will not reoccur, and to minimize the feedback signal path, the cable set from the antenna to the LNA was shortened so that the LNA can only be operated in close proximity to the antenna.

Summary

Development of the ITS30m system involved electronic design effort that met the initial goal, variable data rate, and was extended to provide for the use of more modern vendor-supplied equipment in the future. Development also required overcoming several nut-and-bolt operational issues to create a functional system. Figure 3 shows the ITS30m system as completed. Figure 3a shows the system prior to deployment (the open box next to the antenna holds the preamplifier electronics), 3b shows the inside of an SUV at the HAARP site during the February 2008 campaign, and 3c shows an outside view of the SUV illustrating the antenna and preamplifier box, also from the February 2008 campaign.

a. b. c.

Figure 3. The ITS30m system. (a) The entire ITS30m system prior to deployment. (b) The system deployed in an SUV. (c) The antenna and preamplifier box as deployed for pass acquisition.

2.2. Tomographic Imaging of the Auroral E Region

The tomography analysis system used to invert observations of relative TEC from the HAARP receiver chain to obtain altitude-by-latitude maps of ionospheric electron density was developed with a focus on imaging the major features of the F2 and topside ionosphere. While there was anecdotal evidence that the process was capable of producing images that showed realistic structures in the E region, specifically auroral E, we had not taken a systematic look at any specific cases to see if the results were consistent with other observations. In preparing for the February 2008 campaign (discussed elsewhere in this report), we found two tomography images from passes roughly 90 minutes apart that showed a very strong E region in the initial image with a much weaker E region in the second. We have taken a closer look at these two images and compared them with data collected from other HAARP diagnostic instruments during the times of the two passes.

Figures 4 and 5 show the images generated from the data collected by the HAARP tomography chain. Figure 4 is an image generated from an Oscar 32 pass over the time interval 1226-1246 UT on 10 February 2008, and Figure 5 is an image from an Oscar 25 pass over the time interval 1358-1414 UT on 10 February 2008. An intense E-layer stretching from Gakona (Gak) to Arctic Village (ArV) is very evident in Figure 4, with a very weak E-layer over the southern end of this latitude range in Figure 5. The working hypothesis is that the E-layer in Figure 4 is due to very intense auroral precipitation which has weakened markedly by the time of the second pass shown in Figure 5.

The images in Figure 6 are a series of Digisonde soundings take from the Gakona (left column) and College (right column) Digisondes during the times covered by the tomography

images shown in Figures 4 and 5. The soundings start at 1200 UT on 10 February and run in 15 minute steps through 1415 UT, skipping the sounding at 1315 UT (the Gakona 1315 UT sounding is nearly identical to the Gakona 1330 UT sounding, and the College 1315 UT sounding is nearly identical to the College 1300 UT sounding). The soundings prior to 1230 UT show very substantial E layers, followed by three successive soundings where absorption is so high that no discernable echo trace can be found in either sounding. This is during the period of the image in Figure 4, which shows very strong E layers over both Digisondes. The E-layer traces are beginning to return, and by the time of the second pass (Figure 5), the E layer over Gakona has weakened and there is an F2-layer echo beginning to show at a critical frequency of around 3 MHz, which is consistent with the densities shown in Figure 5.

This picture of an intense auroral precipitation event is supported by the data shown in Figures 7 and 8, which are 24-hour plots of the absorption measured by the HAARP 30-MHz classic riometer and the H, D, and Z traces from the HAARP magnetometer. The riometer shows very strong absorption at the time of the first pass (Figure 4), at the same time the magnetometer is showing a large negative bay in the H and Z traces. The riometer absorption has decreased significantly by the time of the second pass (Figure 5), as has the intensity of auroral currents as observed in the magnetometer data. Unfortunately, there were no DMSP passes near the HAARP facility at the time of this event, but data from other longitude sectors showed strong auroral-zone precipitation around the time of the first pass.

We plan to pursue this ability to image the auroral E region with the tomography system in our future work on the new contract.

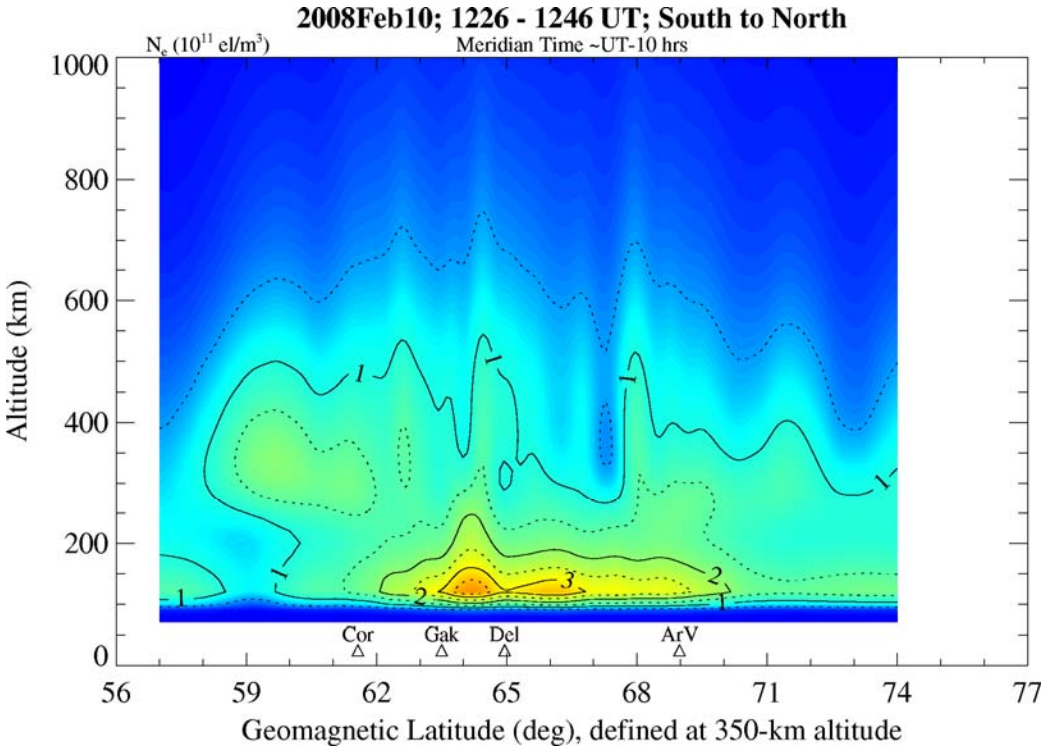

Figure 4. Tomography image, Oscar 32 pass from 1226 to 1246 UT on 10 February 2008.

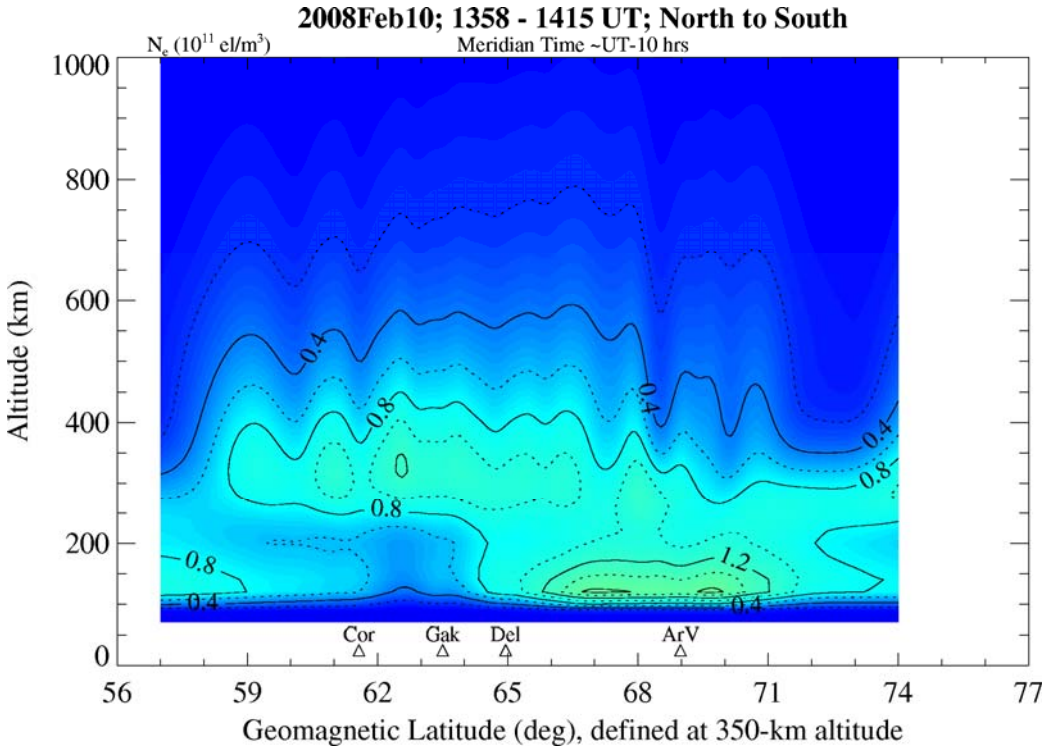

Figure 5. Tomography image, Oscar 25 pass from 1358 to 1414 UT on 10 February 2008.

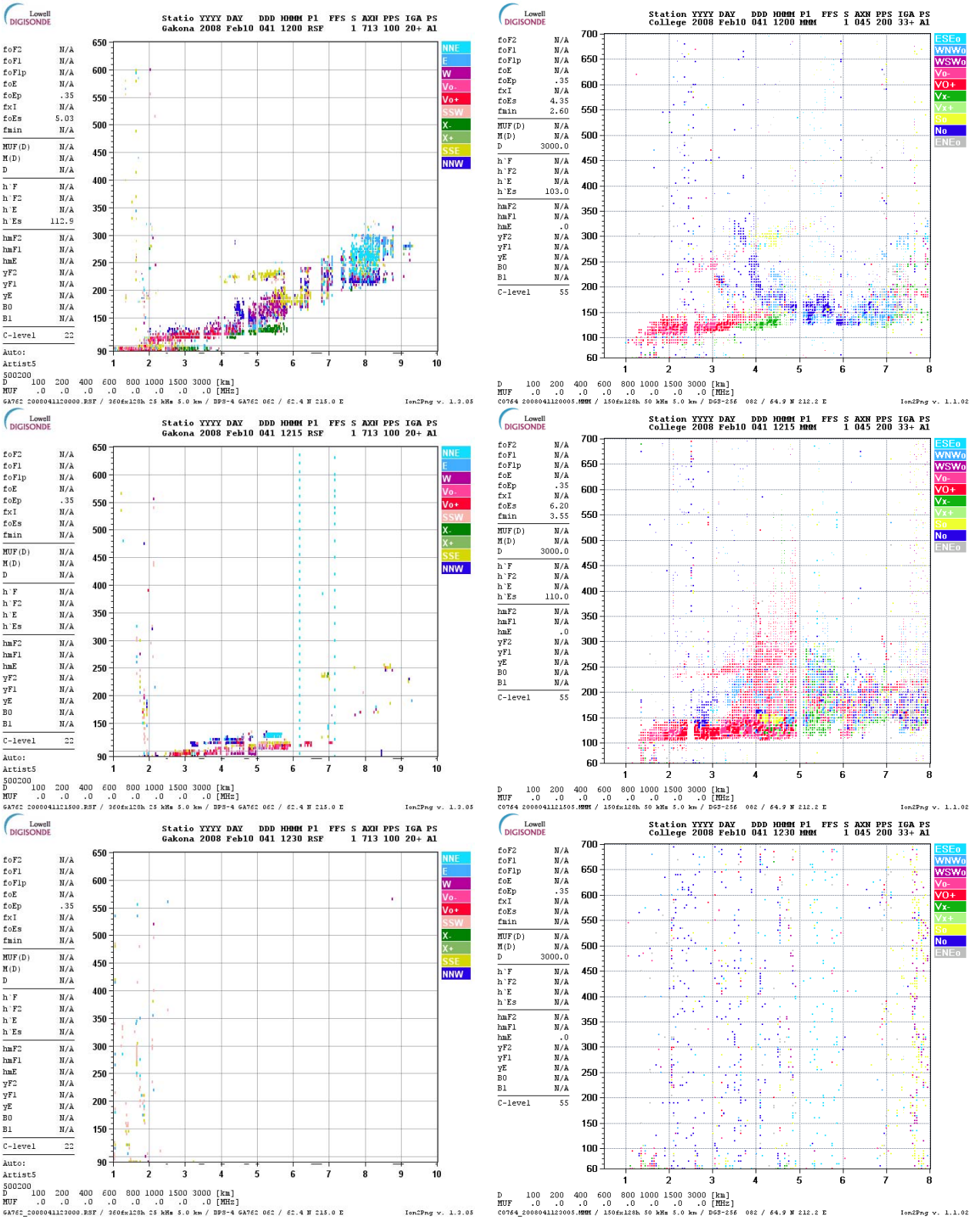

Figure 6. Digisonde soundings from Gakona (left column) and College (right column).

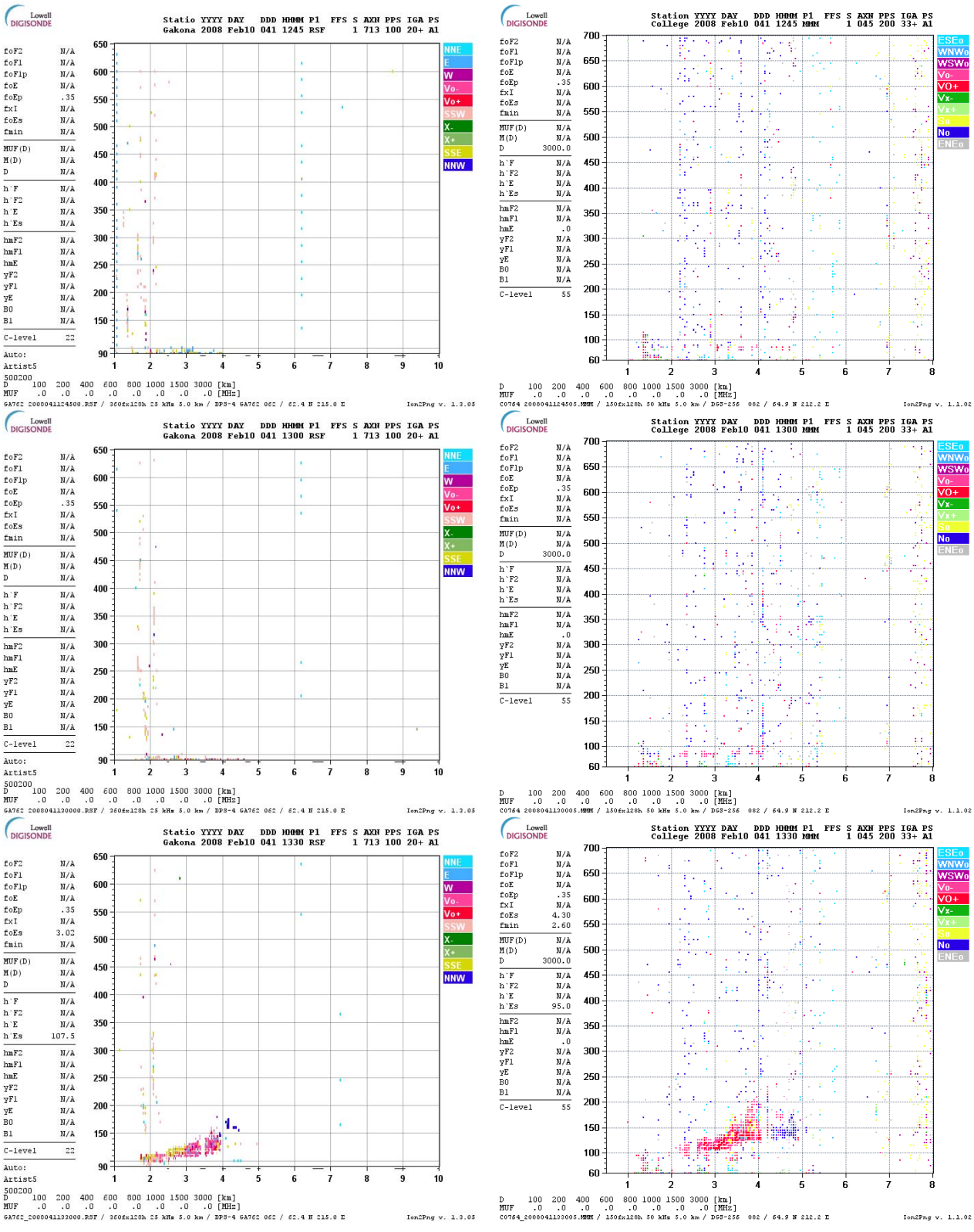

Figure 6. (continued).

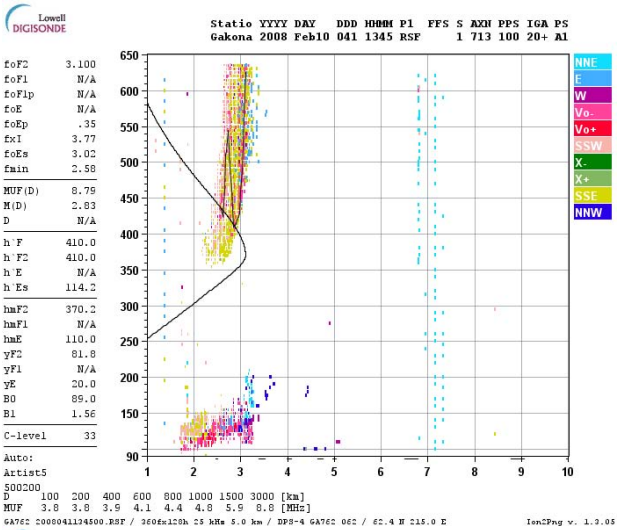

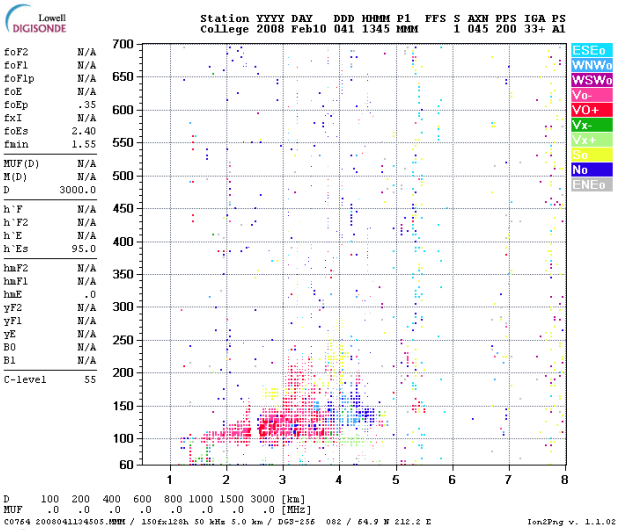

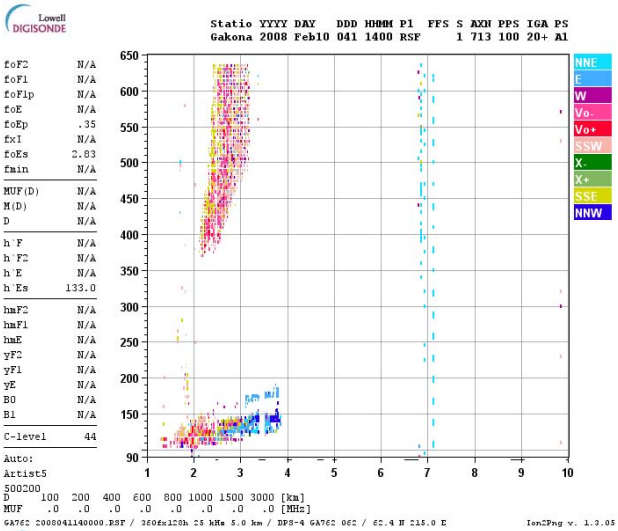

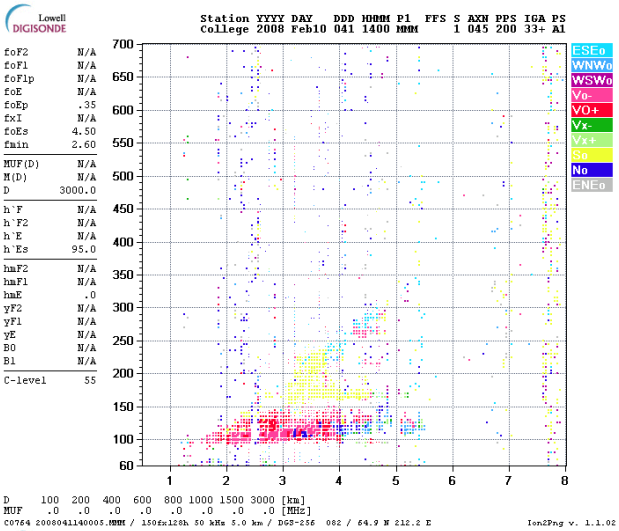

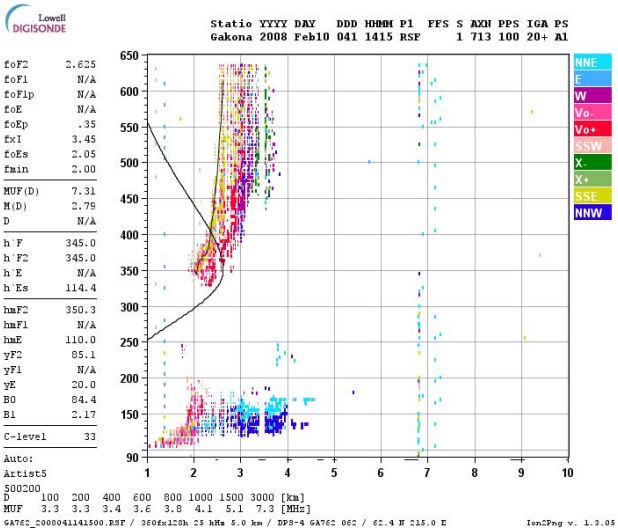

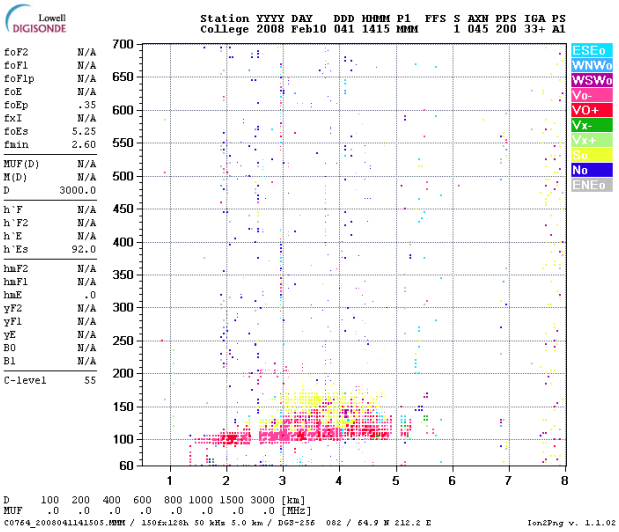

Figure 6. (continued).

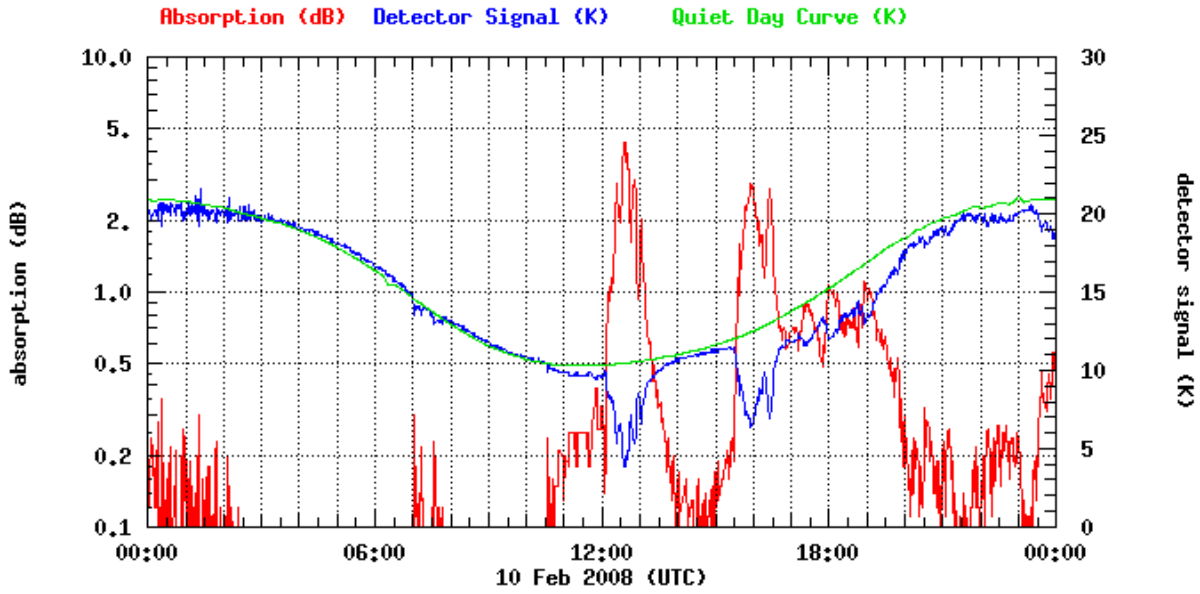

Figure 7. Gakona riometer data.

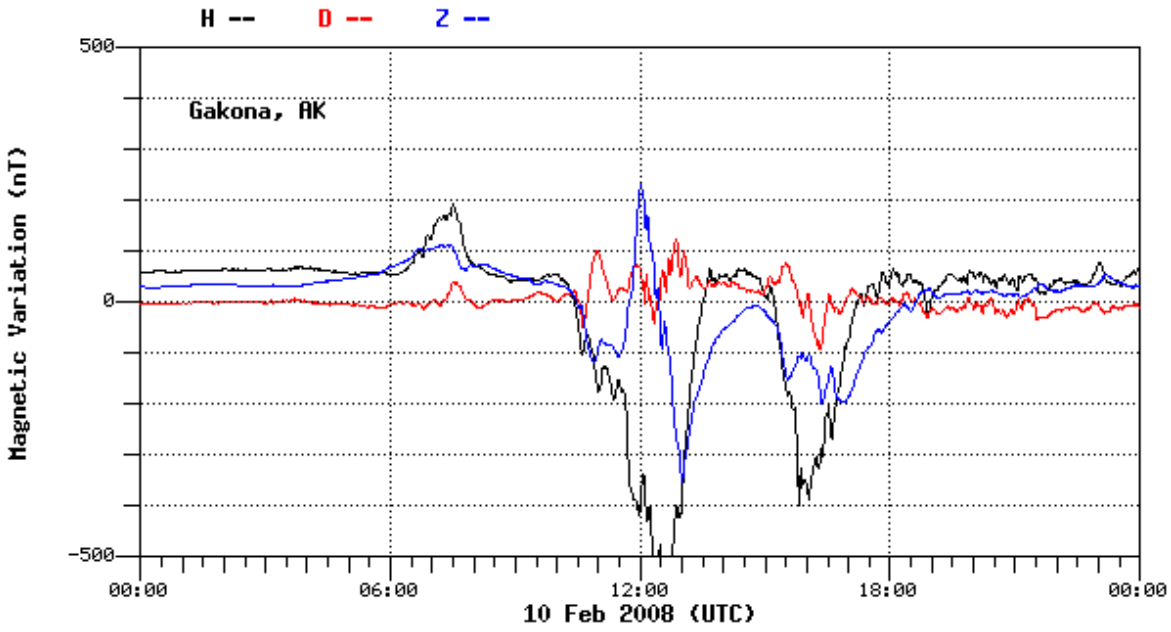

Figure 8. Gakona magnetometer data.

2.3. Tomographic Image Uncertainty Specification

2.3.1. Background

In Section 2.2. of SR1 for this contract, we described our approach to determining the uncertainty in density and f_oF2 derived from the tomographic inversion process. That approach

began with the theoretical specification of uncertainty provided by the framework we have used for the inversion process at the core of the tomographic system, and expanded on that by comparison with a few observations of f_oF2 made concurrent with our tomography images from the Digisonde located at Gakona. During the second part of the contract, we expanded this to include an assessment of the uncertainty in the vertical TEC derived from our tomographic images, and ran a more detailed comparison with a much larger set of Digisonde soundings.

2.3.2. Assessment of Uncertainty in Vertical TEC

A different approach was used in assessing the uncertainty in vertical TEC derived from the ITS images. In previous status reports, we described how observations of f_oF2 from the Gakona Digisonde were used to assess the accuracy of the theoretical estimates of the uncertainty in the images, and we discovered that the theoretical estimates were both too low and did not account for an offset in the uncertainty that reflects the tendency of the analysis to provide estimates of f_oF2 that are systematically low. There are no corresponding independent observations of TEC available for a similar comparison. Two potential sources were (1) TEC calculated from Digisonde measurements of the F2 peak, and (2) TEC from the Gakona GPS receiver system. Both were rejected due to uncertainties in both quantities that were at least on order of, if not larger than, the expected uncertainty in the ITS-derived TEC. The Digisonde-derived TEC was based on an estimate of the topside content (between h_mF2 and the nominal satellite altitude of 1,000 km), thus potentially over- or under-estimating the TEC in ways that are difficult to quantify. The GPS observations, on the other hand, include content from 1,000-km altitude out to the GPS satellites at (nominally) 20,000-km altitude. While the TEC in this height range is small, it can be on the order of 2-5 TEC units (10^{16} el/m^2). Additionally, there is inherent uncertainty in the TEC measurements due to differential group delay in the satellite and receiver which, while it is calibrated using the SCORE process, has uncertainties on the order of a few TEC units and, at the high latitudes sampled from Gakona, can be larger.

Rather than deal with these additional uncertainties, it was decided to use simulated ionospheric images as a basis for this study. These images were generated using the simple three Chapman layer profile model known as RBTEC which was developed in the mid-1970s by personnel at the Air Force Global Weather Central (*Damon and Hartranft*, 1970; *Flattery and Ramsay*, 1975). Three different types of images were generated: a smooth ionosphere with either no latitude gradients or with a constant south-to-north gradient in f_oF2; and two modifications of these smooth cases with a Gaussian-shaped enhancement in f_oF2 located within the image range: one with the enhancement situated near Gakona and the other with the enhancement situated near the northern end of the chain. Figure 9 shows an example of one of these "blob" images. TEC was calculated for the six stations in the HAARP chain by integrating through these images to pre-calculated satellite positions, and relative TEC was produced by subtracting off the TEC value of the first point in the simulated pass. These relative TEC records were processed using the standard ITS processing with each of the three EOF sets (day, dusk, and night) currently used in generating images at HAARP. Figure 10 shows the resulting ITS reconstruction of the image shown in Figure 9 using the "Day" EOF set. (Note that the barely discernable uncertainty bars on this plot were generated from the unmodified ITS variance estimates. As will be shown below, these underestimate the true expected uncertainty.)

These three image types were all controlled by setting four parameters: the latitude gradient, the f_oF2 value at the southernmost end of the image, h_mF2 for the entire image (h_mF2 was not varied in latitude), and a factor that controlled the topside scale height [this is an additional multiplicative factor added to the topside section of the RBTEC model described on page 341 of *Flattery and Ramsay* (1975)]. Table 1 summarizes the parameter settings used in generating the 576 images generated for this study. Since each of these images were processed using each of the three EOF sets, the study is based on a total of 1,728 analyses and over 300,000 individual estimates of f_oF2 and TEC. A database was built from these analyses which included, for each profile in each image, the f_oF2, h_mF2, and TEC from both the original and reconstructed images, as well as the estimates of the lower and upper bounds of both f_oF2 and TEC as derived from the ITS-calculated variance (denoted in this report by – and + superscripts and referred to as uncertainty estimates).

Table 1. Values of parameters used in generating the simulation image set. The Gradient parameter is the percent change in f_oF2 across the image from the initial value shown to the value in the final (northernmost) profile. The topside scale factor is applied to factors calculated by the RBTEC model.

Parameter	Values
Gradient:	None , 10% , 25% , 50%
Initial f_oF2:	2.5 , 4.5 , 6.5 , 9.5 MHz
h_mF2:	225 , 275 , 325 , 375 km
Topside scale factor:	1.0 , 1.3 , 1.6

The two plots in Figure 11 summarize the initial findings from this analysis. These are histograms of the percent difference between the f_oF2 and TEC calculated from the original images and those calculated from the ITS reconstructions. These histograms include the results from all 1,728 analyses. The solid curves are the calculated histograms, the dotted curves are normal distributions fit (in a least-squares sense) to the histograms, and the vertical long-dash lines indicate the averages of the difference between the original-image values and the X^- and X^+ values (where X is f_oF2 or TEC). These provide estimates of the expected average square-root of variance based on the ITS calculation of the variance for the image. The horizontal long-dash line indicates the "*1/e*" point in the histograms, which provides a location on each histogram that should correspond to the square-root of variance (assuming that the histogram is well represented by a normal distribution). If this horizontal line crosses the histograms at the same locations as the vertical horizontal lines, this would indicate that the observed variance (for these 300,000+ cases) was well represented by the modeled variance. As can be clearly seen in Figure 11, this is not the case. Not only is the variance too low, but it does not capture the offsets from zero clearly seen in both histograms. This is consistent with what was discovered in comparing with the Gakona Digisonde observations.

During the early stages of this analysis, the ITS processor was run using the modified variance calculation based on the Gakona f_oF2 analysis reported earlier. We encountered difficulties, however, in obtaining consistent results with the uncertainties in f_oF2 and N_mF2 because the modifications to the variance used in generating the uncertainty estimates were made partially in terms of plasma density and partially in terms of plasma frequency. For the purpose

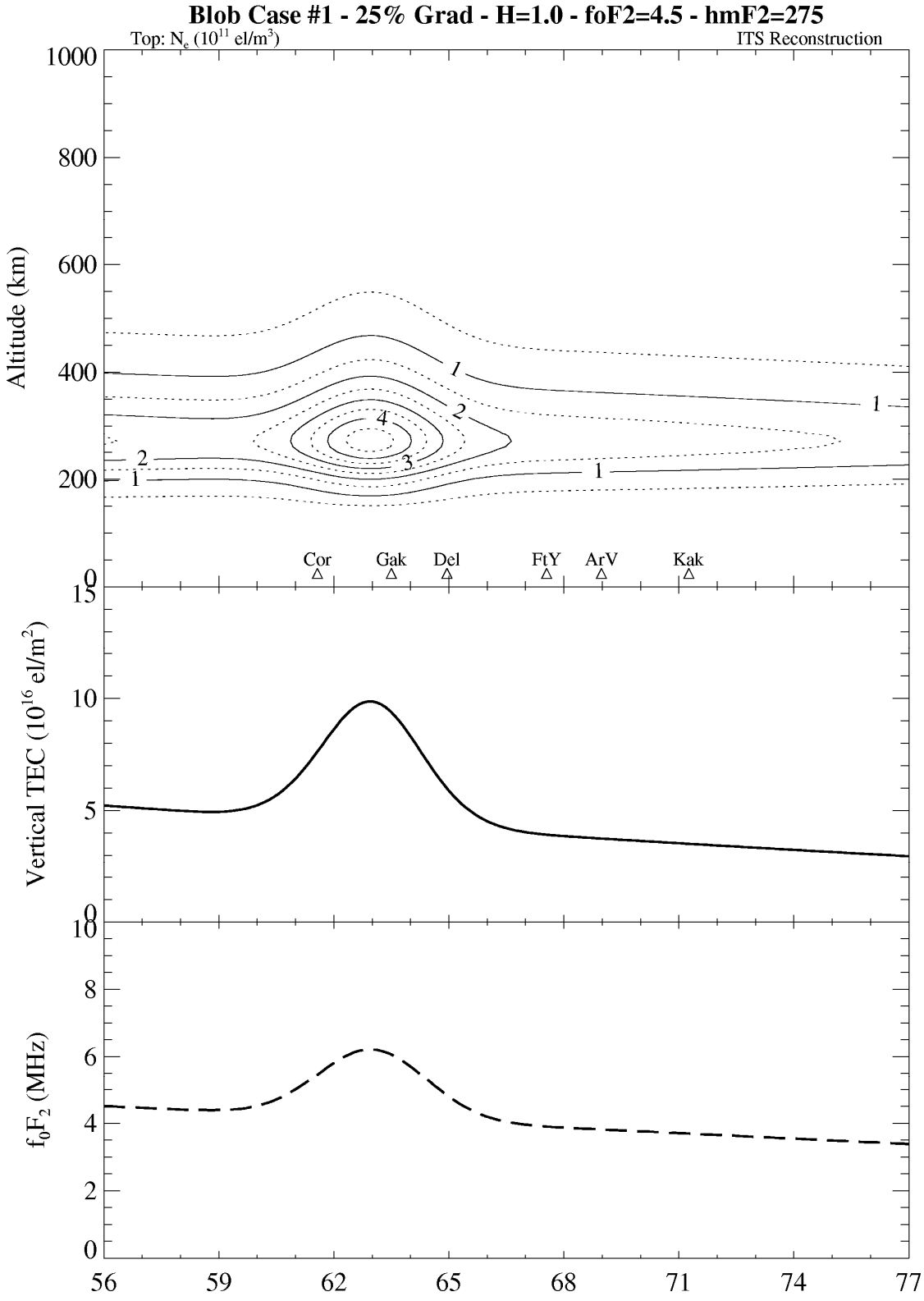

Figure 9. One of the simulation electron density images generated for the uncertainty study. The upper panel shows a contour plot of the electron density, the middle panel is the vertical TEC generated by integrating through the image in the upper panel, and the lower panel is f_0F2 derived from the profiles in the image.

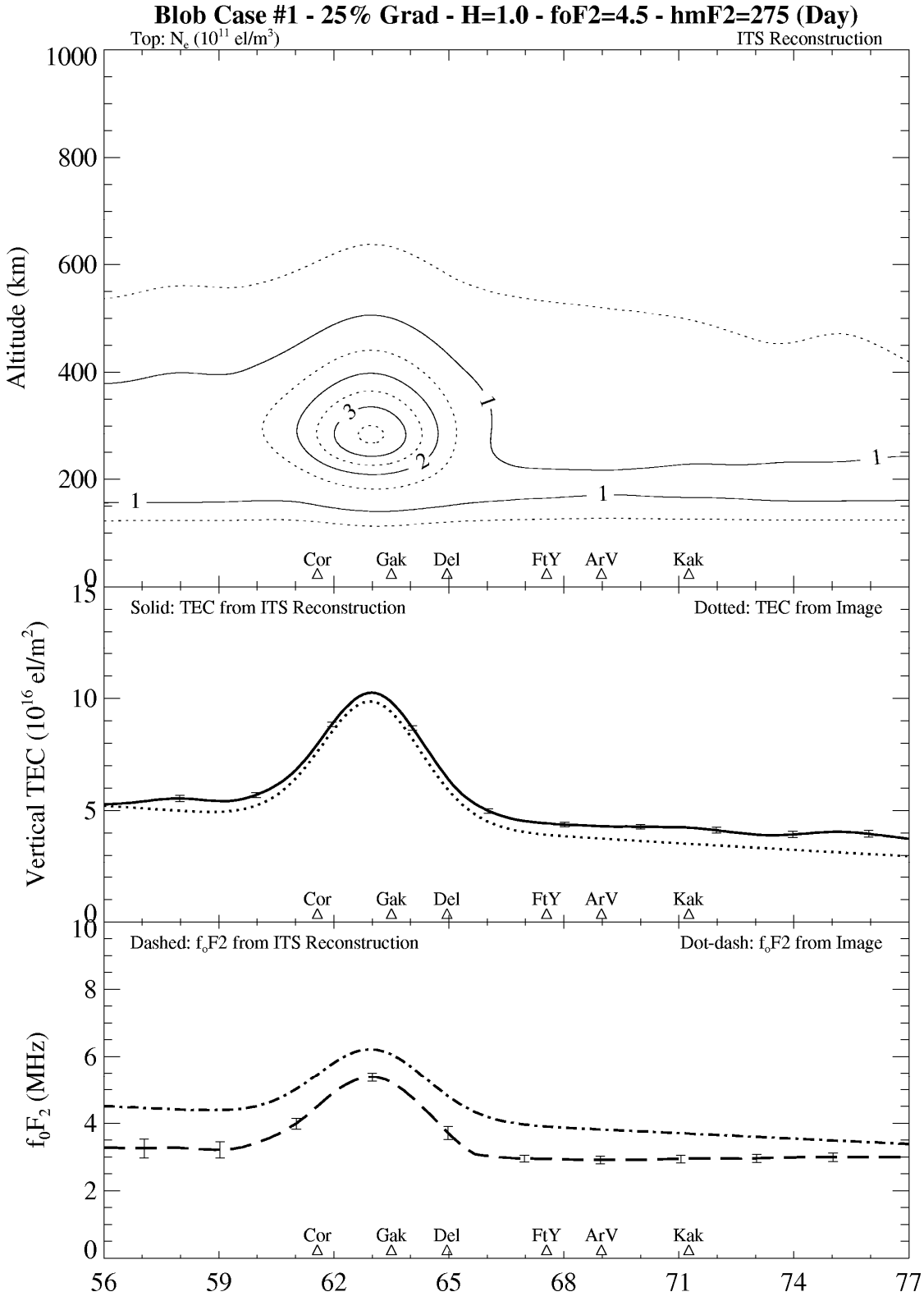

Figure 10. Results from the ITS reconstruction of the image shown in Figure 9. In the middle and lower panels, the TEC or f_oF2 from the original image is shown as a dotted curve and that calculated from the ITS reconstruction is shown as a solid curve. The error bars are uncertainties in TEC and f_oF2 calculated from the theoretical variances.

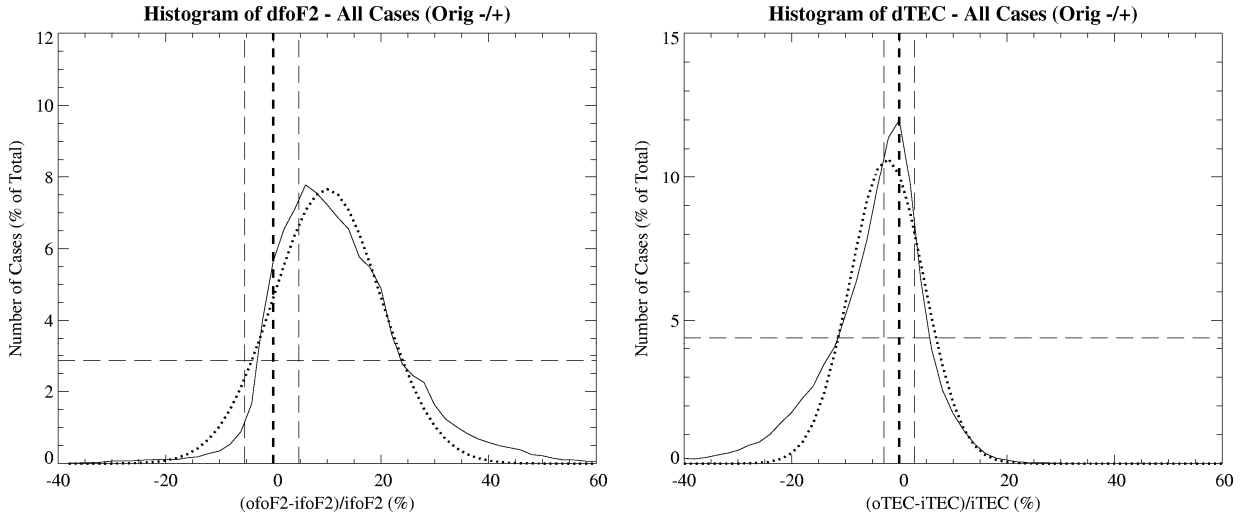

Figure 11. Histograms of the difference between the original and ITS reconstruction foF2 (left panel) and TEC (right panel). See text for description of the long-dash lines.

of this study, we disabled the adjustments we had implemented as a result of our comparison with the Gakona f_oF2 observations, which is why the uncertainty estimates reflected in the location of the vertical long-dash lines in Figure 11 for f_oF2 are smaller than will account for the variance shown in the histograms, and are symmetric about zero.

The adjustments made to the ITS-calculated variances in order to bring them more in line with the variances consistent with the histograms shown in Figure 11 were made following the same general algorithmic approach as that used in adjusting the variances in the Gakona f_oF2 study, with some small differences. As in the Gakona study, the variance calculated from the ITS theory (in program *stat_comp*) is multiplied by a factor of the form

$$M = (1 + a\overline{N_m F2}) \qquad [1]$$

where $\overline{N_m F2}$ is the image-averaged value of the density at the F2 peak and *a* is a free model parameter. This factor is applied to all variances in the variance image generated by the analysis. The offsets in the uncertainty values (obviously required, as can be seen in the offset and asymmetric histograms in Figure 11) are then applied when the estimates of profile parameters are generated (program *stat2image*). The offset calculation is implemented as a second free parameter, *b*, that is multiplied times either N_mF2 (for the f_oF2 uncertainties) or TEC to provide the necessary offset in the negative and positive uncertainty values. The desire is to find a value for the *a* parameter in this equation which provides good estimates of the uncertainty of all parameters shown in Figure 11. It is likely that the offset parameter, *b*, will be different for the peak and TEC parameters as evidenced by the fact that while the peak parameters show that the ITS analysis typically underestimates the values of the peak parameters, it typically overestimates TEC. We'll identify the offsets as b_P and b_I for the peak and TEC calculations, respectively.

It was discovered that while we were able to match the uncertainties as embodied in the histograms shown in Figure 11 for f_oF2 and N_mF2 using the same values for *a* and b_P, this still left the uncertainty calculated for TEC too low. To account for this, we introduced another

parameter, a_I, which is a simple multiplicative factor applied to the uncertainty calculated from the ITS variance image after it has been modified using the *M* factor described above. After a second iterative process, we found that the TEC uncertainty calculated from the variance image generated using the *M* factor needed to be increased by roughly 80% to achieve the variance shown in the histogram. The initial values derived for the four free parameters were:

$$a = 0.8 \quad , \quad a_I = 1.8 \quad , \quad b_P = -0.33 \quad , \quad b_I = +0.03$$

The results of these modifications on the uncertainties calculated are shown in Figure 12, which is a repeat of the histograms from Figure 11 with the new average uncertainties (the vertical long-dash lines) shown. Note that these now intersect the histograms at the *1/e* points as desired.

When these parameters were used to generate new error bars, we discovered that the calculated error bars did not appear to be representative of some of the simulated-image results. In particular, there appeared to be problems with some of the reconstructions made using the Day EOF set. The histograms shown in Figures 11 and 12 were regenerated independently for the reconstructions from each of the three EOF sets, with the results shown in Figure 13. We decided that rather than fitting to the aggregate histograms, we would set the lower and upper ranges of the uncertainty to fit the lowest and highest *1/e* points of the three histograms. This altered the values of the four parameters to the following:

$$a = 1.3 \quad , \quad a_I = 1.5 \quad , \quad b_P = -0.40 \quad , \quad b_I = +0.03$$

This set provided better overall representation of the uncertainty, and the value for *a* is now very close to that determined in the analysis of the Gakona f_oF2 Digisonde data (1.2). This also reduced the amount by which the TEC uncertainty is increased over the increase needed to fit f_oF2 from 80% to 50%.

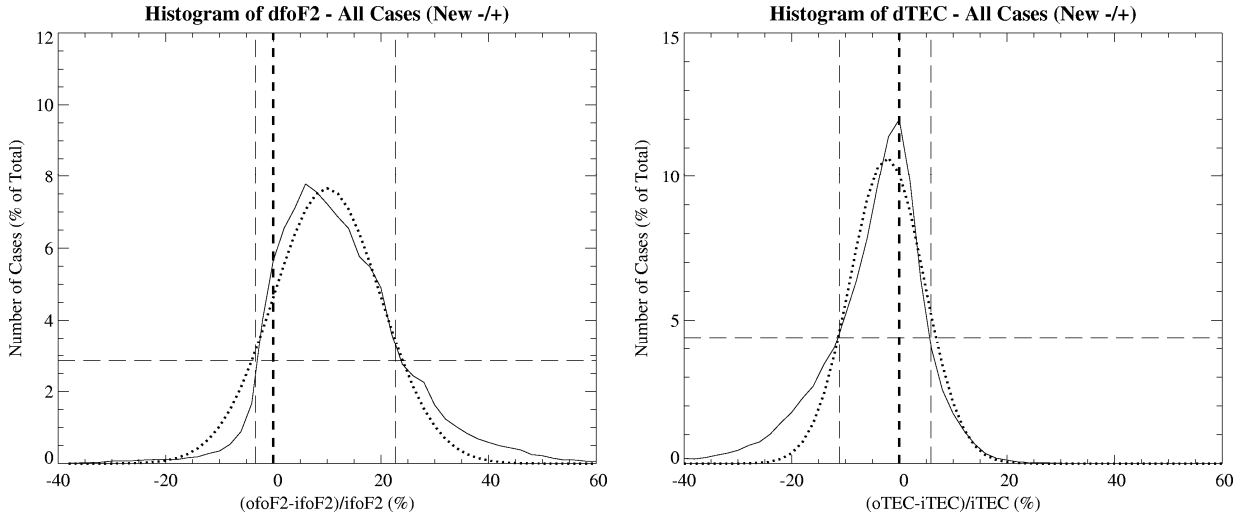

Figure 12. Histograms as shown in Figure 11 with uncertainty locations from the analysis of the aggregate histograms.

The need to increase the variance by a factor of 50% for the TEC uncertainties to match the histograms generated from the simulation studies arises from at least two sources: (1) a breakdown in an underlying assumption made in calculating the TEC variance from the density

variance map, and (2) a breakdown in the implicit assumption that the multiplicative factor which correctly adjusts the variance at the F2 peak (the *M* factor) is valid for all heights in the profile. We'll address these separately.

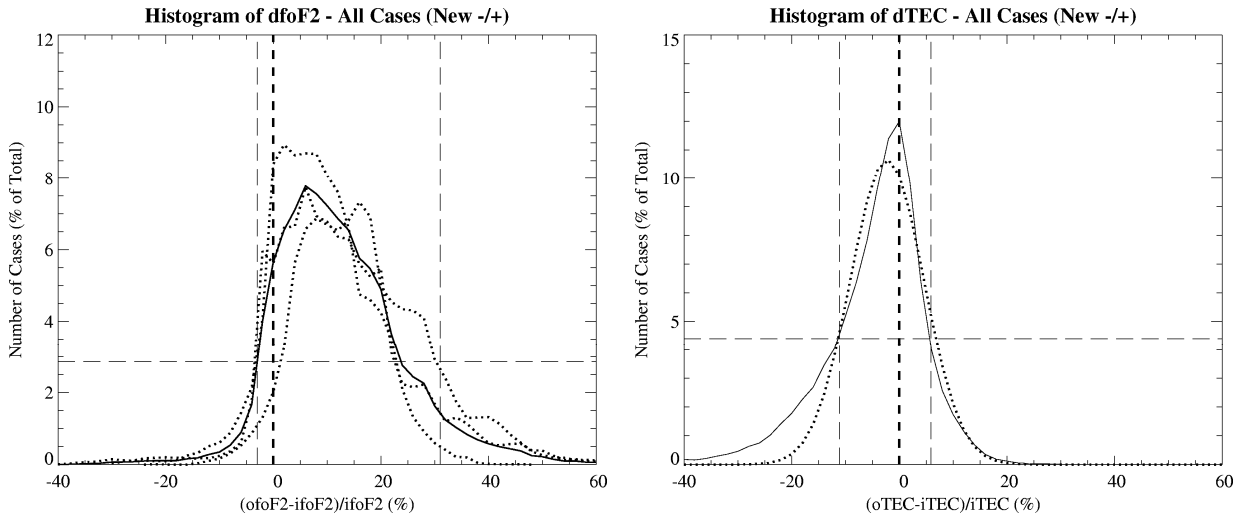

Figure 13. Histograms as shown in Figures 11 and 12 with uncertainty locations from the analysis of the Day, Night, and Dusk EOF set histograms. The aggregate histogram is the solid curve, and the individual EOF sets are dotted curves.

The expected uncertainty in vertical TEC derived from the ITS images is calculated from the density variance images produced by the ITS software by summing up the product of the size of the vertical bins squared times the variance in each bin of the vertical profile. This provides an estimate of the total variance to be expected in the TEC based on the density variances in each profile bin, assuming that there is no correlation between the variations of N_e in each bin. The square root of this variance is then used to provide for error bars, or an uncertainty range, around the TEC calculated from the ITS N_e image. An underlying assumption used in deriving this calculation is that there is no correlation in the density variations in the various bins. If there is correlation, extra terms show up in the equation used to calculate the expected TEC variance from the density variances. Assessing the magnitude of this source, in terms of additional TEC variance, is difficult using the simulation set we have employed. However, it is to be expected that there is some correlation between the density variations in adjacent bins, and that this is, at least qualitatively, a clear potential source for "extra" variance, beyond what has been calculated.

The validity of the assumption that the *M* factor derived at the F2 peak can be applied at all altitudes throughout the profile is clearly called into question by the results shown in Figure 14. This figure shows the height variation of the average square root of variance (a good estimate of the uncertainty) for a randomly selected simulation image. The heavy solid curve is that calculated directly from the initial and reconstructed images, the light solid curve is calculated from the ITS-generated variance image, and the dotted curve is the ITS-generated variance scaled to match the variance calculated from the reconstructed image at the F2 peak. The two horizontal lines indicate the range of h_mF2 in the reconstructed image. Two things are clear from this plot: (1) the height variation of variance as generated from the ITS processor is not adequately modeling what is observed, and (2) a scaling factor that brings these two curves into

agreement at the F2 peak is not valid for the entire profile, particularly just below the F2 peak and in the topside of the profile, and is likely to lead to an underestimated TEC variance.

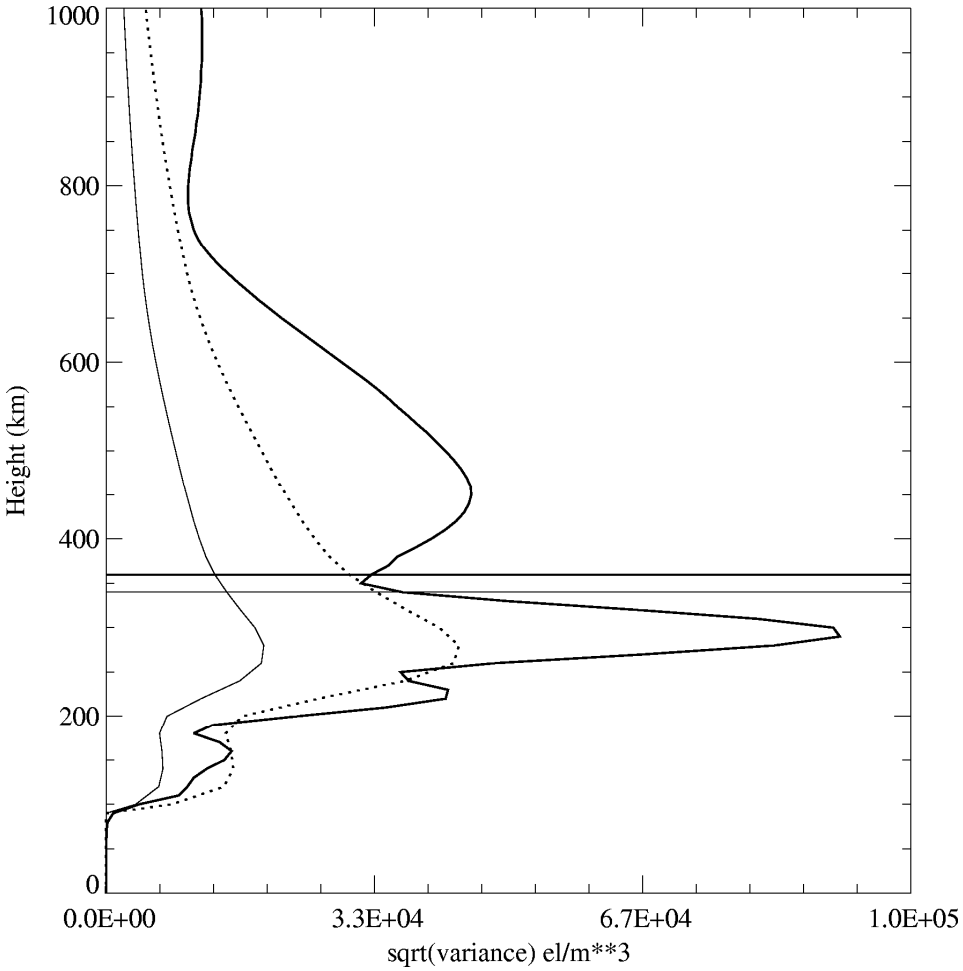

Figure 14. Comparison of the uncertainty calculated for a single simulation image by (1) direct comparison with the original image (heavy solid line) and (2) calculated from the ITS theory (thin solid curve). The dotted curve is the theoretical curve scaled to match the direct-comparison curve at the F2 peak. The horizontal lines indicate the range of the height of the F2 layer in the image.

Given limitations in resources available to continue pursuing this aspect of the ITS processor, we have chosen to not attempt to identify which of these two sources provides how much of the observed underestimate in TEC variance, nor to search for other potential sources. We will implement the scheme outlined here in the ITS processor and use it to calculate estimates of the uncertainty in the f_oF2 and TEC values which are posted on the HAARP web site. Figure 15 shows the final comparison of the simulated and tomography f_oF2 and TEC using the final algorithm for the uncertainty bars. Note that the simulation image used in this report to illustrate the uncertainty calculation is, despite being selected at random, very nearly a worst-case example. This is reflected in the fact that the differences shown in Figure 15 between the f_oF2 and TEC reconstruction and the "true" values from the simulated image are at, and in some cases beyond, the uncertainty bars.

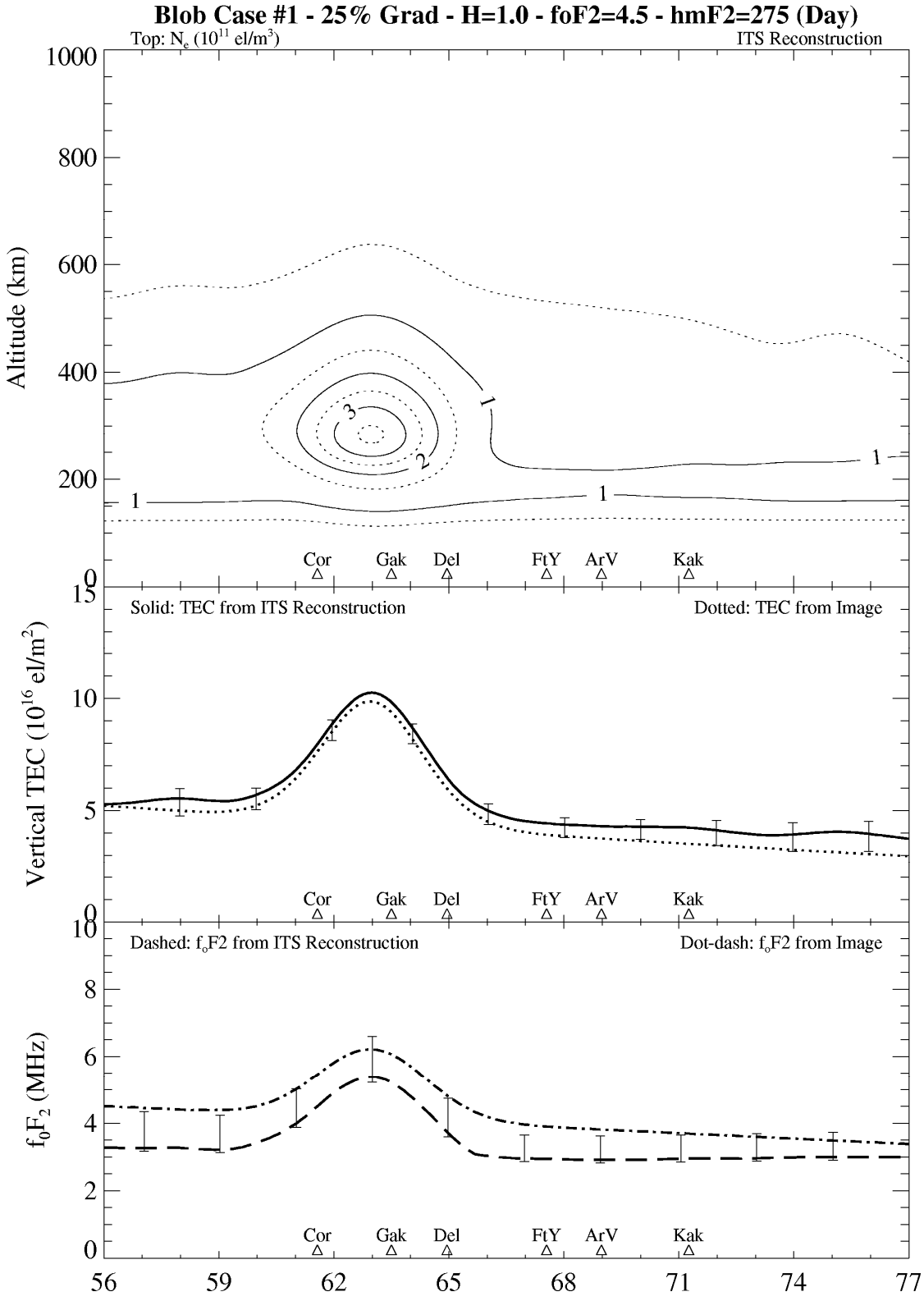

Figure 15. Sample reconstruction showing uncertainty estimates (error bars) calculated using the new algorithm.

2.3.3. Comparisons with Digisonde Observations

In the original investigation of uncertainty in our estimates of f_oF2, a small sample of hand-analyzed Digisonde observations of f_oF2 was used to estimate the true uncertainty in our images. Subsequent to the word described in the preceding section, we were able to obtain a much larger set of post-processed Digisonde f_oF2 and h_mF2 observations from both the Gakona Digisonde and a second Digisonde located at College, Alaska. These data were provided by Dr. Ivan Galkin of the Center for Atmospheric Research at the University of Massachusetts Lowell campus. Table 2 shows months for which data were provided by Dr. Galkin for the years 2001 through 2006. This provided over 13,000 observations of f_oF2 over this six-year period.

Table 2. Months for which UML-supplied Digisonde data are available.

	January	February	March	April	May	June	July	August	September	October	November	December
2001	X	X	X	X	X	X	X	X	X	X	X	X
2002	X	X	X	X	X	X	X	X	X	X	X	
2003	X	X	X	X	X	X	X	X	X			
2004	X	X	X	X	X	X	X		X			
2005	X	X	X	X	X				X			
2006	X	X	X	X	X							

The original plan for these data was to revisit the algorithms described in the previous section that provide estimates of uncertainty in f_oF2 and TEC derived from our tomography images and then adjust these algorithms as indicated by the analysis results. We were only able to begin this process, as with the completion of the HAARP facility, the focus of our efforts shifted to support for campaign operations at the site and analysis of data collected during those campaigns. We will report on progress made to date on this effort. It will serve as the starting point for future work to improve our estimation of uncertainty in products derived from the tomography images.

Figures 16 through 21 summarize the results of the comparison as conducted to date. Each of these figures consists of five plots showing the variation of the difference between the tomography-derived and Digisonde-derived f_oF2 and h_mF2 as a function of day-of-year (DOY) (Figures 16 and 17), local-solar time (SLT) at the tomography array center longitude (Figures 18 and 19), and sunspot number (SSN) (Figures 20 and 21). Note that we used a sunspot number derived from the observed 10.7-cm solar radio flux, which is a better surrogate for the effect of solar EUV radiation on the ionosphere than is the observed sunspot number. For each of these six figures, the results have been divided into five cases: all observations (center plot), cases where the Day EOF sets were used in the tomographic analysis (upper-left), the Night EOF set (upper-right), dawn hours (local midnight to noon) using the Dawndusk EOF set (lower-left), and dusk hours (noon to midnight) using the Dawndusk EOF set (lower-right). The tomography system automatically determines which EOF set to use for a particular satellite pass based on the solar zenith angle at the center of the tomography array at the center of the pass time. Note that the gap in data points evident in the SLT plots is an artifact caused by how times are assigned to

the tomography results and are not due to a gap in observations. A similar thinning-out of data towards the latter part of the year (as seen in the DOY plots) is due to the uneven sampling provided by the UML Digisonde data set, which has less data provided from the months at the end of the years covered.

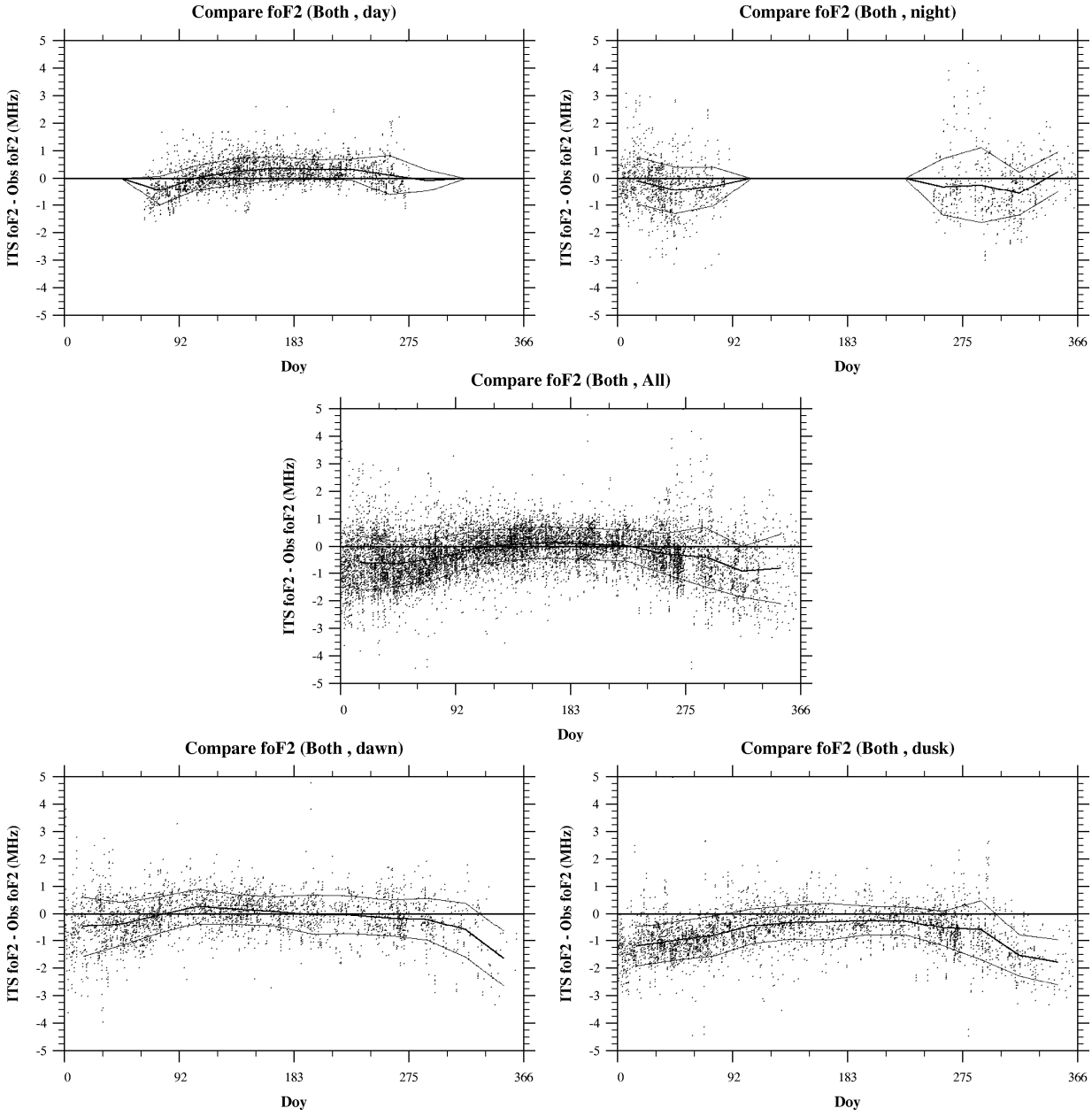

Figure 16. Variation of the difference between tomography-derived and Digisonde-derived f_oF2 as a function of day of the year (DOY). The upper two plots are for tomography cases in which the Day and Night EOF sets were used, the lower two plots are dawn (lower-left) and dusk (lower-right) cases using the Dawndusk EOF set, and the center plot is all cases. The heavy line is an average calculated in 15-day wide bins, and the two light lines are ±1 sigma from the mean. This analysis includes data from both Gakona and College Digisonde.

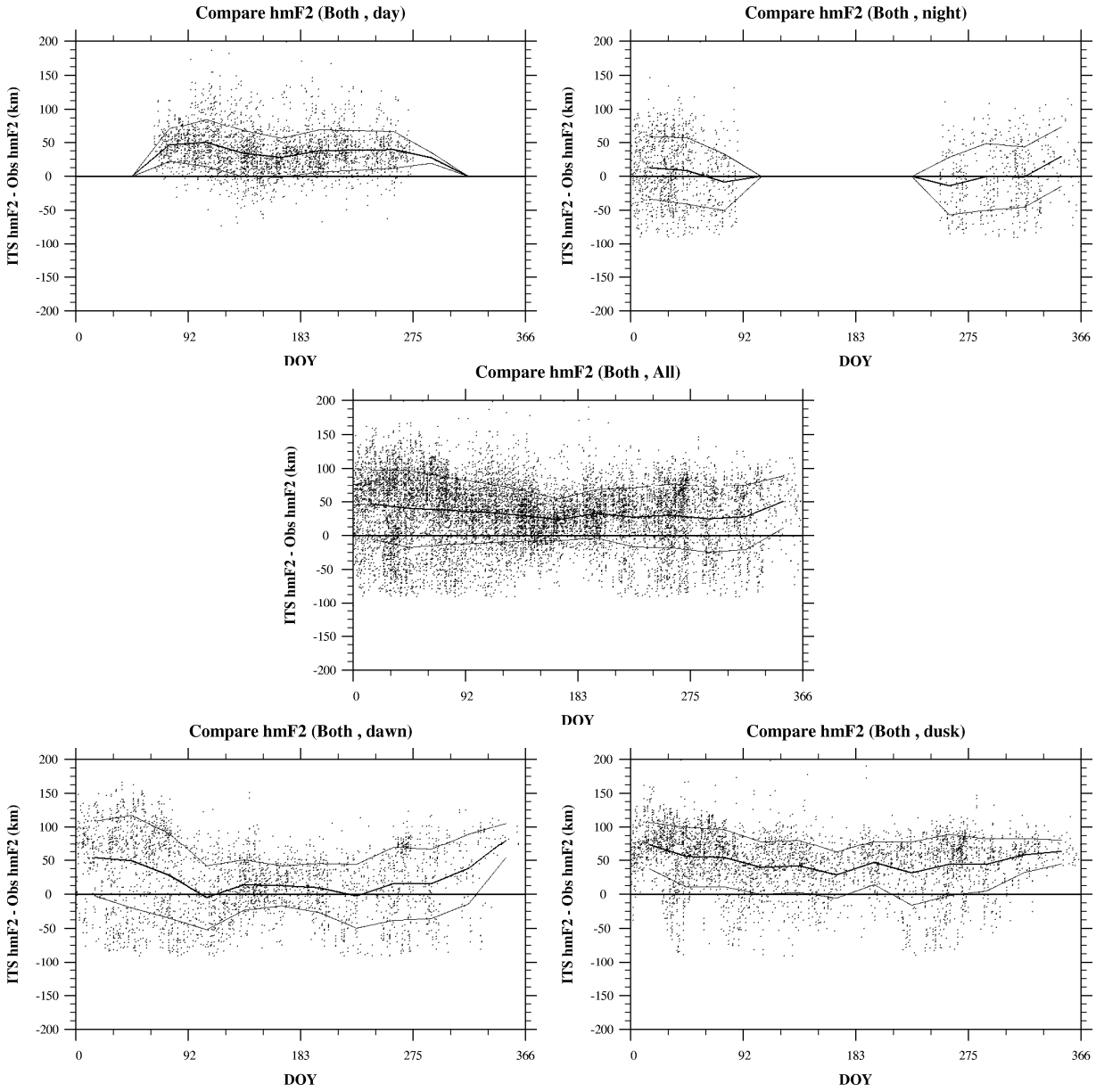

Figure 17. Variation of the difference between tomography-derived and Digisonde-derived h_mF2 as a function of day of the year (DOY). The figure layout and plot details are as in Figure 16.

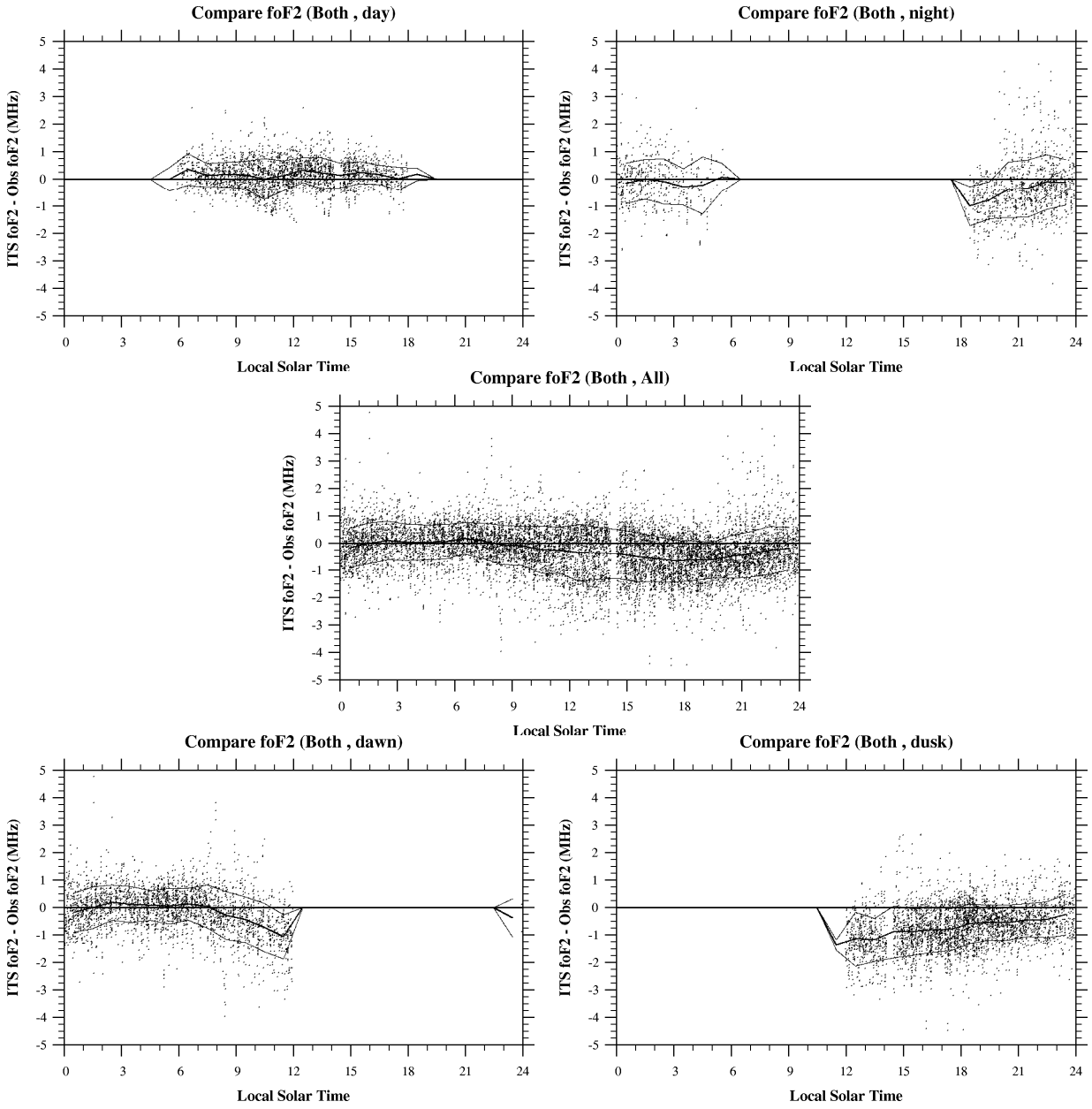

Figure 18. Variation of the difference between tomography-derived and Digisonde-derived f_oF2 as a function of local-solar time at the center of the tomography array (SLT). The figure layout and plot details are as in Figure 16.

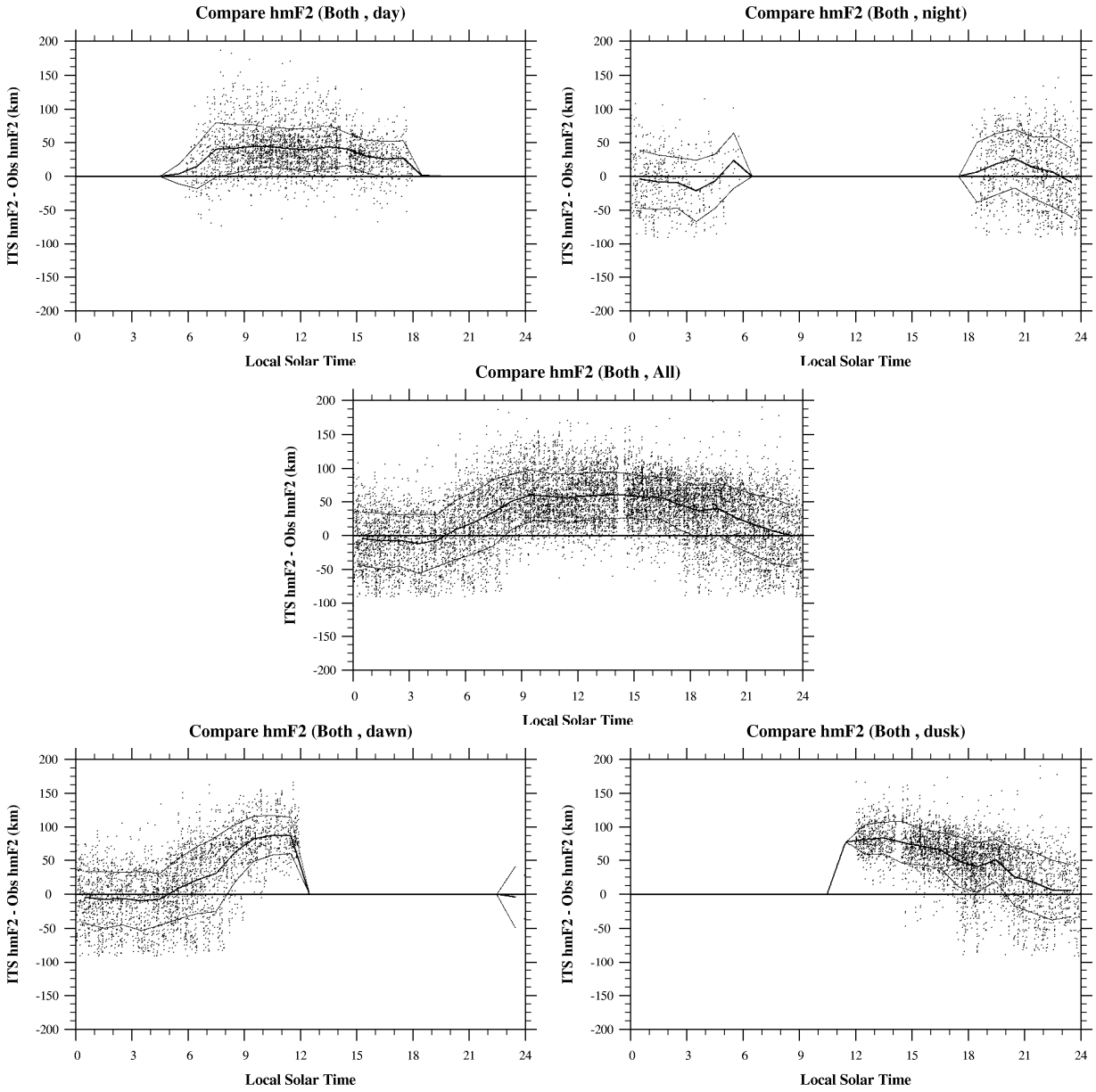

Figure 19. Variation of the difference between tomography-derived and Digisonde-derived h_mF2 as a function of local-solar time at the center of the tomography array (SLT). The figure layout and plot details are as in Figure 16.

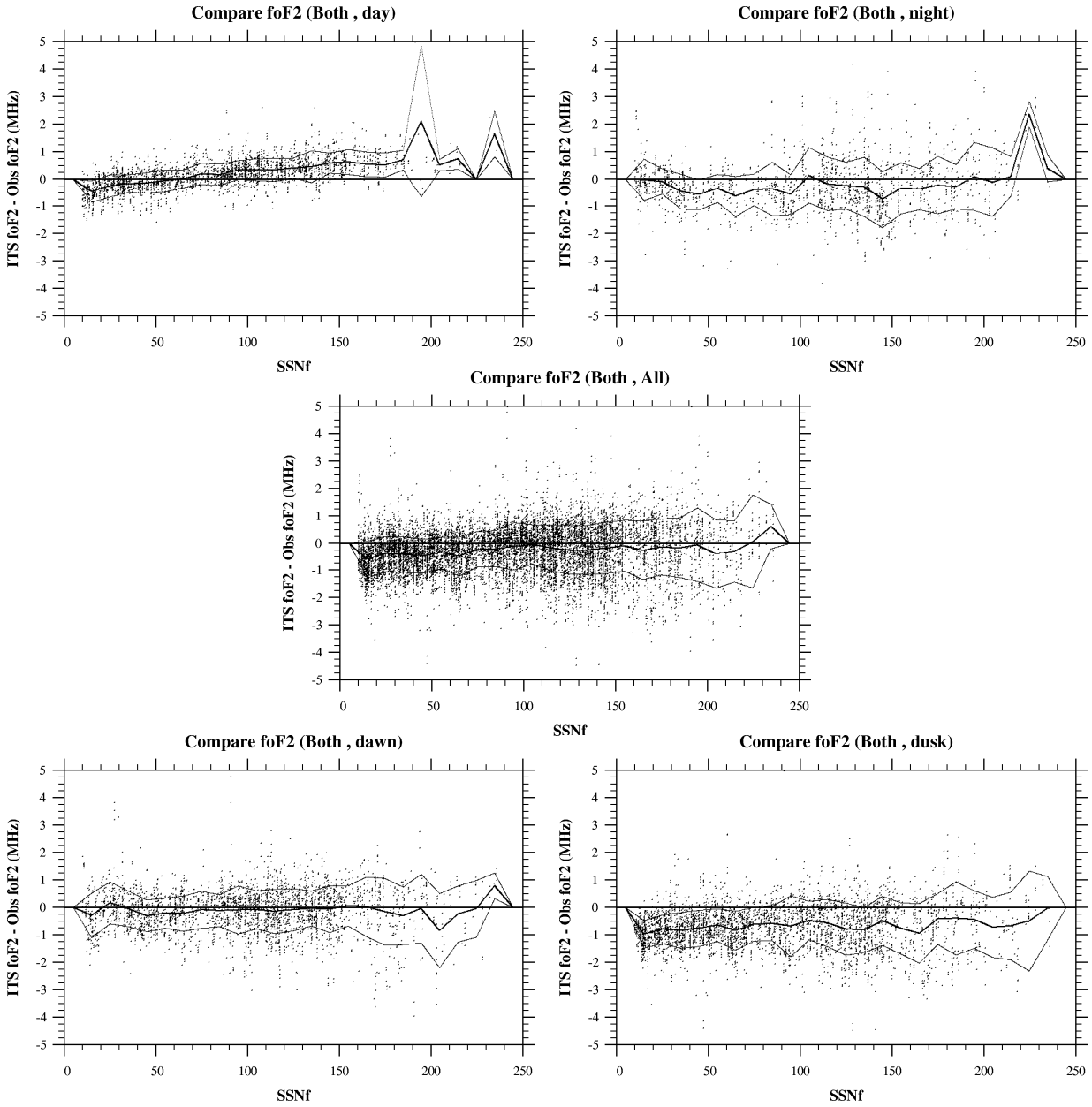

Figure 20. Variation of the difference between tomography-derived and Digisonde-derived f_oF2 as a function of sunspot number (SSN). The figure layout and plot details are as in Figure 16.

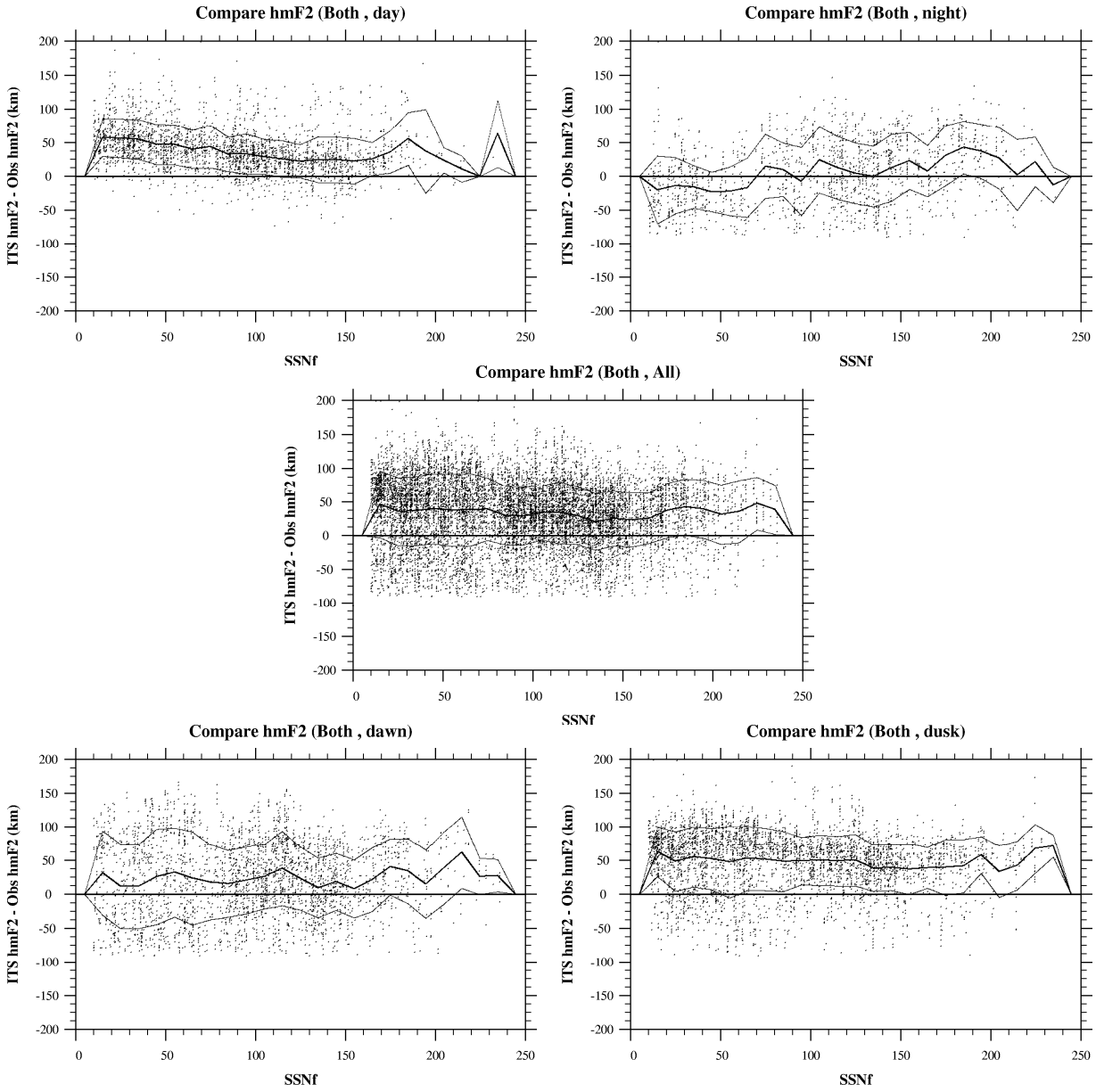

Figure 21. Variation of the difference between tomography-derived and Digisonde-derived h_mF2 as a function of sunspot number (SSN). The figure layout and plot details are as in Figure 16.

Two things are evident from even a cursory look at these results. First, we should adjust our uncertainty scheme to vary with the EOF set employed in generating the tomography image and, perhaps, add in variations with time, season, and SSN. Second, we should revisit our algorithm for determining when we should use a particular EOF set, either selected from the three we have been using or from a different set tailored in a different fashion. Neither of these activities were possible within the remaining scope of this contract, but we will lay out a skeleton plan in this report for addressing these in the future.

The results shown in these figures can, however, provide us with guidance for assessing uncertainty in F2-region parameters derived from the tomography images using the present set of EOFs. The salient points to note are as follows:

f_oF2:

1. As was seen in the analysis of the simulation data set, the tomography-derived values for f_oF2 tend to be systematically lower than the observed values, in this case observed by a Digisonde. However, there are clearly diurnal and seasonal variations in this offset, which may be coupled, and also the behavior is different for the different EOF sets.

2. The performance of the Dawndusk EOF set is clearly much better on the "dawn" side than on the "dusk" side; performance which begins to worsen as daytime conditions are encountered at sunrise. This might indicate that we should transition sooner to the Day EOF set on the dawn side and later from Day to Dawndusk on the dusk side. Also, we should look at using a different EOF set for evening twilight (dusk) than for morning twilight (dawn).

3. The night case shows the most scatter, which is not surprising given the challenge of both imaging the night auroral ionosphere and of measuring the F2 region using an ionosonde.

4. There is a clear trend in the average curve for the variation with SSN for the Day EOF case. In early development of the tomography system, particularly in design and selection of the EOF sets to use, we speculated on the need to tailor the EOF sets used as a function of the point in the solar cycle. The results shown in Figure 20, as well as the corresponding result for h_mF2 shown in Figure 21, support this conjecture.

h_mF2:

1. There is clearly a diurnal variation in the performance of the tomography system's ability to accurately specify the height of the F2 layer. Both the Day and Dawndusk EOF sets show a tendency to overestimate h_mF2 during the day, with a transition to a nearly zero mean difference between the tomography and Digisonde values at night.

2. There is no clear seasonal variation, with a broader spread (in terms of RMS variation) in the difference than seen in the SLT plot.

3. While the scatter in the Night EOF results appears larger than for the other two EOF sets, this is not as large a difference as in the f_oF2 results.

4. Similar to the f_oF2 SSN variation, the Day EOF set results show a systematic trend that could be an indication that we should investigate different Day EOF sets as a function of solar cycle epoch.

Figure 22 shows histograms of the f_oF2 results; in this case, the percent difference calculated from $(f_oF2_{Digi} - f_oF2_{ITS})/f_oF2_{ITS}$. Note that this is the opposite sense of the data shown in the scatter plots, which show $(f_oF2_{ITS} - f_oF2_{Digi})$. This change is made to facilitate comparison with the simulation results discussed in the previous section. In particular, the upper-left plot in this figure (for all EOFs) should be compared to Figure 13 in that section. Two things are evident in the results shown in Figure 22. First, while the tomography f_oF2 values tend to underestimate the Digisonde observations, the offset is much less than that shown in Figure 13. Also, the distribution curve is a bit broader than that obtained from the simulation data, which should not be surprising given that the simulation result was obtained from a smooth, relatively well-behaved, model ionosphere. Assuming we continue to use a single algorithm for all EOF sets, these results indicate that the uncertainty bars for f_oF2 should be broader than are being produced by our current algorithm and the offset of the error bars from the tomography values should be less, perhaps much less, than at present. A quick rerun of the analysis that produced the values used in the uncertainty algorithm described in the previous section gave values of 3.4 for parameter a and –0.20 for parameter b_p, reflecting both the smaller offset (controlled by parameter b_p) and the broader distribution in the uncertainty (controlled mostly by parameter a).

An interim next step, based on retaining the current simple model for the uncertainty, is to use the information gleaned from this preliminary analysis to adjust the parameters of the present model. Since the model for uncertainty in the TEC derived from the tomography images is coupled to the model for f_oF2 uncertainty (through the adjustment of the variance output by the inverse processor), we cannot simply implement new parameters without reconciling the changes to the TEC uncertainty. Since we have no source of independent TEC, other than GPS TEC which provides TEC over a much larger height range, we will need to make this reconciliation based primarily on what was learned from the simulation analysis.

The steps to be taken to make use of the comparison of the tomography and Digisonde data sets to improve the tomography process and the specification of uncertainty in the resulting images are as follows:

1. Make a more careful analysis of the histograms shown in Figure 22 to derive new values for the f_oF2 uncertainty model and revisit the simulation results in light of this modification to the f_oF2 uncertainty to reset the TEC uncertainty model parameters.

2. Collect additional Digisonde observations, if possible, to better cover the last several months in each year listed in Table 2.

3. Expand the analysis described in this section to better separate local time and seasonal variations.

4. Review the use of EOF sets in the tomography analysis. This will include refining the algorithm used to determine which set to use (currently tied to the solar zenith angle) and looking at gains to be made by having EOF sets tailored by SSN.

5. If the EOF sets are changed, or their use is changed, reprocess all of the tomography data sets to generate new images.

6. Redo the comparison of the tomography-derived f_oF2 and h_mF2 with the Digisonde data and develop a new model for uncertainty based on this new analysis.

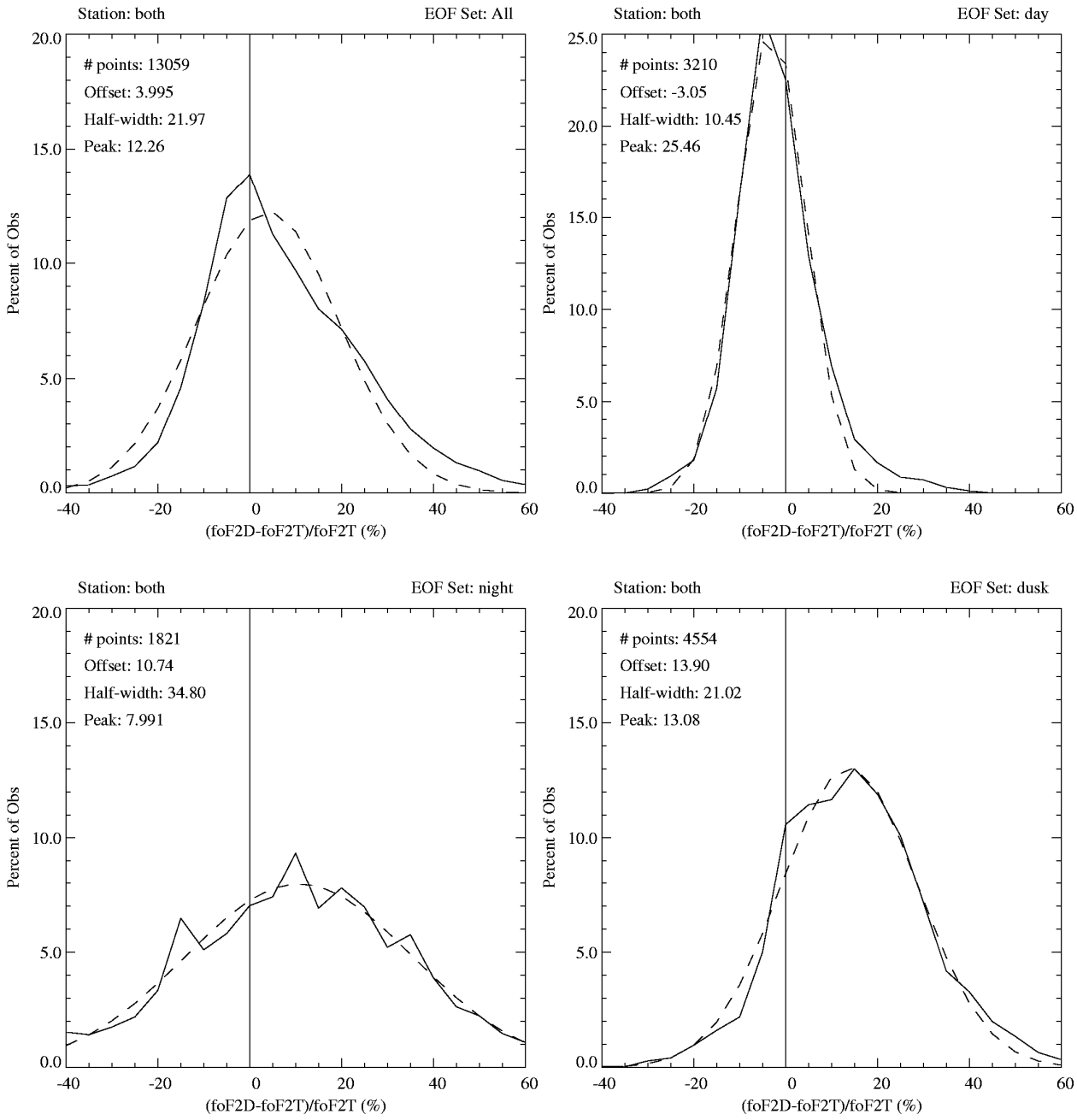

Figure 22. Histograms of the percent difference between Digisonde f_0F2 and tomography f_0F2 for all cases (upper left), Day EOF set (upper right), Night EOF set (lower left), and Duskdawn EOF set (lower right). Solid curves are the data, and the dashed curves are Gaussian curves fit to the data.

7. Either adjust the TEC uncertainty model to be consistent with both the new F2-region uncertainty model or revisit the TEC uncertainty through redoing the simulation analysis with the new EOF sets.

The goal of this process would be both an improved performance of the tomography processor and a better specification of the uncertainty in parameters of interest derived from the tomography images.

2.4. Digisonde Inclusion in Tomography

As we have previously demonstrated, the tomographic inversion processor we have developed is capable of using data from both Digisonde soundings and from *in-situ* density measurements from the DMSP SSIES instrument (see 4.1.2.3.2 in *Andreasen et al.,* 2004). While we have used this capability in post-analysis inversions, we have never implemented it for use in our near real-time inversions which are posted on the HAARP web site. The DMSP SSIES data are not available until well after-the-fact (we obtain these data from Dr. Fred Rich, AFRL/VSBXP), and while the Gakona Digisonde data are available in near real-time, the difficulty in automated analyses of high-latitude ionospheric soundings and lack of adequate quality-control information has relegated use of the data to post-analyses when a human can review the Digisonde analyses for accuracy. We have found that using either type of additional data as input can markedly improve the results through providing "tie-down" points in the vertical profile, not just in the vicinity of the observation, but across the entire image.

We have begun work on finding a way to be able to use at least some of the Digisonde analysis in our real-time images. As shown in Figure 23, there is gain to be had by including the Digisonde f_oF2 and h_mF2 estimates. The plots on the left side of Figure 23 show the tomography inversion results using only slant-range relative TEC from the tomography chain. Note the difference between the f_oF2 derived from the tomography inversion (lower panel on the left side) and the Gakona and College Digisondes as indicated by asterisk (*) symbols. This tendency of the tomography inversion process to underestimate f_oF2 (and overestimate h_mF2) during the daytime hours appears to be fairly systematic (a finding of our ongoing study of uncertainty in the tomographic inversion process). The plots on the right side of Figure 23 show the results when the f_oF2 and h_mF2 from a single Gakona Digisonde sounding are added to the TEC data. Note that the input of this single-point observation greatly improved the f_oF2 fit at the College Digisonde location, which was not input to the analysis.

Due to the improvement provided by using the Digisonde data, we began work to determine how we might be able to use at least some of the Digisonde observations in our real-time analyses. Due to limitations in resources, this never progressed beyond preliminary discussions with various experts in the field of quality control of Digisonde observations (Dr. Terry Bullett, Mr. Leo McNamara, Dr. A. Lee Snyder, Prof. Bodo Reinisch, and Dr. Ivan Galkin). This would be a fruitful area to investigate further.

2.5. Observations of the Artificially Perturbed Ionosphere

NWRA was involved in three campaigns at the HAARP facility near Gakona, AK, during the period covered by this report: the March 2006 HAARP Optics Campaign, the October 2008 HAARP Irregularities and Optics Campaign, and the February 2008 HAARP Irregularities and Optics Campaign. In addition to running experiments, NWRA was given the responsibility to coordinate and oversee the latter two of these campaigns. The October 2007 campaign was scheduled to run for 10 days but, due to difficulties at the site, this campaign was terminated after the first day. No results were obtained from that campaign, although we did discover an

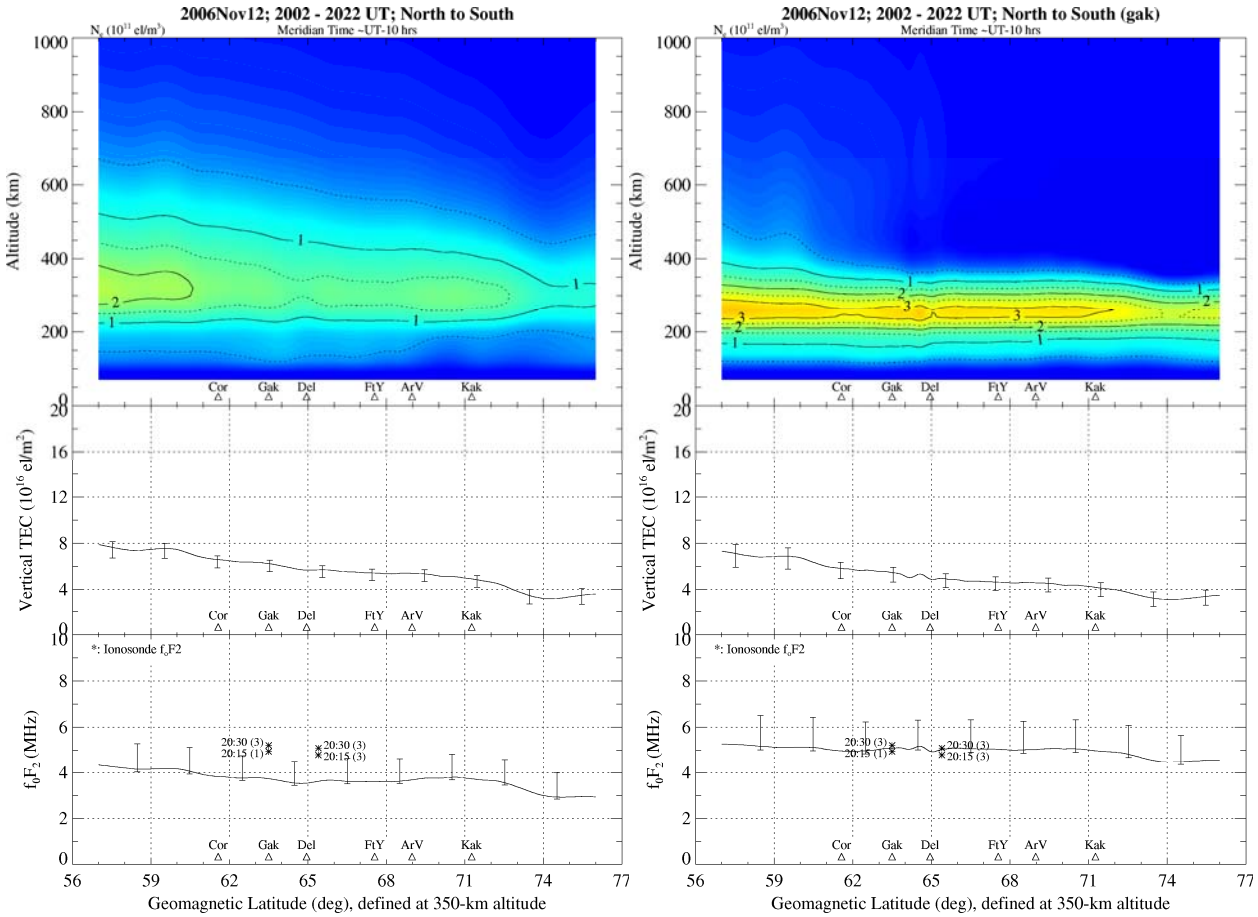

Figure 23. Tomography results for 12 November 2006. The results in the three panels on the left side were generated using only slant-range relative TEC, while the results shown on the right side were generated using both TEC and a single Gakona Digisonde observation.

inconsistency in how passes were identified for collection between the fixed and mobile receivers which saved us from losing passes in the February campaign. In this section, we will present results obtained during the March 2006 and February 2008 campaigns.

2.5.1. Results from March 2006 Campaign

We obtained IRI support for two short time periods during the March 2006 HAARP Optics Campaign in conjunction with two NIMS passes very near to the field-aligned location in the heater field-of-view. A major difference from similar experiments attempted during the 2003 optics campaign was that these passes occurred during morning daylight hours. The first pass was unsuccessful due to sudden onset of geophysical activity, generating irregularities from naturally occurring processes and producing high levels of absorption in the lower ionosphere, effectively shielding the F2 region from the heater effects.

We were more successful with the second pass on 27 March 2006, with the time of nearest approach to the field-aligned point at 00:33:51 UT. Geophysical conditions were very quiet, and we were able to observe irregularity-generated scintillation on the VHF and UHF signals from

the Oscar 25 satellite. Data from the SuperDARN radar located at Kodiak, AK, confirmed that there were no natural irregularities in the scale-sizes the radar is sensitive to both prior to, and after, the time period during which the heater was running. Figure 24 shows a section of the VHF and UHF detrended signal intensity and the detrended differential phase centered on the time during which the ray path passed through the heated region. While it is typical to see enhancements in scintillation levels when the raypath approaches the field-aligned point, this enhancement requires the presence of irregularities to operate. Data from this same pass at Delta Junction and at Cordova both showed no enhancement in scintillation levels at their respective field-aligned points, and similar passes with the same geometry and time-of-day taken at Gakona have also not shown enhancements of this level. We are fairly certain that the irregularities that caused the scintillation shown in Figure 24 were generated by the heater. Further details and analyses of this pass were presented in a poster at the 12th Annual Ionospheric Interactions Workshop in Santa Fe (*Secan and Fremouw,* 2006).

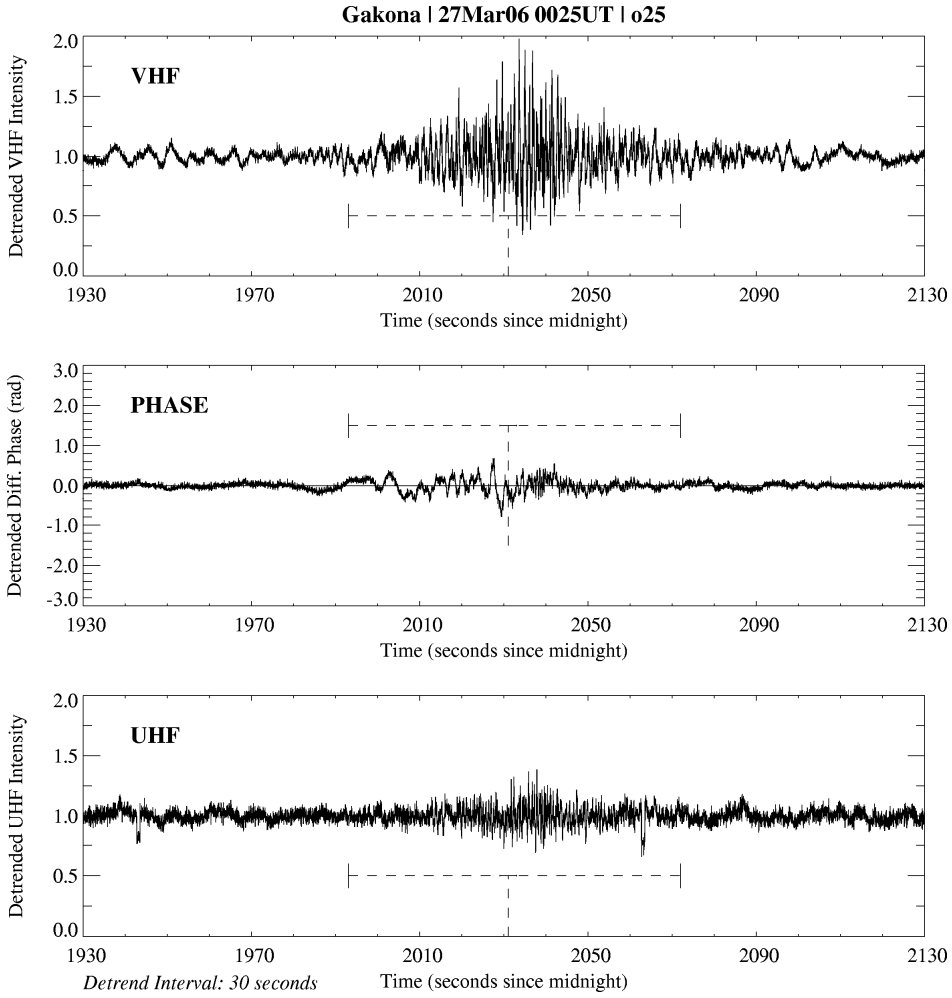

Figure 24. Detrended VHF (top panel), UHF (middle panel), and differential phase (lower panel) from a 200-second segment of data collected at Gakona, AK, from the Oscar 25 pass at 0033 UT on 27 March 2006. The vertical dashed line indicates the time of closest approach to the field-aligned point (as observed from Gakona), and the horizontal dashed lines indicate the time during which the ray path was within 8° of beam-center (the region within which heater-generated optical emissions are typically observed).

2.5.2. Results from February 2008 Campaign

As noted earlier, NWRA was the campaign organizer and coordinator for this campaign. Details of this campaign, including a discussion of lessons learned during the campaign operation, have been provided in a separate report (*Kennedy et al.,* 2008). In this report, we will focus solely on the results obtained from NWRA's experiments and participation in experiments run by others.

NWRA was assigned seven experiment time slots during this campaign, and we collaborated with Dr. Keith Groves of AFRL on an eighth. Six of the eight were LEO satellite passes and two were joint LEO and GPS passes. We were also provided time originally assigned to another experimenter for a GPS pass. Table 3 provides a summary of the experiment times NWRA was provided. In this table, the Case column specifies the case number we assigned the experiment (the Milikh case is time assigned originally to Gennady Milikh; the Groves case is the experiment we ran collaboratively with Dr. Groves); the Satellites column indicates which satellites were involved ("G" for GPS with the GPS PRN, "FM" for FORMOSAT, "O" for NIMS, and "F" for DMSP); the Program column indicates the configuration of the IRI beam; the Freq column is the IRI frequency; and the UT and AST columns provide the date and start/end times of the IRI use. The three programs shown were STD for our "standard" program of CW O-mode with the beam directed to the geomagnetic zenith, NS for a beam elongated in the north-south direction aligned with the array geometry (also CW O-mode), and 30sOnOff is the standard mode with a 30-seconds on, 30-seconds off operation.

Table 3. NWRA February 2008 Campaign Experiment Times.

Case	Satellites	Program	Freq MHz	UT			AST		
				Date	Start	End	Date	Start	End
Milikh	G21	STD	3.4	21-Feb	19:25:00	19:45:00	Thu, 21-Feb	10:25:00	10:45:00
1	FM6/G23	STD	2.84	22-Feb	03:47:00	04:13:00	Thu, 21-Feb	18:47:00	19:13:00
2	FM6	STD	4.5	22-Feb	20:22:00	20:46:30	Fri, 22-Feb	11:22:00	11:46:30
3	O32	STD	5.2	23-Feb	22:40:00	23:04:30	Sat, 23-Feb	13:40:00	14:04:30
4	O25	NS	4.2	24-Feb	01:31:00	01:55:30	Sat, 23-Feb	16:31:00	16:55:30
5	F15	NS	3.4	24-Feb	17:50:00	18:15:00	Sun, 24-Feb	08:50:00	09:15:00
Groves	O23	NS	5.2	24-Feb	22:17:00	22:47:00	Sun, 24-Feb	13:17:00	13:47:00
6	FM5	NS	4.8	25-Feb	00:02:00	00:25:00	Sun, 24-Feb	15:02:00	15:25:00
7	F15	STD	2.7	25-Feb	03:44:00	04:10:00	Sun, 24-Feb	18:44:00	19:10:00
7	G23	30sOnOff	2.7	25-Feb	04:10:30	04:18:00	Sun, 24-Feb	19:10:30	19:18:00

Data were collected from both the Gakona fixed-asset ITS10S receiver and the NWRA ITS30m mobile receiver for most of these time periods. Data were also collected from NWRA's HAARP GPS GIOS receiver for Dr. Gennady Milikh, and have provided Dr. Milikh with the raw data from his experiment times.

2.5.2.1. Experiment with DMSP F15 Overflights

Two experiments were run during the campaign making use of the two-frequency beacon and in-situ instrumentation on the Defense Meteorological Satellite Program (DMSP) F15 satellite. The clearest example of a possible feature generated by the HAARP IRI can be seen in results obtained from a DMSP F15 pass near the HAARP facility around 0400 UT on 25 February 2008. The beacon data collected from this pass proved to be unusable for extracting scintillation information, but data from the in-situ instruments shows what may well be a density

structure at the satellite altitude (nominally 840 km) generated either directly or as a by-product of HAARP IRI heating in the F-region.

Figure 25 shows the geometry of this pass and of the IRI heated region as configured during the time of the pass. The left panel shows the track of the DMSP pass as mapped down field lines (using IGRF 2005) to an altitude of 220 km, the nominal F2-layer altitude at the time, and the 3-dB and 6-dB contours of the IRI beam at that same altitude. The heavy line indicates the location of the structure we will be studying. The right panel shows the satellite track at the nominal satellite altitude of 840 km and the IRI beam contours at that altitude. Geomagnetic conditions were very quiet during this pass, and the SuperDARN radar from Kodiak showed that the ionosphere was free of meter-scale irregularities in the vicinity of HAARP aside from those generated by the IRI.

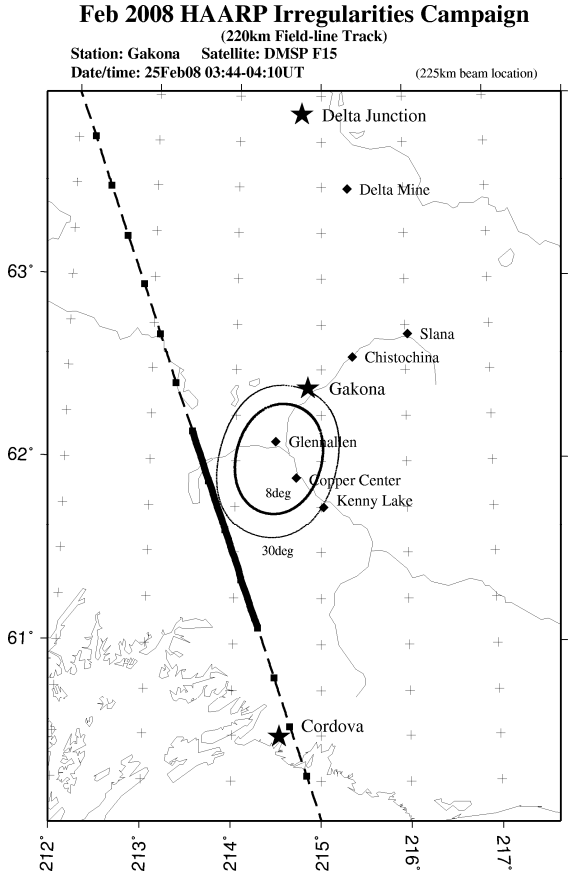

Figure 25. Track of DMSP F15 field line, mapped to 220-km altitude, for pass at 0400 UT on 25 February 2008 (dashed and solid line). Solid section of this track indicates the section of patch in which a possible IRI-produced feature was found. The two ovoids are the 220-km 3-dB and 6-dB contours of the IRI heater as configured for this experiment.

Data from the F15 in-situ instruments are shown in Figures 26a (ion density) and 26b (drift velocity and ion temperature). The structure of interest is in the center of these plots, clearly seen in the bottom panel of Figure 26a. This is an isolated structure in the pass data, and while it does not map directly into the F-layer region in which the IRI is interacting, it is very near to it. Our tentative hypothesis is that the larger-scale structure, as seen in the bottom panel of Figure

26a, is plasma that has been moved along the field line from lower altitudes, with the finer-scale structure evident in the top panel of Figure 26a more probably generated locally due to plasma instabilities, possibly a gradient-drift instability. The fact that one side of the larger structure has this finer-scale structure than the other is symptomatic of this type of instability in isolated density structures. The coincident onset of upwelling evident in the vertical drift velocity (center panel of Figure 26b) is consistent with this picture, as is the decrease in ion temperature evident in the lower panel of Figure 26b.

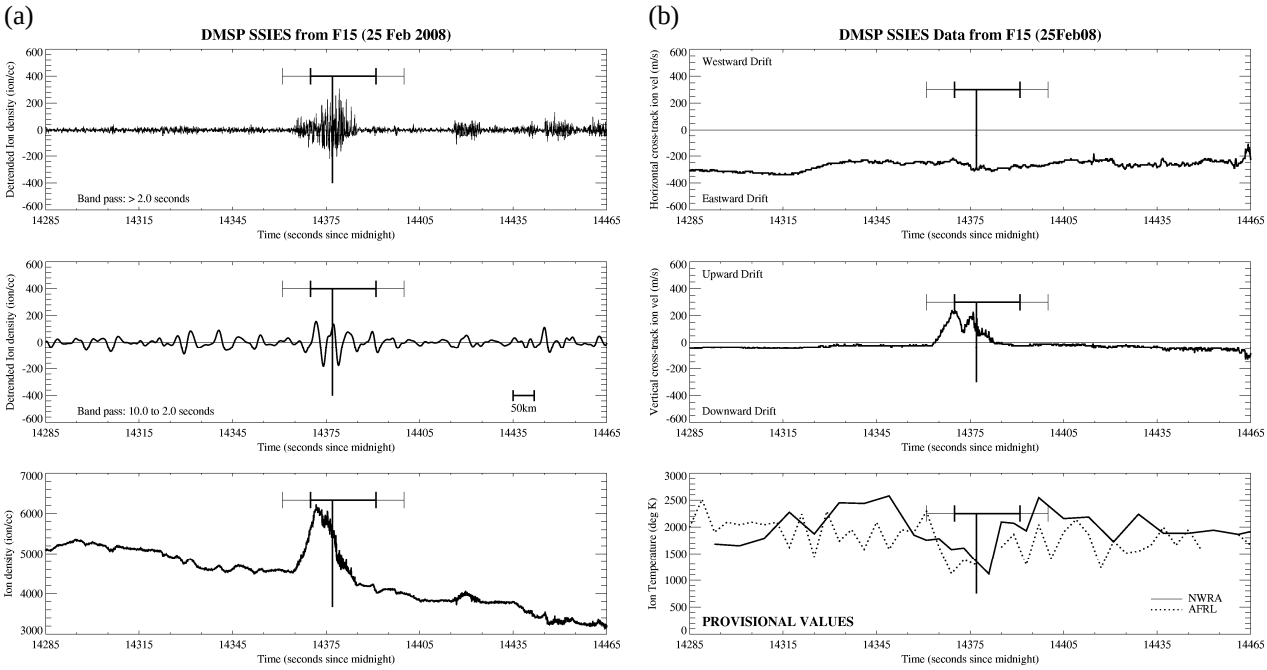

Figure 26. Data from the DMSP F15 SSIES instruments from the pass shown in Figure 25. (a) Data from the SSIES Scintillation Meter (SM) instrument. The bottom panel shows the total ion density, the top panel the output of a digital filter applied to the ion density data with a band pass > 2.0 seconds (a detrended version of the lower panel), and the middle panel shows the output of a digital filter with a band pass of 2.0 to 10.0 seconds. (b) Data from the SSIES Drift Meter (DM) (top two panels) and Retarding Potential Analyzer (RPA) (bottom panel) instruments. The top two panels show the horizontal and vertical cross-track ion drifts, respectively, and the bottom panel shows a provisional estimate of the ion temperature from two sources (AFRL and NWRA analyses). In all panels, the heavy vertical line indicates closest approach to the center of the HAARP IRI heated region, the heavy horizontal lines indicate the period that the DMSP satellite was within the 3-dB contours of the heater beam (mapped to 840-km altitude), and the light horizontal lines indicate the time that the satellite was within the 6-dB contours

A critical question that must be answered in order to confirm that this structure is indeed due to IRI interactions is how the structure was formed. Options include (1) direct interaction between the IRI beam and the ionosphere either at, or very near, the satellite altitude, (2) bulk transport of plasma from below the satellite altitude along the field line by either changing the thermal equilibrium along the field line or by changing the electric field structure along the field line, or (3) some form of "spoofing" of the DMSP instruments by direct interaction with the IRI RF signal.

While all of these have strong and weak points, we believe that option 3 is unlikely but should be verified with engineers familiar with the DMSP instrumentation. The fact that the

horizontal cross-track velocity shows no feature where the vertical velocity shows a sharp change in the flow characteristics, and the uneven distribution of the effect on all parameters in the region where the satellite is within the IRI beam at 840-km altitude (as indicated on all plots in Figure 26), are, we believe, strong circumstantial evidence that this is unlikely to be spoofing. Similarly, we also believe option 1 to be unlikely, unless a plausible mechanism for the interaction can be proposed given the IRI operating mode and frequency. One observation against this option is that there was no change in the electron temperature as measured by the Langmuir probe on DMSP (data not shown).

We believe that one of the scenarios in option 2 is the most likely, although, whether the plasma transport is due to thermal or electrodynamical processes is not clear at present. If the plasma in the feature has been transported from lower in the ionosphere without any loss, if we assume a scale height of about 150 km and a Chapman profile the density difference between the center of this feature and the density away from the feature would correspond with densities roughly 50 km below the satellite altitude when outside the feature. With an upward velocity of 200 m/s, that infers a transit time on the order of four minutes, which is well within the time frame of the experiment. We will be working with Dr. Brenton Watkins and his student, Chris Fallen, at the University of Alaska Geophysical Institute to use their one-dimensional model of the expected behavior of the dynamics along the field line to sort out the different processes that could lead to the generation of this structure.

2.5.2.2. Dual-Receiver LEO Satellite Observations

NWRA ran a series of experiments with a variety of LEO satellite passes using both the fixed-position ITS10S receiver located at the HAARP site (designated the Gakona receiver) and the new mobile ITS30m receiver (designated the Mobile receiver) which was deployed in a rented SUV at a number of locations around the site. AFRL (Dr. Keith Groves) also had a new ITS30m receiver deployed at this campaign, which was deployed in tandem with the NWRA Mobile receiver in order to check out this new receiver as a sort of shake-down cruise. The ITS30m deployments were under the guidance of NWRA consultant Mr. Frank Smith, who also assisted the AFRL team that deployed Dr. Groves' ITS30m receiver. Mr. Smith also spent a considerable amount of time helping the AFRL team and Dr. Groves sort out problems with their receiver and how it was deployed. A problem was discovered in the A/D converter card in the laptop used by AFRL for data collection from their receiver, and other issues relating to antenna cabling were also resolved.

We were able to collect useful data from several of these experiments, one of which will be presented later in this report. We did encounter problems with several of the satellites, however, that made it difficult or impossible to collect useful data from them:

1. We discovered that not all FORMOSAT-3 (COSMIC) satellites have their beacons turned on when these satellites pass over Alaska. The organization that controls these satellites was requested to have several satellites' beacons enabled, but fewer were on than expected. For future campaigns, the status of these beacons needs to be established further in advance of the campaign with a clearer understanding of which beacons will be on.

2. The signals from the FORMOSAT-3 satellites that we were able to collect showed severe structure due, mostly likely, to the transmitter antenna pattern. The reduction in UHF signal strength in a deep null near overhead passes by these satellites caused all receivers (the fixed

ITS10S and both mobile receivers) to lose lock on the satellite as it reached overhead. Even on passes where the signals were tracked for the entire pass, removing the artificial structure from the antenna pattern from the received signals in order to study the IRI heater-produced structures will be challenging. For this reason, we plan to place a lower priority on FORMOSAT-3 passes in future campaigns.

3. A similar problem with structure was found in the DMSP F15 beacon data. We suspect that this is a combination of both structure in the transmit antenna pattern and interference with the signal by structures on the bottom of the DMSP spacecraft that can block or reflect the beacon signal. We also found small-scale oscillations (order 1-2 seconds) in both the phase and intensity from this beacon, which will make the data very difficult to use for scintillation observations. These issues have been identified to Dr. Paul Bernhardt, NRL, who is the PI for this beacon.

One of the issues we wanted to address as one of our experiments during the campaign was to collect data from two different receiving geometries during the same satellite pass. The goals of this are to (1) have at least one observation not viewing the heated region with a geometry parallel to the local geomagnetic field (avoid the propagation enhancement to scintillation observed when viewing along the local field direction), and (2) sample different regions of the heated region to look at differences in the effects at, and away from, the magnetic zenith during the same heating experiment. Our experiment on 24 February 2008 using the Oscar 25 satellite was designed to look at these issues. We deployed our Mobile receiver away from the HAARP site to provide a different viewing geometry than that available from the Gakona ITS receiver, and we used a new beam geometry developed by Dr. K. Groves of AFRL and Dr. M. McCarrick of BAE Systems. This new geometry spreads the beam in a fan shape with the beam center aimed at the local zenith (not magnetic) and the fan semi-major axis aligned with the array orientation (just east of geographic north).

Figure 27 shows the geometry for this pass and the resulting VHF intensity and VHF/UHF differential phase data collected during this pass. From the IPP track map in Figure 27a, you can see that the IPP from the Mobile receiver (shown in blue) passed through the southern end of the heated region and sampled very near the IRI magnetic zenith position which the Gakona receiver geometry (shown in red) samples the northern end of the heated region well away from the IRI magnetic zenith. The elongated ovoids shown in the map is the mapping of the IRI beam 3-dB and 6-dB contours to a 220-km altitude. The times that the ray paths were within these contours are indicated in the data plots in Figure 27b by horizontal heavy (3-dB) and light (6-dB) lines. The heavy vertical line in these plots indicates where the geometry crosses the semi-major axis of the heated region. Note that this pass proceeded from south to north.

The results seen in the data from the Mobile pass (top two panels in Figure 27b) are similar to those observed in previous IRI experiments using signals from these LEO satellite beacons. The results from the Gakona receiver are different and quite interesting. In particular, the most disturbed section of the pass occurs not when the signal was passing through the heated region, but to the south of that region at a similar latitude to where the effects were seen in the data from the Mobile receiver. We have not fully analyzed this pass yet, but one initial interpretation is that what we are seeing is structure that has been advected out of the heated region by background flow of the ionosphere (which is supported by preliminary analyses of the Digisonde drift data) with a possible suggestion from the magnitude of the enhancement seen in the Gakona phase data that these structures may be elongated across magnetic field lines and along the local

L-shell, and not just along the magnetic field. This is a very preliminary finding which we plan to pursue during the next few months.

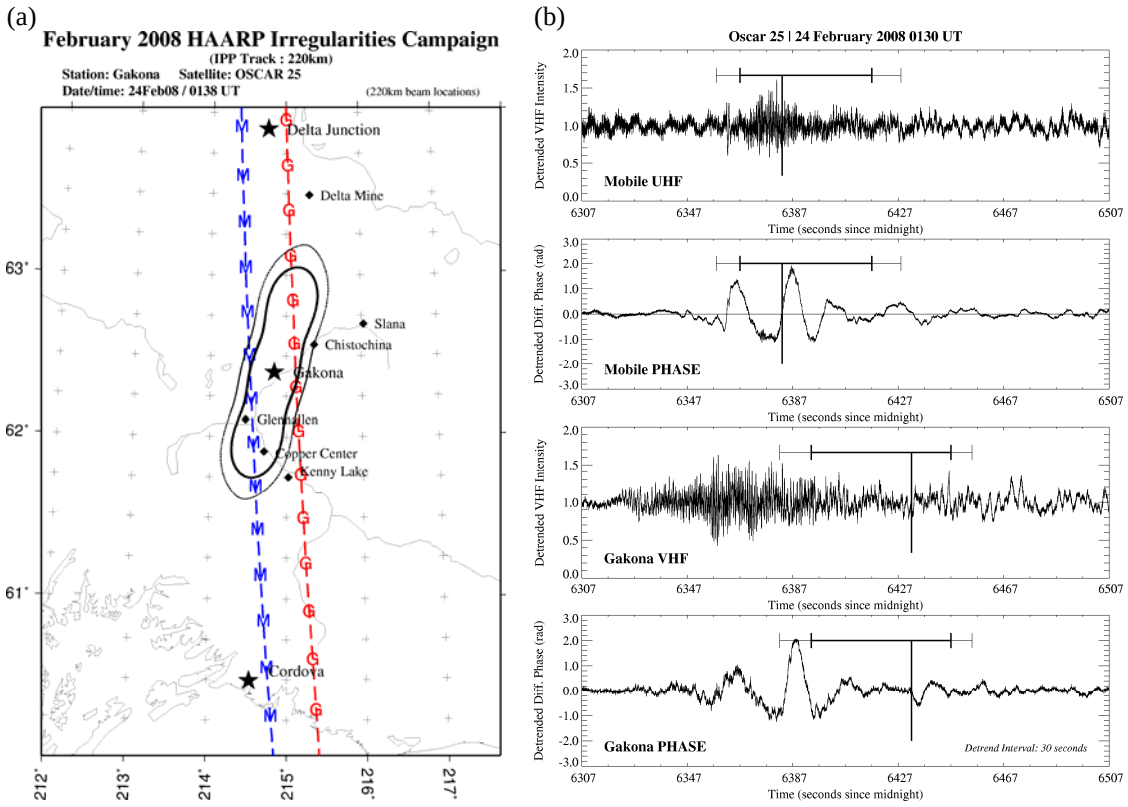

Figure 27. (a) 220-km Ionospheric Penetration Point (IPP) track for the 24 Feb 2008 Oscar 23 pass for the raypath from the Gakona receiver (in red) and the NWRA Mobile receiver (in blue). The extended ovoid shapes indicate the 3-dB and 6-dB contours of the IRI beam used in this experiment. (b) Detrended (30-second cutoff) VHF intensity and phase as observed from the NWRA Mobile receiver (top two panels), and as observed from the Gakona receiver (bottom two panels. Heavy vertical line indicates closest approach to the IRI beam semi-major axis, heavy horizontal line indicates where the IPP was within the 3-dB contours, and the light horizontal line indicates where the IPP was within the 6-dB contours.

2.5.2.3. GPS Observations

Dr. Gennady Milikh, University of Maryland, ran a series of experiments with the HAARP IRI that employed the NWRA GPS receiver located at the HAARP site as a primary diagnostic. Figure 28 shows the Total Electron Content (TEC) derived from one of Dr. Milikh's experiment periods showing clear evidence of structures generated by the HAARP IRI during the experiment. We have submitted a paper to Geophysical Research Letters describing this result [*Milikh et al.*, 2008].

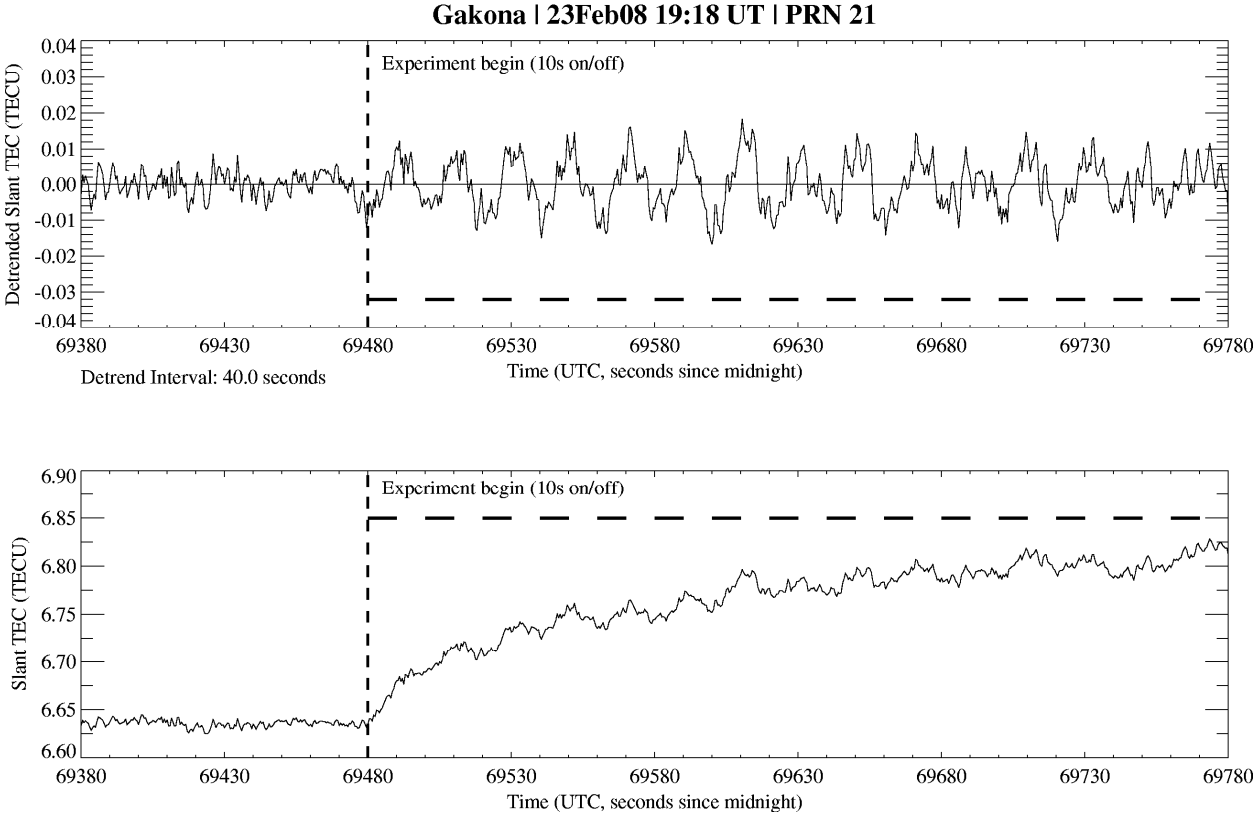

Figure 28. Data from the NWRA HAARP GPS receiver taken during an experiment by Dr. G. Milikh. The bottom panel is the absolute slant-TEC derived from observations of the time-delay and phase-advance on the signals from GPS satellite PRN 21, and the top panel is the data detrended by a high-pass filter with a 40 second cut-off period. The horizontal dashed line indicated times that the IRI transmitter was on and off (10-second intervals).

3. NON-HAARP TOPICS – TECHNICAL AREA 3(A)

Contract work on topics under BAA Technical Area 3(a) during the period covered by this report was focused on two primary areas of interest: (1) ionospheric scintillation, and (2) ionospheric Total Electron Content (TEC) derived from measurements using GPS signals.

3.1. Ionospheric Scintillation Research

Two research efforts were undertaken during the contract period focused on ionospheric scintillation. Continuing the thrust of the work reported in SR1 (Section 3.1.) wherein algorithms for specifying the uncertainty in estimates of scintillation indices calculated by the WBMOD ionospheric scintillation model [*Secan*, 2004] were developed and added to that model, we used several years of scintillation observations collected by the ITS10S receiver located at the HAARP site in Gakona, AK, to assess the performance of the WBMOD model at an auroral station. Results of that work were provided in a separate report (*Secan,* 2005).

The second effort in this area consisted of two studies looking at ionospheric scintillation models and assessed their performance in terms of scintillation observations made by several systems which are operationally impacted by the effects of scintillation. The results of these studies are presented in Appendix D to this report.

3.2. Use of GPS Signals to Derive Ionospheric TEC

The use of radio beacons on satellites to measure the Total Electron Content (TEC) between the ground and the satellite dates back to the first artificial satellite, Sputnik I, in 1957 (*Al'pert et al.,* 1958). This parameter became of interest to the DoD community as TEC provides a useful observation for estimating the impact of the ionosphere on a wide range of communications and surveillance systems which make use of the transionospheric propagation channel. In the 1970s and well into the 1990s, a primary source of ionospheric TEC for operational use was a network of polarimeters, which make use of the Faraday rotation effect, established by the U.S. Air Force Cambridge Research Laboratory (AFCRL) for use in models run by the USAF Air Weather Service (AWS) (*Mendillo and Klobuchar, 1974; Flattery and Ramsay,* 1975). With the launch of the first operational Global Positioning System (GPS) satellites in the late 1980s, work was already underway to use the two phase-coherent GPS L-band signals (L1 and L2) as a replacement for the aging polarimeter network (*Klobuchar and Rino,* 1983). This work culminated in the mid 1990s with development and deployment of the USAF Ionospheric Measuring System (IMS) GPS-based TEC systems (*Bishop et al.,* 1994).

While GPS-based TEC was a major advance over the old polarimeter network TEC, there remained two issues to resolve; one that was a carry over of an unresolved issue with the polarimeter-based TEC and a second due to limitations of the polarimeter-based TEC. The first issue is how to use TEC, an integral measure, to updated models of the full electron density profile. This will be an issue for any system that measures TEC. The second issue is a somewhat artificial one, although important in an operational setting. The polarimeter-based TEC was able to measure TEC only to an altitude of 1,500 to 2,000 km due to the weighting effect of the earth's magnetic field on the Faraday rotation phenomenon on which these TEC measurements were made (*Titheridge,* 1972). This limitation led to an artificial "cap" on the upper altitude range of models used by the USAF AWS; a limitation that carried forward to newer models and that has led to a need for estimates of TEC up to an altitude of 2,000 km. This has been codified into a specification of "ionospheric TEC" to refer to TEC up to this altitude and "plasmaspheric TEC" for TEC from that altitude out to infinity.

The issue of the impact of plasmaspheric TEC also has ramifications on the ability to convert TEC observed to GPS satellites from a measure along a raypath of any orientation (called slant TEC) to an estimate of the equivalent-vertical TEC. This was also a parameter used by older AWS models, and the process of converting from slant TEC to equivalent-vertical TEC is a key part of the process developed for the IMS system to estimate the biases in differential group delay (DGD) estimates of TEC due to uncalibrated delays (between the L1 and L2 signals) in both satellites and receivers (*Bishop et al.,* 1995), known as the SCORE process (for Self Calibration Of Range Errors). The effect of plasmaspheric TEC on this process is described in *Lunt et al.,* [1999]. A preliminary method for dealing with this problem, which also addressed the issue of separating the TEC into ionospheric and plasmaspheric components, was developed by NWRA and denoted SCORPION (SCOre for Plasmasphere and IONosphere) (*Mazzella et al.,* 2002).

The original plan for this effort was to continue development of the SCORPION algorithm as a way to resolve at least the issue of partitioning GPS slant TEC into an equivalent-vertical ionospheric TEC and a plasmaspheric TEC. That effort was funded by AFRL via a Small Business Innovative Research contract (*Rao,* 2004; *Rao and Mazzella,* 2007). To complement that separate effort, and to address issues other than the partitioning of TEC into ionospheric and

plasmaspheric components, three parallel efforts were conducted under this contract looking at improving use of GPS TEC data:

1. Expanding on an existing data-assimilation system, the GPS Ionospheric Inversion (GPSII) program (*Fridman and Nickisch,* 2001), to deal with the issue of converting GPS slant TEC measurements into electron density profiles and, as a side effect, with the partitioning issue as well.

2. Expand the existing SCORE processing to look at data from a chain of stations along a longitude sector to assess the performance of SCORE in dealing with the impact of the plasmaspheric TEC during solar minimum conditions.

3. Begin work to codify and quantify the various sources of uncertainty in GPS TEC measurements (both slant and equivalent-vertical).

4. Deploy GPS systems to a high latitude station (Clear AFS, AK) to run the SCORPION analysis software to both test and demonstrate that the SCORPION system provided realistic bias results at a location where there should be little, or no, contribution from the plasmasphere.

We were fortunate in that there were a number of opportunities to test and exercise the new capabilities developed under these efforts to meet the needs of AF users. Appendix E describes extensions made to GPSII to better use GPS TEC data and several applications of this new technology to specific applications. We were also able to make use of the GPSII developments to provide an extensive analysis of data in the west European longitude sector in support of analysis by a DoD agency of the performance of radar systems in the UK (the spacetrack radar at Fylingdales). The work on assessing the performance of SCORE from a chain of stations along the west cost of the U.S. and our work to quantify uncertainty in GPS TEC measurements were leveraged to provide support for a validation and calibration effort for the DMSP SSUSI ultraviolet spectrometer sensor. In this section, we will provide an overview of the SCORE system developed for our research, describe the two efforts just mentioned, and the data-collection deployment to Clear AFS, in the context of the core focus of the overall effort to improve the use of GPS TEC measurements.

3.2.1. SCORE Test and Analysis Implementation

As a precursor to the research planned that would make use of the SCORE analysis system, we spent some time developing a more flexible implementation of the SCORE process that would provide a more user-friendly and extensible platform for use not only in our planned research, but also for future use. The existing SCORE implementation was tied strongly to the real-time implementation used in the IMS system, and the test implementation that had been derived from the operational implementation was complicated to set up and cumbersome to use. There was also very limited information available upon which to base assessments of how well the analysis worked and the uncertainty in the TEC generated by the analysis. The existing implementation was also tied to the Windows operating system, and we wanted a system that could run on a wide range of platforms.

The decision was made to build the analysis system around the existing Fortran codes that make up the SCORE analysis system, making only those changes to these codes as necessary to add capabilities not currently in existence. The scripting codes that were built to run these programs, however, were to be completely rewritten. For the sake of portability, we decided to

use the python scripting language for the majority of the processing scripts (wherein lies most of the expertise in running the SCORE Fortran programs) and the Generic Mapping Tools (GMT) package for all display generation. Both of these are freely available over the Internet, and provide support on all major computing platforms. The system was also designed to present a range of graphical outputs in a form that is easily accessible by standard Internet browsers such as Microsoft's Internet Explorer and the Mozilla Firefox browser. One final constraint on the system was that it would be designed such that replacing the SCORE bias-determination process by the SCORPION process should be relatively simple. For our needs, we tested the new codes on Windows (XP), Linux, and Unix (Solaris) systems. As a starting point for the core processing script, we used a script that had been developed by S. Rao for testing the SCORPION system [Rao, 2004].

Details for this rather elaborate system, which covers the processing from downloading RINEX data files from sites around the Internet to display of both TEC data and a range of diagnostics and tools for repackaging the TEC data for delivery to other users, are described in detail in formal documentation written for this system and delivered to AFRL (*Secan and Holland,* 2008). This report will describe this system at a high functional level, focusing mostly on the new tools developed for assessing performance and in ways it has been used in two capabilities demonstrations. Examples of the primary displays that this system is capable of producing are presented in Appendix F to this report.

The system is designed such that it can be used to download RINEX-format data from any repository of RINEX data files on the Internet, process the data using the SCORE system, generate a number of displays from the resulting analysis, store the results of the analysis in an archive database system, and post the displays in a cross-linked web site for ease in viewing. This process can be configured to do one day for a single station or multiple days for a collection of stations. A number of tailored versions of this system were developed in the course of the research conducted on this contract, ranging from a hands-on one station-day per run setup, to a fully automated system that downloads, processes, and stores data from a chain of stations on a daily basis without human intervention.

The tools developed to aid in assessing the performance of the bias-calibration process and the uncertainties in the TEC derived based on those biases can be categorized as follows:

1. Displays of the resulting equivalent-vertical TEC that are simple to generate and easy to use.

2. Statistics generated from the TEC produced by the process

3. Comparison of the biases generated by the SCORE (or SCORPION) process with biases from other days or from other sources.

4. Comparison of the TEC generated with TEC from other sources.

Looking at the display examples shown in Appendix F, Figures F1 and F2 are in the first category; parts of Figures F1 and F2 (the average and standard deviation parameters included in these plots) and Figure F4 are in the second category; Figures F3, F8, and F9 are in the third category, and Figures F5, F6, and F7 are in the fourth category. The set of Figures F1 through F4 can be generated routinely and posted to a cross-linked web site for review, as can Figures F5 through F6 if data are available from the JASON spacecraft (see Section 3.2.3.). The other figures can be generated automatically, but they are set up to be used by what we refer to as a

"skilled analyst" to use in assessing how well or poorly SCORE (or SCORPION) has performed on a particular data set.

This concept of the "skilled analyst" is a stepping stone to a more automated system for assessing overall performance. The plan is that by using these tools manually to determine how the system is behaving, we will be able to identify which of the various metrics we have established for assessing system performance could be worked into an automated system. At this time, the expertise in this area is at the level of a person who understands both the SCORE system and the behaviors and limitations of GPS TEC data, who can look at the various displays and output parameters and make a judgment as to whether the biases generated for a given day, and the resulting TEC, are good or not. Some of the outputs, such as the average TEC as a function of local solar time and the standard deviation of the individual TEC observations about this mean, can be used as preliminary assessments of quality and uncertainty, and have been provided as such to end users (see Section 3.2.3.). Further automation of this process will require further work with these tools.

3.2.2. Western Europe Sector GPSII Analysis

An earlier demonstration test of an early version of the SCORE implementation just described and of the GPSII system described in Appendix E was afforded by a request from a USAF agency for analysis of data from several time periods around solar maximum to be used in assessing the performance of new software developed for early warning radars to mitigate the impact of the ionosphere on radar operations. By the end of this effort, we provided estimates of ionospheric TEC along user-specified ground-to-satellite ray paths covering three two-week periods: 05 to 19 January 2002, 09 to 23 June 2001, and 27 March to 10 April 2001. For each day of these two-week periods, RINEX data for a set of stations in a region centered over the United Kingdom and reaching into northern Africa on the south, eastern Europe on the east, Scandinavia on the north, and southern Greenland on the west, was downloaded and processed by the SCORE implementation to provide an initial analysis and then, by the GPSII system, to provide grids of electron density profiles from which TEC along any trajectory within the grid could be easily calculated.

While the SCORE output was not used directly in generating the end product (TEC along specific trajectories), it was used to identify stations that had data-quality issues and as a cross-check to the TEC produced by the GPSII analysis to insure that the newer technology in the GPSII software was producing estimates of satellite and receiver biases that were consistent with those estimated by the SCORE process. We used SCORE as a pre-selector tool because it ran much quicker than GPSII and works with one station independent of all other data. This allowed us to make a quick-look assessment of the data to be used with no possibility that odd behavior at any one given station was being caused by data problems at some other station that was part of the same analysis. The cross-check of the biases generated by the two approaches provided a "sanity check" on the more complex GPSII analysis.

Plots of the daily TEC similar to those shown in Figures F1 and F2 were generated for both the SCORE analysis and, when the analysis output became available, for the GPSII analysis. The GPSII software was modified to provide, as a diagnostic output, the TEC produced by the "forward model" within GPSII for GPS TEC corresponding to each input GPS TEC. If the two processes were generating completely consistent estimates for TEC, the plots would be identical. Two differences in how these systems operate make an identical analysis unlikely. First, the

SCORE process converts the observed slant TEC into an equivalent-vertical TEC, while the GPSII process generates the vertical TEC estimates by a true vertical integration, thus, there are differences due to known deficiencies in the process used within SCORE. Second, the SCORE process analyzes the data one station at a time, with no attempt made to reconcile the results with results from other stations, while GPSII attempts to find solutions that provide the best possible fit to all stations for which it has data. The SCORE plots were used initially in the input-data QC process in which we eliminated unsuitable stations. After the GPSII data were available, cross-comparisons were made to insure that the GPSII analysis was generating realistic grids of ionospheric electron density in the analysis region.

All trajectory data were generated and provided to the USAF customer by the end of May 2007. This exercise assisted us in refining several of the tools we had developed for the SCORE implementation, and led to several improvements to the GPSII software, as described in Appendix E. One major improvement was in the runtime of the GPSII code, which was decreased by over a factor of two in order to handle the large volume of data employed in this analysis.

3.2.3. SCORPION Performance at Auroral Latitudes

Shortly after the study described above, we were provided an opportunity to deploy a GPS receiver system operating the NWRA GIOS (GPS Ionospheric Observing System) software package to Clear AFS, AK, in support of a USAF test activity, Combat SPACETRACK Integration Node Global Enhanced Radar (STINGER). Rather than the usual SCORE calibration package, the system was deployed with a real-time version of the SCORPION calibration package which had just been completed under an SBIR contract (*Rao and Mazzella*, 2007). The system was deployed to Clear AFS in mid-July 2007, and installed and operated by NWRA consultant. Mr. Frank Smith, of Northwest Research Engineering (NRE). Data was collected in conjunction with tests run using the radar system located at Clear AFS as part of the Combat STINGER testing for the period 24 through 29 July 2007.

The GPS TEC data collected was calibrated in real-time using the SCORPION software run in a mode designed to replicate the results that would be obtained from SCORE. This run mode was designed to be used when the data were being collected at a location far enough poleward of the plasmasphere boundary that there should be no, or minimal, impact by the plasmasphere on the calibration operation. This deployment provided an opportunity to collect data at such a location to test the real-time operation of SCORPION using this run mode.

The performance of SCORPION was assessed by comparing the estimates of the combined receiver and satellite biases obtained by SCORPION in the field with estimates generated by the production version of SCORE analyzing the data after-the-fact. The processing system developed for testing SCORE performance, as described in the previous section, modified to use data from the GIOS system rather than RINEX-format data, was used for this testing. For the six-day period of the test, the RMS difference between the SCORPION and SCORE estimates of the biases was 0.10 TECU, and all were within 1 TECU. The majority of the large differences occurred on the initial day of the data collection, and appear to have been due to problems getting the data collection process started. These problems were not reflected in the SCORE processing, so the two analysis systems were working with slightly different data sets for that day. Overall, the comparison showed that SCORPION operating in a SCORE mode (ionosphere only) performs as well as the production version of SCORE. This was the desired outcome, as

SCORE has proven to be as good a process as any available for determining the biases from a single station in near real-time.

The Combat STINGER program needed to have these observations in a form that was more easily used in their post analysis software. We obtained the services of a consultant, Dr. Rob Daniell, to take the data we had collected and provide Combat STINGER with the analyses in the format they needed. These data were delivered to AFRL for delivery to the Combat STINGER team in September 2007.

3.2.4. SCORE West-Coast US Analysis

The SCORE implementation reached its full maturity in a final application in which RINEX data from a chain of stations along the west coast of the United States was analyzed using SCORE to provide estimates of TEC for use in a calibration and validation (cal/val) study of TEC data produced by the new DMSP Special Sensor Ultraviolet Spectrographic Imager (SSUSI). We used this opportunity to extend the tools already developed and to develop additional tools to allow us to compare TEC derived from the SCORE system with TEC from another source, the JASON oceanic altimeter data. Many of the graphical tools shown in Appendix F were developed for this effort, which has greatly expanded the toolkit available for assessing both the performance of the SCORE system and quantifying the uncertainty in TEC derived by that process. Table 4 lists the nine stations for which data were provided, and Table 5 lists the days in 2007 for which slant-range TEC data were provided for each of the nine stations in Table 4. All data identified by these two tables were provided to AFRL and Aerospace during the report period.

Table 4. List of stations for which slant-range TEC data derived from GPS observations were provided.

Station		Geographic		Geomagnetic		Mlat Difference	
Name	**ID**	**Lat**	**Lon**	**Lat**	**Lon**	**To South**	**To North**
Neah Bay	neah	48.30	235.38	54.08	293.93	1.94	N/A
Fort Stevens	fts1	46.21	236.04	52.14	295.43	1.48	1.94
Corvalis	corv	44.59	236.69	50.66	296.70	2.75	1.48
Yreka	ybhb	41.73	237.29	47.91	298.28	3.49	2.75
Petaluma	p198	38.26	237.39	44.42	299.47	2.48	3.49
Bakersfield	bkr1	35.13	240.89	41.94	304.09	2.17	2.48
Point Loma	plo5	32.67	242.76	39.77	306.72	7.61	2.17
La Paz	lpaz	24.14	249.68	32.16	315.89	4.58	7.61
Colima	col2	19.24	256.30	27.58	323.40	N/A	4.58

Table 5. Dates for which slant-TEC data derived from the chain of stations shown in Table 4 were provided.

# Days	Data Days (2007)	
	Start	End
40	30-Mar-07	08-May-07
11	21-May-07	31-May-07
14	12-Jul-07	25-Jul-07
21	10-Sep-07	30-Sep-07
12	15-Dec-07	26-Dec-07

Figures F5 through F7 show a set of analysis displays that were developed to facilitate the comparison of GPS TEC derived using SCORE and TEC derived from the JASON data. Figure F5 is a composite plot, so named because the GPS TEC shown is a composite of GPS TEC data averaged to provide a comparison with the JASON data. This composite average (the line of black error bars) is generated by selecting those GPS TEC values that are within a user-selected spatial and temporal distance from the track along which JASON data are available (the line of solid blue dots) and creating a weighted average, where the weighting is dependent on the distance (spatial and temporal) between the GPS TEC observation and the JASON TEC observation. The width of the error bars on the GPS TEC points is given by the weighted standard deviation of the GPS TEC data used to generate the average. The green points along the bottom of this plot indicate the difference between the GPS composite TEC and the JASON TEC. Note that previous analyses of TEC estimates calculated from the JASON altimeter data found that JASON-derived TEC overestimates the actual TEC by 4-5 TECU (*Bishop*, private communication).

Figures F6 and F7 provide an in-depth look at the individual GPS TEC data that were used in generating the average GPS TEC shown on Figure F6. The difference between these two figures is the plot in the lower-right quadrant of the figure. In Figure F6, the location of the GPS TEC values and the location of the JASON track are shown as a function of azimuth and elevation angle from the site, in this case St. John's, Newfoundland. In Figure F7, this is replaced by a plot of the locations in latitude and longitude, with the sub-satellite track location used for the JASON data and the 350-km Ionospheric Penetration Point (IPP) used for the GPS TEC data. The purpose of these plots is to provide an analyst a more detailed look at the locations of the GPS TEC data with respect to the JASON TEC locations (in space and time) and of the scatter of the GPS TEC as a function of local time and latitude.

A detailed look at some of the results derived from this effort, including a multi-station version of the plot shown in Figure F5, is presented in *Bishop et al.* [2008]. This preliminary look at the performance of SCORE and the impact of the plasmasphere during solar minimum conditions showed that these new tools will be useful for assessing the overall performance of the SCORE process and, eventually, the SCORPION process.

4. PUBLICATIONS AND PRESENTATIONS

The following publications and presentations were based on the work completed during the report period:

Kuo, S. P., M. Rubinraut, Y.-L. Wu, Theoretical study of the cascade spectral features of HFPLs in HAARP heating experiments, presented at the RF Ionospheric Interactions Workshop, Santa Fe, NM, Apr 2006.

Kuo, S. P. Basis of ionospheric modification by high-frequency waves, *Progress in Electromagnetics Research, PIER 73*, 277-296, 2007.

Kuo, S. P., and D. Greco, Determination of the height of the modulated electrojet region generating ELF radiation, *Geophys. Res. Lett., 34,* L05103, doi:10.1029/2006GL029124, 2007.

Kuo, S. P. S. S. Kuo, J. T. Huynh, and P. Kossey, Precipitation of trapped relativistic electrons by amplified whistler waves in the Magnetosphere, *Phys. Plasmas, 14(6),* 009706 (1-7), 2007.

Kuo, S. P., S. S. Kuo, J. T. Huynh, Double cyclotron resonances for whistler wave amplification and electron precipitation in the magnetosphere, presented at the RF Ionospheric Interactions Workshop, Santa Fe, NM, Apr 2007.

Kuo, S. P., Y.-L. Wu, R. Pradipta, J. A. Cohen, and M.-C. Lee, VLF wave generation by amplitude-modulated HF heater waves at Gakona, Alaska, *Geophys. Res. Lett., 35,* L13101 (1-5), doi:10.1029/2008GL034414, 2008.

Kuo, S. P., and M.-C. Lee, Cascade of Langmuir waves in HAARP heating experiments, presented at the 29th General Assembly of URSI, paper # 1796, Chicago, USA August 7-16, 2008.

Kuo, S. P., M. Rubinraut, Y.-L. Wu, R. Pradipta, J. A. Cohen, M.-C. Lee, Frequency dependence of VLF wave generation at Gakona, Alaska, presented at the 29th General Assembly of URSI, paper # 1799, Chicago, USA August 7-16, 2008.

Kuo, S. P., S. S. Kuo, J. T. Huynh, Whistler wave mitigation of energetic electrons in the magnetosphere, presented at the 29th General Assembly of URSI, paper # 1801, Chicago, USA August 7-16, 2008.

Pryse, S. E., E. L. Whittick, A. D. Aylward, H. R. Middleton, D. S. Brown, M. Lester, and J. A. Secan, Modelling the tongue-of-ionization using CTIP with SuperDARN electric potential input: Verification by radiotomography, submitted to *Annales Geophys.*¸Jul 2008.

Rubinraut, M., D. Greco, S. P. Kuo, A technique to determine the source region of ELF\VLF wave generation by modulated HF heater, presented at the RF Ionospheric Interactions Workshop, Santa Fe, NM, Apr 2006.

Rubinraut, M., and S. P. Kuo, Generation of energetic electrons at harmonic cyclotron resonances in HF heating experiments, presented at the RF Ionospheric Interactions Workshop, Santa Fe, NM, Apr 2006.

Rubinraut, M., Y.-L. Wu, and S. P. Kuo, Locating the electrojet source region in ELF wave generation, presented at the RF Ionospheric Interactions Workshop, Santa Fe, NM, Apr 2007.

Secan, J. A., and E. J. Fremouw, TEC and Scintillation Observations During HAARP Daytime Operations, poster presented at the 12th Annual Ionospheric Interactions Workshop, Santa Fe, NM, Apr 2006.

Secan, J. A., HAARP Irregularities Campaign Plans, presented at the 13th Annual Ionospheric Interactions Workshop, Santa Fe, NM, Apr 2007.

Secan, J. A., Feb/Mar 2008 HAARP Campaign Summary, presented at the 14th Annual Ionospheric Interactions Workshop, Boulder, CO, Apr 2008.

Secan, J. A., F. J. Rich, K. R. Martin, Evidence of IRI-generated structure at 840-km altitude in DMSP in-situ observations, poster presented at the 12th Annual Ionospheric Interactions Workshop, Boulder, CO, Apr 2008.

Whittick, E. L., S. E. Pryse, H. R. Middleton, J. A. Secan, and A. D. Aylward, Radiotomography observations of large scale high-latitude ionospheric structure by the IITC: influence of IMS, season, and longitude, presented at the European Geosciences Union General Assembly 2008, Vienna, Austria, Apr 2008.

Wu, Y.-L., M. Rubinraut, and S. P. Kuo, Experimental and numerical studies of whistler wave generation by amplitude-modulated HF heating waves, presented at the RF Ionospheric Interactions Workshop, Santa Fe, NM, Apr 2007.

Appendix A
Tomography Image Coverage

Tables A1 through A5 provide a summary of images generated from the Alaskan tomography network from 2004 through 2008 (31 July), respectively, as a function of month. The upper panel separates the images by the set of stations used to generate each image. The entries in the columns under "Stations" indicate which stations contributed to the image; for example, the top row lists images generated from the station-set Kaktovik, Fort Yukon, and Delta Junction. The bottom panel shows the percentage of images in each month that included data from the station listed in the left-most column.

Note that the decrease in the number of images and in the number of stations from the chain in these images towards the end of the report period were due to two factors: (1) the primary satellites used for the tomography work, the Navy Ionospheric Measuring System (NIMS), or Oscar, satellites, are beginning to go off the air; and (b) the two UAF GI stations, Kaktovik and Delta Junction, became highly unreliable and then left the air completely during 2007 and 2008.

Table A1. Station-Availability Summary for Tomographic Images in 2004

Number of Images

Stations							Jan	Feb	Mar	Apr	May	Jun	Jul	Aug	Sep	Oct	Nov	Dec	All
Kak		For	Del				0	0	0	0	0	0	0	0	0	0	1	0	1
Kak			Del	Gak			0	0	0	0	0	0	0	1	0	0	2	0	3
		For	Del	Gak			0	0	0	0	0	0	0	0	0	0	2	0	2
Kak		For				Cor	0	0	0	0	0	0	0	0	1	1	0	0	2
Kak			Del			Cor	0	0	0	0	0	0	0	0	1	0	0	0	1
Kak				Gak		Cor	0	0	0	0	0	0	1	21	28	0	0	0	50
		For		Gak		Cor	0	0	0	0	0	0	0	0	5	1	0	0	6
	Arc			Gak		Cor	0	0	0	0	0	0	0	0	0	0	0	7	7
			Del	Gak		Cor	191	132	148	128	108	89	130	76	17	56	47	3	1125
Kak		For	Del	Gak			0	0	0	0	0	0	0	0	0	1	1	0	2
Kak		For		Gak		Cor	0	0	0	0	0	0	0	0	15	0	0	0	15
Kak	Arc			Gak		Cor	0	0	0	0	0	0	0	0	0	0	0	2	2
Kak			Del	Gak		Cor	0	0	0	0	0	0	9	38	13	38	21	1	120
		For	Del	Gak		Cor	0	0	0	0	0	0	0	0	6	13	7	0	26
	Arc		Del	Gak		Cor	0	0	0	0	0	0	0	0	0	0	48	111	159
Kak	Arc	For	Del			Cor	0	0	0	0	0	0	0	0	0	0	1	0	1
Kak		For	Del	Gak		Cor	0	0	0	0	0	0	0	0	22	67	29	0	118
Kak	Arc		Del	Gak		Cor	0	0	0	0	0	0	0	0	0	0	27	76	103
	Arc	For	Del	Gak		Cor	0	0	0	0	0	0	0	0	0	0	4	4	8
Kak	Arc	For	Del	Gak		Cor	0	0	0	0	0	0	0	0	0	0	27	31	58
						Summary	191	132	148	128	108	89	140	136	108	177	217	235	1809

Percent of Images Including Specific Stations

Station	Jan	Feb	Mar	Apr	May	Jun	Jul	Aug	Sep	Oct	Nov	Dec	All
Kaktovik	0	0	0	0	0	0	7	44	74	60	50	46	26
Arctic Village	0	0	0	0	0	0	0	0	0	0	49	98	19
Fort Yukon	0	0	0	0	0	0	0	0	45	46	33	14	13
Delta	100	100	100	100	100	100	99	84	54	98	100	96	95
Gakona	100	100	100	100	100	100	100	100	98	99	99	100	100
Copper Center	0	0	0	0	0	0	0	0	0	0	0	0	0
Cordova	100	100	100	100	100	100	100	99	100	99	97	100	99

Table A2. Station-Availability Summary for Tomographic Images in 2005

Number of Images

Stations							Jan	Feb	Mar	Apr	May	Jun	Jul	Aug	Sep	Oct	Nov	Dec	All
Kak		For		Gak			0	0	0	0	2	3	15	79	71	15	3	0	188
	Arc	For		Gak			0	0	0	0	1	0	0	0	0	0	0	0	1
Kak			Del	Gak			7	0	2	2	7	0	0	0	0	0	6	2	26
		For	Del	Gak			0	0	0	0	0	0	0	0	0	0	0	2	2
	Arc		Del	Gak			1	2	0	57	0	0	0	0	0	0	0	0	60
Kak		For				Cor	0	0	0	0	0	0	0	28	0	0	0	2	30
Kak	Arc					Cor	1	0	0	0	0	0	0	0	0	0	0	0	1
	Arc		Del			Cor	0	0	2	0	0	0	0	0	0	0	0	0	2
Kak				Gak		Cor	0	0	0	0	24	79	27	1	0	21	0	2	154
		For		Gak		Cor	0	0	0	0	2	6	8	1	0	4	0	0	21
	Arc			Gak		Cor	0	0	0	0	0	1	0	0	0	1	0	0	2
			Del	Gak		Cor	18	57	18	7	16	0	0	0	0	1	7	9	133
Kak	Arc	For		Gak			0	0	0	0	0	0	0	0	0	1	0	0	1
Kak		For	Del	Gak			0	0	0	0	1	0	0	0	0	1	23	5	30
Kak	Arc		Del	Gak			3	1	0	32	0	0	0	0	0	0	0	0	36
Kak		For		Gak		Cor	0	0	0	0	74	62	102	7	0	64	2	0	311
Kak	Arc			Gak		Cor	0	0	0	0	0	0	0	0	0	2	0	0	2
Kak			Del	Gak		Cor	12	37	15	4	7	0	0	0	0	10	44	53	182
		For	Del	Gak		Cor	0	0	0	0	0	0	0	0	0	0	2	4	6
	Arc		Del	Gak		Cor	111	70	134	47	0	0	0	0	0	0	0	0	362
Kak	Arc	For		Gak		Cor	0	0	0	0	0	0	0	0	0	11	0	0	11
Kak		For	Del	Gak		Cor	0	0	0	0	10	0	0	0	0	50	92	110	262
Kak	Arc		Del	Gak		Cor	62	37	84	32	2	0	0	0	0	1	0	0	218
	Arc	For	Del	Gak		Cor	0	0	0	0	1	0	0	0	0	0	0	0	1
Kak	Arc	For	Del	Gak		Cor	0	0	0	0	1	0	0	0	0	4	1	0	6
Summary							215	204	255	181	148	151	152	116	71	186	182	188	2050

Percent of Images Including Specific Stations

Station	Jan	Feb	Mar	Apr	May	Jun	Jul	Aug	Sep	Oct	Nov	Dec	All
Kaktovik	39	36	39	38	86	95	94	99	100	96	95	92	71
Arctic Village	82	53	86	92	3	0	0	0	0	10	0	0	34
Fort Yukon	0	0	0	0	62	47	82	99	100	80	67	65	42
Delta	99	100	100	100	30	0	0	0	0	36	97	97	65
Gakona	99	100	99	100	100	100	100	75	100	100	100	98	98
Copper Center	0	0	0	0	0	0	0	0	0	0	0	0	0
Cordova	94	98	99	49	92	98	90	31	0	90	81	95	83

Table A3. Station-Availability Summary for Tomographic Images in 2006

Number of Images

Stations							Jan	Feb	Mar	Apr	May	Jun	Jul	Aug	Sep	Oct	Nov	Dec	All
Kak		For	Del				1	0	0	0	0	0	3	0	0	0	0	0	4
Kak	Arc		Del				0	0	0	1	0	0	0	0	0	0	1	0	2
	Arc	For	Del				0	0	0	0	0	0	0	0	0	1	0	0	1
Kak			Del	Gak			4	1	0	0	0	2	0	0	0	0	0	2	9
		For	Del	Gak			0	0	0	0	0	0	0	0	0	1	0	0	1
	Arc		Del	Gak			0	1	1	1	0	1	0	3	1	4	2	2	16
Kak		For				Cor	0	0	0	0	1	0	0	0	0	0	0	0	1
Kak			Del			Cor	2	1	1	1	2	0	0	0	0	0	0	1	8
	Arc		Del			Cor	0	0	0	0	0	0	1	2	1	2	0	0	6
Kak				Gak		Cor	0	4	2	1	0	0	0	0	0	0	0	3	10
		For		Gak		Cor	0	0	0	0	0	0	0	1	0	2	0	1	4
	Arc			Gak		Cor	0	2	2	0	0	1	0	2	1	12	1	5	26
			Del	Gak		Cor	19	6	2	3	24	2	4	9	3	8	5	22	107
Kak		For	Del	Gak			1	0	0	0	0	1	1	0	0	0	0	0	3
Kak	Arc		Del	Gak			0	2	3	9	0	2	4	2	0	0	0	0	22
	Arc	For	Del	Gak			0	0	0	0	0	0	0	0	0	2	0	0	2
Kak		For	Del			Cor	2	0	0	0	4	0	0	0	0	0	0	1	7
Kak	Arc		Del			Cor	0	1	3	2	0	0	0	0	0	0	0	0	6
	Arc	For	Del			Cor	0	0	0	0	0	0	0	1	2	0	0	0	3
Kak		For		Gak		Cor	0	0	0	0	0	0	0	1	0	0	1	3	5
Kak	Arc			Gak		Cor	0	5	8	1	2	2	0	0	0	0	1	2	21
	Arc	For		Gak		Cor	0	0	0	0	0	1	0	1	1	5	2	3	13
Kak			Del	Gak		Cor	53	25	9	17	17	12	6	1	0	0	4	6	150
		For	Del	Gak		Cor	4	0	0	0	37	1	3	3	3	3	1	2	57
	Arc		Del	Gak		Cor	0	11	36	9	2	6	18	26	38	31	16	41	234
Kak	Arc	For	Del	Gak			0	0	0	0	0	1	2	4	0	0	1	1	9
Kak	Arc	For		Gak		Cor	0	0	0	5	2	2	0	0	0	0	3	4	16
Kak		For	Del	Gak		Cor	89	0	0	1	35	23	8	10	0	0	3	5	174
Kak	Arc		Del	Gak		Cor	0	103	107	110	7	42	21	15	0	0	25	21	451
	Arc	For	Del	Gak		Cor	0	0	0	1	7	11	22	14	64	35	15	2	171
Kak	Arc	For	Del	Gak		Cor	0	0	0	18	19	57	41	27	0	0	36	5	203
						Summary	175	162	174	180	159	167	134	122	114	106	117	132	1742

Percent of Images Including Specific Stations

Station	Jan	Feb	Mar	Apr	May	Jun	Jul	Aug	Sep	Oct	Nov	Dec	All
Kaktovik	86	87	76	92	55	86	64	49	0	0	64	40	63
Arctic Village	0	77	91	87	24	75	81	79	94	86	88	65	69
Fort Yukon	55	0	0	13	66	58	59	50	61	46	52	20	38
Delta	100	93	93	96	96	96	100	95	98	82	93	84	94
Gakona	97	98	97	97	95	100	97	97	97	97	99	98	97
Copper Center	0	0	0	0	0	0	0	0	0	0	0	0	0
Cordova	96	97	97	93	100	95	92	92	99	92	96	96	96

Table A4. Station-Availability Summary for Tomographic Images in 2007

Number of Images

Stations							Jan	Feb	Mar	Apr	May	Jun	Jul	Aug	Sep	Oct	Nov	Dec	All
Kak	Arc			Gak			1	0	0	0	0	0	0	0	0	0	0	0	1
	Arc	For		Gak			0	0	0	0	5	1	3	0	0	0	0	0	9
Kak			Del	Gak			3	4	0	0	0	0	0	0	0	0	0	0	7
		For	Del	Gak			0	0	0	0	0	0	0	11	0	1	1	0	13
	Arc		Del	Gak			3	4	12	0	0	0	2	12	5	1	1	3	43
	Arc	For				Cor	0	0	0	0	0	0	1	0	0	0	0	0	1
		For	Del			Cor	1	0	0	0	0	0	3	0	1	1	0	1	7
	Arc		Del			Cor	5	1	0	0	0	0	0	0	6	3	4	6	25
		For		Gak		Cor	0	0	0	0	3	19	31	0	1	0	0	0	54
	Arc			Gak		Cor	2	7	33	136	87	67	18	0	1	0	0	0	351
			Del	Gak		Cor	39	6	2	0	6	0	15	59	58	58	40	59	342
Kak		For	Del	Gak			1	0	0	0	0	0	0	0	0	0	0	0	1
Kak	Arc		Del	Gak			3	16	16	0	0	0	0	0	0	0	0	0	35
	Arc	For	Del	Gak			0	0	0	0	0	0	1	2	0	0	0	1	4
Kak		For	Del			Cor	1	0	0	0	0	0	0	0	0	0	0	0	1
	Arc	For	Del			Cor	1	0	0	0	0	0	0	0	8	0	0	0	9
Kak		For		Gak		Cor	1	0	0	0	0	0	0	0	0	0	0	0	1
Kak	Arc			Gak		Cor	1	4	1	0	0	0	0	0	0	0	0	0	6
	Arc	For		Gak		Cor	0	0	0	3	34	25	32	0	0	0	0	0	94
Kak			Del	Gak		Cor	25	18	4	0	0	0	0	0	0	0	0	0	47
		For	Del	Gak		Cor	2	0	0	0	0	0	31	44	14	8	15	9	123
	Arc		Del	Gak		Cor	39	9	46	10	1	0	13	43	86	102	83	65	497
Kak	Arc	For	Del	Gak			0	1	0	0	0	0	0	0	0	0	0	0	1
Kak		For	Del	Gak		Cor	5	0	0	0	0	0	0	0	0	0	0	0	5
Kak	Arc		Del	Gak		Cor	23	52	55	0	0	0	0	0	0	0	0	0	130
	Arc	For	Del	Gak		Cor	1	0	0	0	0	0	39	41	39	29	38	12	199
Kak	Arc	For	Del	Gak		Cor	1	3	1	0	0	0	0	0	0	0	0	0	5
						Summary	158	125	170	149	136	112	189	212	219	203	182	156	2011

Percent of Images Including Specific Stations

Station	Jan	Feb	Mar	Apr	May	Jun	Jul	Aug	Sep	Oct	Nov	Dec	All
Kaktovik	41	78	45	0	0	0	0	0	0	0	0	0	12
Arctic Village	50	77	96	100	93	83	57	46	66	66	69	55	70
Fort Yukon	8	3	0	2	30	40	74	46	28	19	29	14	26
Delta	96	91	80	6	5	0	55	100	99	100	100	100	74
Gakona	94	99	100	100	100	100	97	100	93	98	97	95	98
Copper Center	0	0	0	0	0	0	0	0	0	0	0	0	0
Cordova	93	80	83	100	96	99	96	88	97	99	98	97	94

Table A5. Station-Availability Summary for Tomographic Images in 2008 (Through July)

Number of Images

Stations							Jan	Feb	Mar	Apr	May	Jun	Jul	Aug	Sep	Oct	Nov	Dec	All
		For	Del	Gak			0	2	0	0	0	0	0						2
	Arc		Del	Gak			1	1	1	0	11	6	15						35
	Arc		Del			Cor	0	1	1	3	16	1	1						23
	Arc			Gak		Cor	3	0	1	0	4	6	1						15
			Del	Gak		Cor	30	50	28	24	13	41	45						231
		For	Del	Gak		Cor	0	2	0	1	0	0	0						3
	Arc		Del	Gak		Cor	88	53	90	128	105	99	82						645
	Arc	For	Del	Gak		Cor	0	6	11	0	0	0	0						17
Kak	Arc	For	Del	Gak		Cor	0	0	0	0	0	0	0						0
						Summary	122	115	132	156	149	153	144	0	0	0	0	0	971

Percent of Images Including Specific Stations

Station	Jan	Feb	Mar	Apr	May	Jun	Jul	Aug	Sep	Oct	Nov	Dec	All
Kaktovik	0	0	0	0	0	0	0						0
Arctic Village	75	53	78	83	91	73	68						75
Fort Yukon	0	8	8	0	0	0	0						2
Delta	97	100	99	100	97	96	99						98
Gakona	100	99	99	98	89	99	99						97
Copper Center	0	0	0	0	0	0	0						0
Cordova	99	97	99	100	92	96	89						96

Appendix B
ITS Receiver Stations Status

The following summary report of the status of the NWRA-operated ITS tomography receiver chain was provided by NWRA consultant Mr. Frank Smith. NWRA maintains and operates five ITS10S Receiver systems for the HAARP tomography chain. At any time, four of these systems are deployed at sites in Alaska, while the fifth system is a reserve to serve as back-up and a test platform for software or hardware upgrades or trouble-shooting.

B1. Description of ITS Receiver Systems

The five ITS10 receiver systems are nearly identical, comprising a two-band coherent receiver (VHF and UHF), an associated two-band antenna and a computer. The computer controls the operation of and collects data from the receiver, and it, in turn, is remotely accesses to install new software, update the NORAD Two Line Elements (TLE) and adjust various operational parameters.

The VHF Detector section of the receiver is comprised almost entirely of obsolete parts. However, over the years, we have had few failures with this section, but the replacement parts are nearly used up. Another part of the receiver, the Synthesizer, is also made with an obsolete oscillator for which no replacement is available. These oscillators, however, have never failed. The remainder of the receiver, while comprised of 1990's era parts, remains serviceable.

The computers are quite old and obsolete: 300 MHz machines running Windows NT. Additionally, of the two National Instruments cards that interface between the receiver and computer, one is no longer available, and the other has been in production for 13 years, a long run for a National Instruments product. The software suite that runs on these systems is a mixture of old (FORTRAN) and new, but all of the programs operate perfectly well on the latest computer hardware.

B2. Description and Status of the ITS Receiver Stations

Gakona

The ITS10 station at the HAARP site, near Gakona, AK, is the first of the ITS stations to be installed as part of the HAARP operation. This station is the most ideal of all the installations, as RF noise is minimal, a large area is available for a large antenna ground-plane, and the equipment is housed in, and operated from, an equipment shelter specifically designed for scientific observation. Besides power, the facility provides telephone service and high-speed Internet connectivity. The on-call availability of HAARP staff personnel to perform occasional jobs that need hands-on operation is a major benefit for this site location.

Delta

The Delta station, the second Alaska ITS station, was installed in December 1999 at the Silver Fox Roadhouse. Initially, there were multiple problems with receiver tuning, antenna cabling and very noisy telephone service. It took a year and several visits to resolve the problems but, since then, the Delta station has been very reliable. The Silver Fox Roadhouse is a gas station / convenience store with rental cottages, mostly used by recreational hunters. The receiver is located in a small back room away from activity in the store. The antenna is mounted on a wooden frame with a mesh ground-plane similar to the one at Gakona.

Delta is the most RF-quiet location of all the sites. Moreover, since a fiber-optic telephone cable was installed along the highway outside, communication has been very reliable. We have the option of installing a DSL Modem but, at present, there is no need for this. For the occasional service to the system, we have always had the assistance of the owner of the Silver Fox, Mr. Dan Splain.

Cordova

The Cordova station was installed in November of 2000. It was first installed at Cordova High School in the City of Cordova, but the student-teacher activities, local RF interference, and occultation of the horizon by the surrounding mountains led to the abandonment of that site. The station was moved to Cordova Auto Rental, a small business operating near the Cordova airport, about 12 miles from the town. Except for a nearby aeronautical navigation beacon, the location is very radio-quiet. (The navigation beacon interference is removed with an RF filter.) The horizon is low in all directions so low-elevation satellite passes are obtainable. The antenna is mounted atop an 8' x 40' steel cargo container, which provides a good ground plane. The receiver and computer are inside the Rental office, inside a TV-enclosure type cabinet. Communication with the Cordova station is via the local telephone cooperative. Cordova Telephone, in turn, communicates with the outside world entirely by satellite communication. There are occasional outages, but they are rarely longer than a few hours.

Other receiver outages (not caused by the Telephone system) usually require the help of someone on-site. For several years, the owner of Cordova Auto provided this service. However, after he sold the operation, a local Cordova resident, Mr. Jim Vansant, has been available to us as the need arises.

Arctic Village

The station at Arctic Village was installed in March, 2004. It began as, and continues to be, a difficult environment from which to gather data. The location of the station is an 8' x 8' science experiment shelter located near the Arctic Village airport. This facility is owned and operated by the University of Alaska, Fairbanks. Indeed, the actual installation and most subsequent work has been by an employee of UAF, Ms. Kay Lawson.

The difficulty at Arctic Village is twofold; communication with the outside world, and radio interference. The facility had (and has) a telephone connection, so initially it was believed that communication would be similar to Cordova. That is, there is a copper telephone connection from the receiver station to the village, and, then, a satellite link to the rest of the world. However, the satellite link is vastly far below Cordova in terms of data transmission speed. The solution was to set up our own link from the station to a second (Internet-only) satellite station within the village. This was done in concert with an Alaska-wide program to provide Internet access to all Alaskans, regardless of the size of the villages they lived in. This system, by itself, works adequately, albeit very slowly at times. The problem is that the Internet connection equipment is, itself, a source of interference to ITS10 operations. The solution here was to program the Internet connection equipment to power-down during a satellite pass. This mode of operation did eliminate the equipment interference, but sometime during the setup, testing, and eventual power-on - power-off operating mode, another source of interference has come into being.

Arctic Village operation remains poor in terms of the amount of useful data obtained from the site. We are investigating an alternative location for this receiver, perhaps at the Toolik Field Site, operated for the National Science Foundation by the University of Alaska at Fairbanks. This site is on the main road from Fairbanks to Prudhoe Bay, and would provide better communications and on-site support.

B3. Receiver Performance / Operational Upgrades

In addition to serving as a back-up, there has always been an effort to perform various feature upgrades on the suite of receivers without specifically bringing them in for service. That is, the back-up receiver will receive whatever upgrades have been deemed useful and, then, whichever field receiver needs service will be replaced with the upgraded receiver. So far, only once has an otherwise functional receiver been replaced solely for the purpose of receiving an upgrade. The computers, while old, are completely adequate to their task. Software revisions and adjustments have been made and installed remotely since the systems were installed.

B4. Routine Operation / Equipment Malfunction

In routine operation, the only interaction required is the weekly sending of the NORAD TLEs to all stations. Of course, with four stations, all operating at remote locations, the out-of-routine is common. The usual cause of interruption of the data stream is either the telephone connections to the three stations that depend on that mode, or a slowdown in the data archiving at the primary server computer located at the HAARP facility. This kind of problem will often seem to fix itself. For example, the local telephone company will fix a downed line.

Once in a while, an individual station will have its modem become inoperative, and a power cycle to the system is required. This is the usual duty of the on-site people that we depend on. More rarely, there will be a component failure in the receiver or even, more rarely, in the computer. When this happens, the disabled equipment is shipped to NWRA's laboratory in Redmond. If the difficulty can be adequately diagnosed remotely, the replacement receiver / computer will first be shipped to the problem site, and the on-site person will remove / replace the unit and return the defective unit.

Appendix C
Classic Riometer Status

The following report on operations and maintenance on the HAARP 30 MHz classic riometer was provided by NWRA consultant Mr. Jens Ostergaard.

C1. Overview

The HAARP 30-MHz classic riometer is one of a wide range of diagnostic instruments at the HAARP research site in Gakona Alaska. Such riometers have been a standard for measurement of ionospheric absorption for many years. The frequency of 30 MHz is widely used, so data from different stations can readily be compared. The HAARP riometer operates with an antenna array of four, 5-element crossed Yagi antennas pointed at Zenith. The 3-dB beamwidth is approximately 60° x 60°. The riometer receiver is a solid-state, noise balancing radiometer receiver with a digitally controlled noise source used for balancing.

The ionospheric absorption is measured as the difference between the Galactic noise background and the measured antenna temperature. The Galactic noise background and its diurnal variation, the Quiet Day Curve, can either be determined from registrations during periods where the ionosphere is very quiet, or it can be computed from maps of galactic noise sources and computer models of the antennas radiation pattern. Both methods have been used during the last three years. Figure C1 shows examples of calculated Quiet Day Curves for various frequencies. The computed Quiet Day Curve is very accurate during the mid-winter and mid-summer months, where the physical environment around the antenna is dry and stable. However, during periods of frost and thaw, especially in the spring, fairly large deviations have been registered on a recurring basis. The deviations include both calibration jumps, and changes in the form of the Quiet Day Curve. The latter suggests changes in the antenna radiation pattern with changes in the environment around the antenna. It has also been noted that hoar frost on the antenna elements may have caused some of the deviations. Figure C2 illustrate how differences in the condition of the soil and snow accumulation can effect the calculated Quiet Day Curve.

Thus, it must be concluded that the current computational model of the Quiet Day Curve needs refinement. During periods of instability, Quiet Day Curves derived from measurements on ionospherically quiet days have been used. The need for a computed Quiet Day Curve arose during the peak of the past solar cycle, where the ionospheric activity was so high, that it was not possible to derive a Quiet Day curve from measurements at all. The past three years have included the least active period of the solar cycle, and a large number of quiet days have been available. This data has been very valuable when evaluating the absolute accuracy of the riometer receiver and the antenna system. This report presents some of the results of the evaluation.

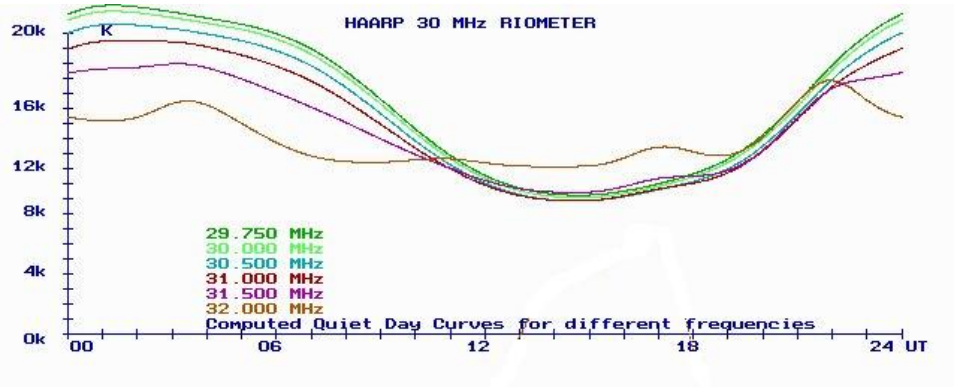

Figure C1. Examples of Quiet Day Curves calculated for the HAARP riometer for a range of frequencies.

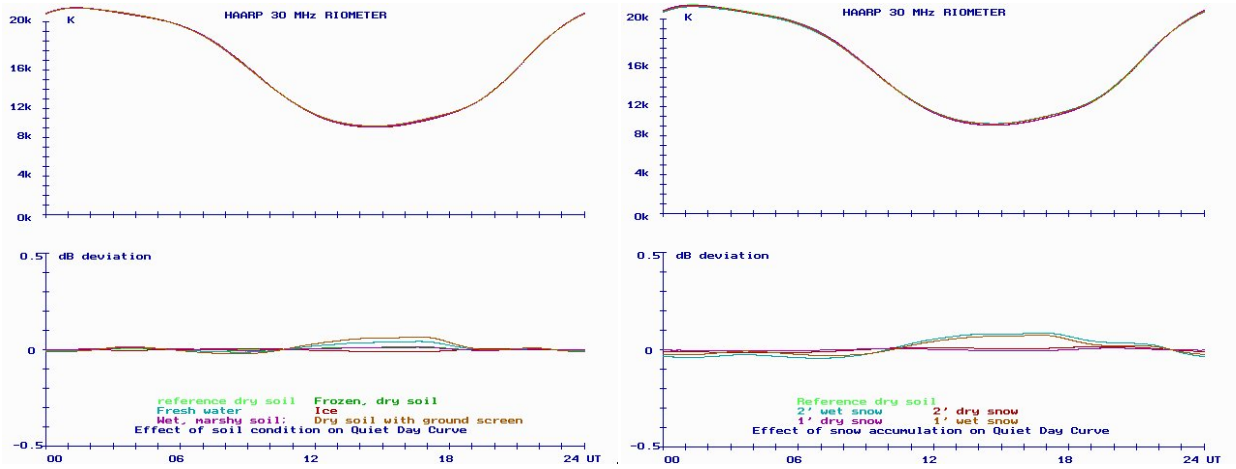

Figure C2. Examples of the impact of varying soil conditions (left-side plots) and varying snow accumulation (right-side plots) on the calculated Quiet Day Curve.

C2. Operational Routine

The riometer operates continuously, and the Quiet Day Curve is included in the operational software. This way, the derived ionospheric absorption is available in real time. Both the measured galactic noise data and the Quiet Day Curve are stored, and the absorption can be reworked at a later date, if the Quiet Day Curve is deemed too inaccurate for a particular use. The riometer operation is checked every day, and calibration jumps, as well as adjustments to the Quiet Day Curve are performed remotely as needed. The best calibration check is a comparison of the Quiet Day Curve with measurements during quiet days. Quiet Day Curve changes are not introduced until the measurements have been observed for some days, and it has become evident that the deviations are caused by the instrument, not ionospheric activity. Weak absorption events, not associated with magnetic disturbances, can be observed at HAARP during late afternoon hours and early evening hours. These events are caused by particles dumped out of the radiation belts. (Dr. Lee Snyder, private communication). It is important not to interpret such events as changes in the Quiet Day Curve.

A site visit is performed once per year. The maintenance work includes antenna leveling. This is necessary, as the guy anchors embedded in the permafrost move slightly every year. The

return loss, i.e. S11 are measured in the frequency band 29.7 MHz - 31 MHz for all antennas and feed systems. A high return loss is the most suitable way to determine if bad connections or corrosion exist in the antennas or the feed system. Deficiencies are repaired as necessary. Finally, the riometer receiver is calibrated with a variable noise source.

C3. Mechanical Failures and Problems

The climate at HAARP is very hard on equipment located outdoors. The riometer antenna array has experienced a number of mechanical problems over the years. The antenna elements, as such, have held up well, and they should last for many more years. There have, however, been a number of failures with the baluns in the feed system. The antennas require a 1:4 step-up balun between the feeder cable and the fed element. The original baluns were made with very thin coaxial cable potted in a hard epoxy. These baluns did have a number of failures most likely due to the internal coax cable being so constrained that the thin inner conductor was torn by the extreme temperature variations at the site. The baluns were replaced a few years ago with standard half-wave coaxial baluns made from RG213 coaxial cable connected with N-connectors to a watertight junction box. All junctions are tightened hard and covered with shrink tubing The new baluns have lasted well for the past three years. The baluns need maintenance during the site visits. The N connectors can work loose, and the shrink tubing does deteriorate with time and needs to be replaced. The coax cables leading from the antennas to the riometer receiver lasted 10 years, but had to be replaced in the spring of 2008 due to cracks in the cable jacket.

It was found in the spring of 2008 that Pad 3 does not drain well during the spring thaw. Large puddles of water covered the pad for a period of many weeks. The pad surface has become uneven and water tends to congregate in the low spots. One such spot is located under the box protecting the riometer receiver, and 1/2" of water was found inside the box at the end of the spring. The low spot will need to be filled in, and the protective box placed on a bed of cinder blocks to keep it above the water during the thaw. All cable transitions into the box have been checked and resealed.

The moisture in the box, in combination with the puddles on the pad, caused problems with the power cables leading from the equipment shelter to the riometer antennas. The GFI relay protecting the cable dropped-out daily. The cable was inspected and tested for galvanic leakage. The cable is in good condition, and no leakage was found. The GFI relay has been replaced. The GFI relay dropouts stopped when the pad dried out in the late spring.

C4. Evaluation of Accuracy

The resolution (R) of a noise balancing radiometer receiver is calculated as:

$$R = \frac{2T}{\sqrt{Bt_i}}$$

where T is the total noise figure, B is the bandwidth, and t_i is the integration time. The total noise figure for the HAARP riometer including feeder losses is 5 dB or approximately 600°K, and the bandwidth is 30 kHz. At the maximum recorded noise level of 22,000°K, the resolution is better than 0.1 dB. Similarly, at 13-dB absorption, the resolution is 0.1 dB; both for an integration time of 1 second. A better resolution is obtained with longer integration times. The long-term, absolute accuracy with the current riometer receiver is not as good. The influence of calibration jumps and presumed antenna pattern changes have, during some periods, introduced a 0.2-dB -

0.4-dB difference between the Quiet Day Curve and measurements during quiet ionospheric conditions. This is not satisfactory. The goal for the overall accuracy of the HAARP riometer is 0.1 dB. The following paragraphs examine some of the sources of these variations.

C5. Properties of the Antenna Array

Extensive modeling of the antenna array radiation pattern has been performed with NEC. The antennas useful frequency range has been determined to cover 29.7 MHz - 31 MHz. The gain in this range varies 0.3 dB, and the low-angle side lobes are well suppressed. The main lobe deteriorates rapidly with an increase in frequency above 31 MHz. At 32 MHz, the front lobe and the low-angle side lobe have equal magnitude and the Quiet Day Curve has degenerated. The gain figures/beamwidth calculations have been corroborated by operating the riometer in a frequency sweeping mode.

A free space, NEC model at 30 MHz shows that the radiation pattern has a respectable front-to-back ratio of 20 dB, and a front gain of 14 dBi. The main beam width is slightly larger than 60 deg. Models, including a ground under the antenna, show a gain variation from 14.4 dBi to 15 dBi dependent on the soil properties used. The highest gain is associated with a perfect ground, the lowest with a dry, sandy soil model. Corresponding small variations in the beam width can also be seen. Quiet Day Curves have been computed based on these models, and a small deviation can be seen at the Galactic maximum part of the curve. The low antenna temperature range of the Quiet Day Curves, where the antenna points farthest away from the ecliptic plane, show a larger variation. The noise distribution over the antenna aperture is very uniform in this area. A slight variation in the gain does not change the antenna temperature, but the associated widening of the beam does. A larger effect is seen if the distance between the ground plane and the antenna is decreased. Again, a perfect ground, or a wet snow pack during the thaw period has a larger effect than a dry and frozen snow/soil model. This could explain some of the noticeable variations in the form of the Quiet Day Curve during the thaw period. Further analysis will be needed to confirm this hypothesis. It is tempting to install a ground screen under the antenna. The materials are available at the site. However, such a screen would be located under the winter snow accumulation, and would not remove the influence of a wet snow pack. Further modeling will be necessary to examine the effects of a combination of a ground screen and the snow cover.

C6. Properties of the Riometer Receiver

The advantage of the Noise Balancing Principle radiometer receiver is that gain variation and variation in the receiver's noise figure are common to both the antenna branch and the noise generator branch. This eliminates calibration concerns for the receiver circuits, detectors and filters. It is still necessary to account for the loss in the antenna feeder, but that is easily measured, and supposedly very stable, unless the cable is damaged. Other sources of calibration drift and instability exist, however. The solid-state noise source used for noise balancing is an avalanche-type diode with an Excess Noise Ratio drift of 0.01 dB/C. That is very little, but over an ambient temperature range of +30°C to -40°C, this could amount to almost 0.1 dB. The HAARP riometer is enclosed in a thermostatic box that eliminates this drift. Other sources are offset voltages in the feed back loop integrator that vary with temperature and time, and gain instabilities in the receivers IF amplifier. Riometers are commonly designed as single conversion receivers with a 10.7-MHz IF frequency. To obtain front-end robustness, most of the signal

amplification is placed in the IF amplifier. This is also the case for the HAARP riometer, where the robustness is needed due to the proximity of the transmitter array. A dual conversion receiver, where more of the signal amplification is moved to either baseband or a low frequency RF amplifier, could eliminate risk of IF amplifier instabilities. A lower IF amplifier gain and a more sophisticated baseband amplifier/detector/integrator is part of the riometer receiver upgrade currently underway.

The riometer data user community has expressed interest in a better time resolution than the current one minute. A sample of data with a time resolution of one second has been collected. Examples of both quiet and highly disturbed periods are included in the data. Analysis of this data is still pending.

C7. Conclusion

Operational experiences with a new riometer receiver have been accumulated throughout the last three years. This period includes the low sunspot part of the solar cycle, and extended periods of quiet ionospheric conditions have been very useful in evaluating and improving the overall accuracy of the HAARP classic 30-MHz riometer. It has been proven that the use of a computed Quiet Day Curve is feasible. However, seasonal calibration jumps still reduce the absolute accuracy more than desirable. The report has outlined the daily and annual operation and maintenance routines; and has presented a number of factors influencing the measurement accuracy. The improvement work is ongoing, and will include work on the ground screen, the antenna supports and revisions of the riometer receiver.

Appendix D
Ionospheric Scintillation Modeling Work

This task was devoted to two major efforts. The first effort involved the use of measurements of total electron content (TEC) from ALTAIR to construct a model of the ionosphere for application to problems involving space based radar. The second effort involved the application and validation of a Matlab version of the multiple phase screen (MPS) propagation code.

D1. Model of the Ionosphere Based on Radar Data

Consider the 1988 PEAK experiment. The 1988 PEAK (Propagation Effects Assessment - Kwajalein) experiment collected ALTAIR dual frequency (VHF and UHF) pulse-by-pulse range measurements during tracks of calibration spheres. The total electron content during these tracks was obtained from the range measurements using the difference in the ranges measured at VHF and UHF, [Knepp and Houpis, 1992]. In 1988, the radar I&Q data was also analyzed to obtain values of the scintillation index and decorrelation time during track of COSMOS 1427, a large Russian calibration sphere. For this track (referred to as PEAK2G), we recently found a binary file (written in 1989) with machine precision TEC measurements. The accuracy of these measurements is limited by the radar receiver noise, not by the computer word length.

In the following we describe a straightforward technique to utilize this dual-frequency ALTAIR radar track data to construct an ionospheric model. Given the model, we then apply an MPS code to predict the scintillation index and decorrelation time. These model predictions are then compared to the actual measurements of scintillation index and decorrelation time. This and other similar comparisons are useful to validate the model.

The PEAK experiment that was conducted in 1988 was originally planned to be the first of two data collections, with the second to occur two years later at solar maximum. The Cold War ended in 1989, and the second data collection experiment was canceled by the Defense Nuclear Agency. Mission Research Corporation was directed to get as much as possible out of the 1988 data and quickly wrap up the program. For this reason, the satellite track referred to as PEAK2G has the only set of measurements of scintillation index, decorrelation time, and coherence bandwidth. These measurements are used in the comparison discussed here.

In the processing described below, the ALTAIR TEC data is used to construct a model of the ionosphere. Then, the MPS code uses this model to calculate the propagation conditions observed at ALTAIR using the measured TEC as the basis of the MPS phase screen. Finally, the experimentally measured scintillation index and the decorrelation time are compared to those values calculated from the MPS simulation. This comparison allows one to determine the usefulness and accuracy of the process used to generate the phase screen representation of the ionosphere.

Fortunately, a file with some relevant TEC data from PEAK2G was available from a backup CD. This file is analyzed here. The file is a Vax binary file and contains TEC measurements and sufficient radar information to generate radar range, azimuth, and elevation. Matlab is used

to quickly develop code to process this data. The data is described in several reports and papers including Knepp and Houpis [1991 and 1992] and Houpis and Nickisch [1991].

The data analyzed here consist of the TEC measured pulse by pulse from simultaneous VHF and UHF range measurements obtained during the track of a Russian calibration sphere in a polar orbit at an altitude of 420 km. The goal of this work is to use the TEC measured in this fashion to generate a realistic phase screen representation of the ionosphere. This phase screen is then used in an MPS propagation simulation to "recreate" the scintillation measurements observed by ALTAIR. In the following, we compare the actual data (measured scintillation index and decorrelation time) with that produced by this phase screen model. Once validated, such a process could then be applied to other transmission frequencies and geometries such as used by space-based synthetic aperture radar.

The presence of receiver noise must be taken into account. Although the signal-to-noise ratio varies during the track, typical values are 20 dB at VHF and 30 dB at UHF. At 20-dB VHF SNR and 30-dB UHF SNR, the range standard deviations (due to noise) at VHF (7-MHz bandwidth) and UHF (18-MHz bandwidth) are 1.52 and 0.18 m, respectively. Using the range measurements to obtain the TEC, the TEC standard deviation is 0.11 TEC units.

Converting the TEC directly into phase for a screen at UHF (422 MHz) gives a standard deviation for the phase of 2.2 radians or 126 degrees. At VHF, the standard deviation is higher by a factor of (422/155). This large an error cannot be handled correctly in the MPS propagation simulation which requires smoothly varying phase from sample to sample. (The criteria for application of numerical MPS techniques is discussed in Knepp [1983].) Thus some creative processing of the original TEC data must be developed to obtain smooth values of phase.

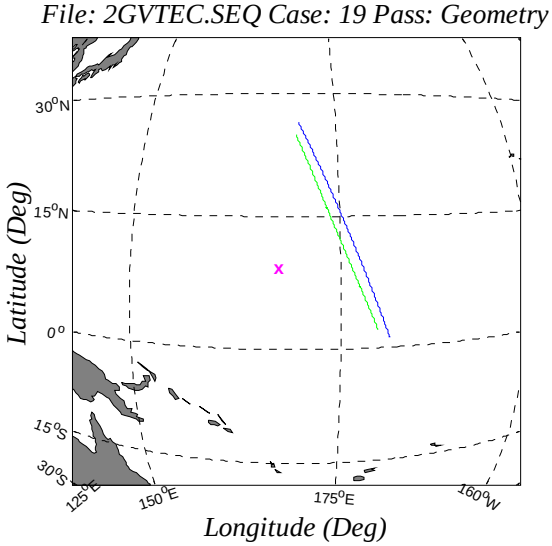

Figure D1. Geometry of pass PEAK2G.

Figure D1 shows the trajectory for PEAK2G. The red x shows the location of the ALTAIR radar, the blue curve shows the latitude and longitude of the satellite, and the green curve shows the latitude and longitude of the ionospheric intercept point at the assumed altitude of 350 km. In order to simulate this geometry with a phase screen, the data here is transformed to obtain the

TEC as a function of distance along the trajectory and perpendicular to the direction of the earth's magnetic field. This is accomplished by converting the latitude and longitude of the trajectory to magnetic latitude and longitude using an earth-centered dipole magnetic field model. Then, the local angle with respect to magnetic North is obtained along the trajectory. For the trajectory in PEAK2G, this angle is approximately constant during the entire track, so the TEC data is easily obtained as a function of distance perpendicular to the earth's magnetic field. The data consisting of TEC versus distance is the basis of the single phase screen representation of the ionosphere to be used here.

For PEAK2G, the angle of the trajectory with respect to magnetic north is 26.5 degrees. To obtain the distance along the trajectory perpendicular to magnetic north, one simply divides the measured distance along the trajectory by the sine of 26.5 degrees. The temporal spacing between radar data samples is variable. Consequently, the spatial separation is also variable. The average spatial separation for PEAK2G is 41.2 meters and the maximum separation is 261.3 meters. Since the separations are not constant, interpolation must be applied in order to obtain the constant spacing necessary to the FFT algorithm in the MPS code. Of course, some filtering of the noise is required prior to the interpolation. Otherwise, the interpolation process will tend to increase the contribution of the noise.

The other required quantity for the MPS code is the propagation distance for the effective phase screen. The MPS code presently models only plane wave propagation a distance Z beyond a phase screen. By the simple lens law, spherical propagation is well-modeled using the expression $Z^* = Z_1 Z_2 / (Z_1 + Z_2)$ where Z_1 is the distance from the transmitter to the phase screen and Z_2 is the distance from the phase screen to the receiver.

The MPS code was initially intended for one-way propagation from a satellite to a ground receiver. To model two-way radar propagation, the calculated voltage is squared (Eq. 12 in Knepp and Houpis, [1991]).

For the PEAK2G data, Figure D2 shows the values of the distances as a function of ALTAIR radar time during the track. The value of Z* ranges from 137 to 187 km during the track. In the MPS calculation, the mean value of 158 km, obtained as the average of all the individual values during the trajectory, is used to specify the constant distance from the phase screen to the receiver plane.

The measured value of slant TEC is multiplied by the classical electron radius and the wavelength to calculate the phase at the radar transmission frequency. Then, to remove some of the noise, we smooth this phase by replacing the values with the output of a 5-point running average. On average, this filters the data over a distance of 5 times 41.2 meters, or 206 meters, which is comparable to the Fresnel zone. The Fresnel zone is the square root of the wavelength times Z*, which at VHF (155 MHz) is 552 meters. Irregularities with sizes on the order of the Fresnel zone contribute most to scintillation. Such filtering will tend to remove structure that is on the order of, and smaller than, the filter length. Too much filtering of the phase will thus tend to remove scintillation-producing irregularities. To better understand the effect of this filtering, we performed a numerical experiment using the MPS simulation.

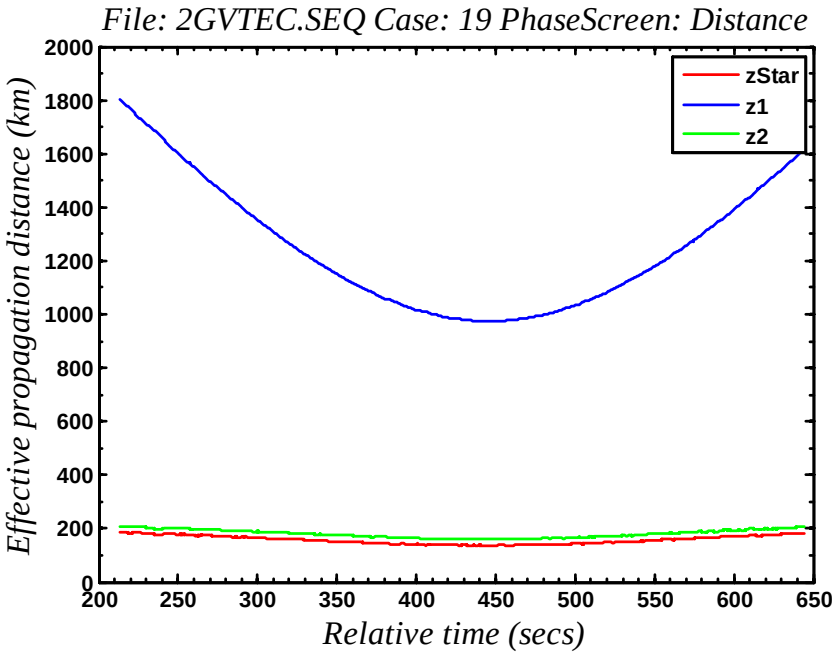

Figure D2. Propagation distances during PEAK2G.

The effect of this filtering depends on the spectrum of the phase. For the phase spectrum of PEAK2G which has a slope of roughly 2.5, we found, by numerical experimentation (discussed below), that the effect of a 5-point smoothing filter is small for the VHF case. For the UHF case, with its smaller Fresnel zone of 335 meters, the effect of the 5-point filter is more important but still minor.

To continue the description of the processing, the filtered phase versus distance is then linearly interpolated to obtain a series of equally spaced phase values separated by a distance of 20.6 meters. For PEAK2G, the original TEC data comprised a series of 31,087 values. The interpolation step described above increases the number of values by about a factor of 2 to 62,175 values.

The final step in the creation of a phase screen model is to increase the total number of points to a power of 2 (131,072 points). For the phase in the additional points, we simply used a linear (straight-line) value connecting the last point to the first point in the periodic repetition of the phase screen. This linear function connects the first and last original phase values so that there is no discontinuity in periodic repeats of the phase screen. Figure D3 shows the complete phase screen at VHF that is used to generate the propagation results presented in this report.

Figure D4 gives a comparison of the VHF phase power spectrum after the filtering and interpolation steps described above. The right-hand frame shows the case of no filtering. The left-hand frame shows the effect on the phase PSD of the 5-point running average filter. The appended linear portion of the phase screen is not used to calculate this power spectrum. The major differences appear at values of wavenumber, q, of 0.004 m^{-1} and above, and are caused by the 5-point running average filter.

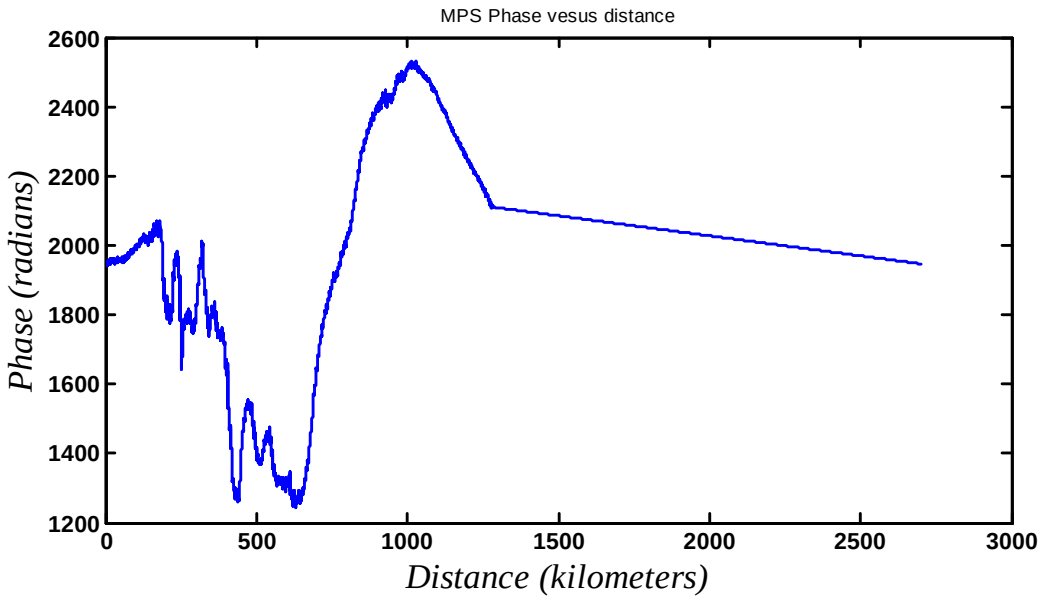

Figure D3. Phase screen representation of PEAK2G.

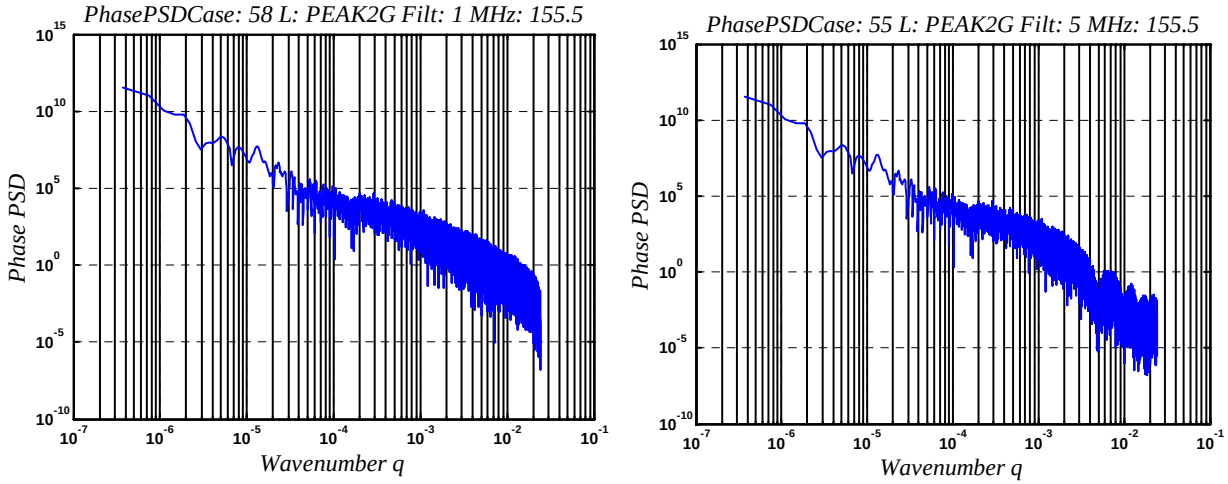

Figure D4. Effect of filtering on the phase PSD.

Figure D5 shows the results of a number of statistical MPS calculations of the scintillation index and the decorrelation distance for a simulation of the PEAK2G data. These results are generated with a number of statistically independent phase screens designed to simulate the power spectrum observed during PEAK2G. The phase screen shown in Figure D3 is not used to generate the data in Figure D5. For this simulation, a phase power spectrum with a slope of -2.5 is used to match the measured power spectrum. The propagation distance, frequency, grid size and grid spacing, and other MPS input parameters match the PEAK2G measurements.

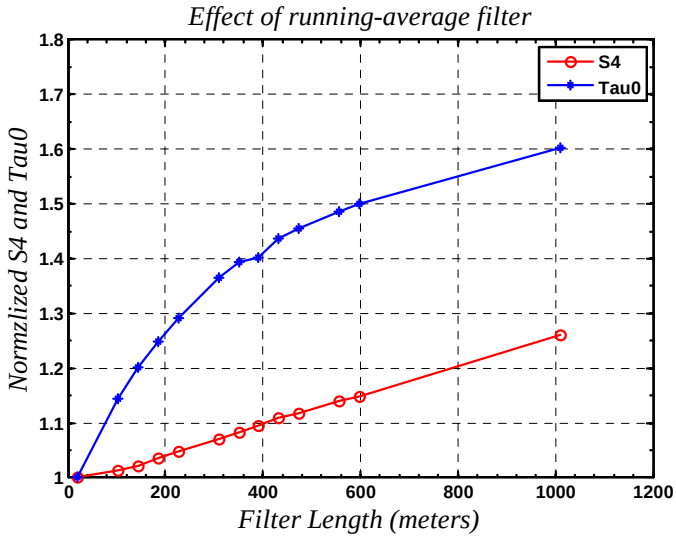

Figure D5. MPS simulation of the effect of the filter on the measured scintillation index and decorrelation time.

Figure D5 shows the effects of filters of various lengths that are used to modify the statistical MPS phase screen prior to the propagation calculation. The quantities plotted are the scintillation index divided by the scintillation index for the case of no phase filtering and the decorrelation distance divided by the decorrelation distance for the case of no filtering. These two quantities are plotted versus the filter length. The plotted parameters increase with increasing filter length because the filter is removing the smaller scale irregularities that produce scintillation but leaving larger scale structure that produces large lenses that give strong focusing and, hence, very large enhancements in power. These enhancements increase the value of scintillation index. As the filter length increases, the overall phase variance decreases, which reduces the total scintillation and thus increases the value of the decorrelation distance.

The results presented in Figure D5 show that the filtering does indeed impact the values of the scintillation index and decorrelation distance and should be avoided, if possible.

In the following, we present a comparison of the ALTAIR data (for RCS, scintillation index, and decorrelation time) versus the output of the MPS propagation calculation that uses the filtered TEC data shown in Figure D3 as the phase screen representation of the ionosphere. A comparison of Figures D6 and D7 show the power versus time of the measured ALTAIR data and the MPS simulation. For these figures alone, a small amount (20-dB SNR) of Gaussian noise is added to the output electric field of the MPS calculation. This additive noise, for plotting purposes only, reduces the depth of some of the deepest fades and gives a noisy power in the portion of the MPS grid where the phase screen is linear (1200 to 3000 km in Figure D3). The level of scintillation is similar in the MPS simulation and the actual data. The major difference in the figures is that the period in the actual data from about 550 to 650 seconds is relatively scintillation-free, while the MPS simulation shows severe scintillation during that same period. This indicates that the 5-point moving average filter did not remove all the phase (or TEC) noise. As discussed above, additional filtering (more than 5 points) would also remove the important phase structure at the Fresnel zone size, which gives the most important contribution to amplitude scintillation.

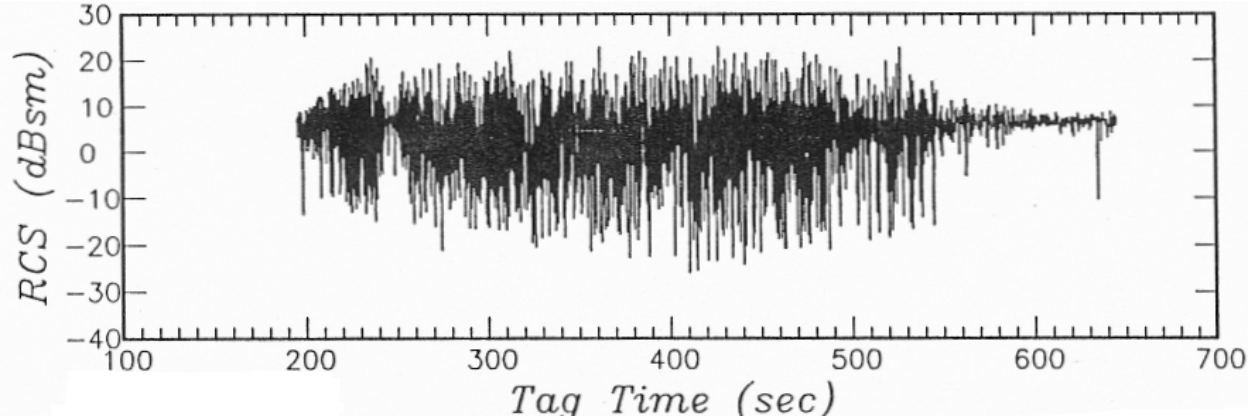

Figure D6. RCS measured at VHF during PEAK2G.

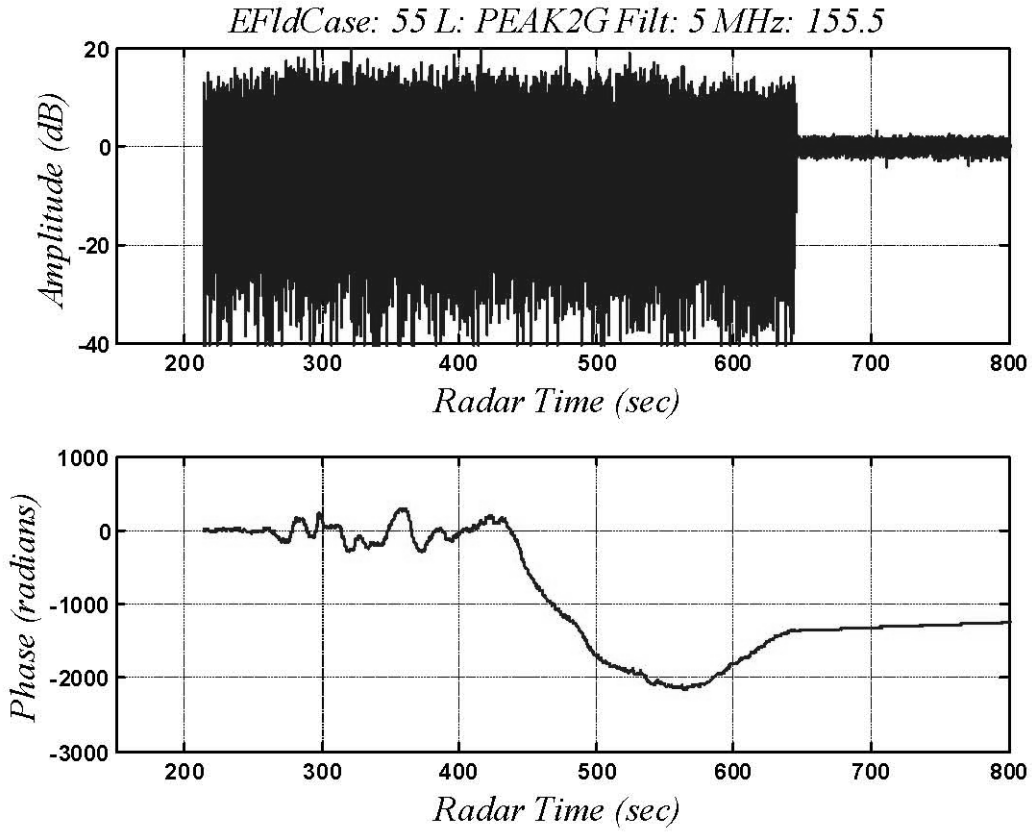

Figure D7. MPS calculation of VHF power and phase.

Figures D8 and D9 show the value of scintillation index versus radar time from the actual data and from the MPS simulation. Roughly the same number of points is used for both calculations. The overall appearance of the curves is similar with the same degree of scintillation severity. However, the simulation fails to predict the reduction in scintillation starting around 550 seconds. In the original data processing used to produce Figure D8, 1000 points are used to calculate a single value of scintillation index. This 1000-point window is then moved in time, and additional values of scintillation index are calculated.

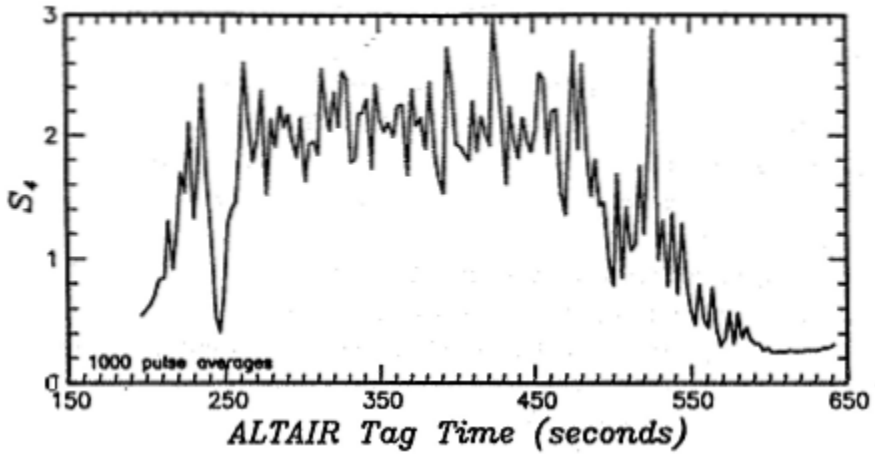

Figure D8. Scintillation index measured at VHF during PEAK2G.

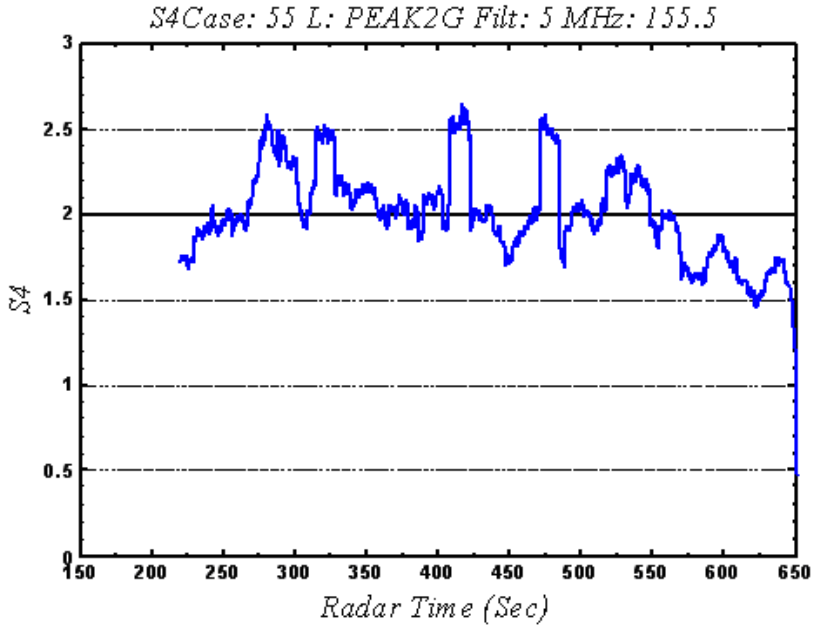

Figure D9. MPS calculation of scintillation index at VHF.

In the simulation, 2000 points are used for this same process because the effective temporal spacing in the simulation is twice that of the original ALTAIR data. The value of scintillation index obtained from these points is plotted in the figure at the center of this data window. The window is moved slightly (one-quarter of its length) and the process is repeated. Thus the values of scintillation index shown in the figure are correlated and the two figures are directly comparable.

Figures D10 and D11 show the value of the decorrelation distance measured using 1024-point FFTs for the data, and 2048-point FFTs for the simulation. A comparison of these two figures indicates that the maximum level of scintillation is similar for the data and the simulation, characterized by a minimum value of decorrelation time of 0.01 sec in both cases. The curves look similar, but the value of decorrelation time in the data is increasing later in the pass at a much higher rate than in the simulation.

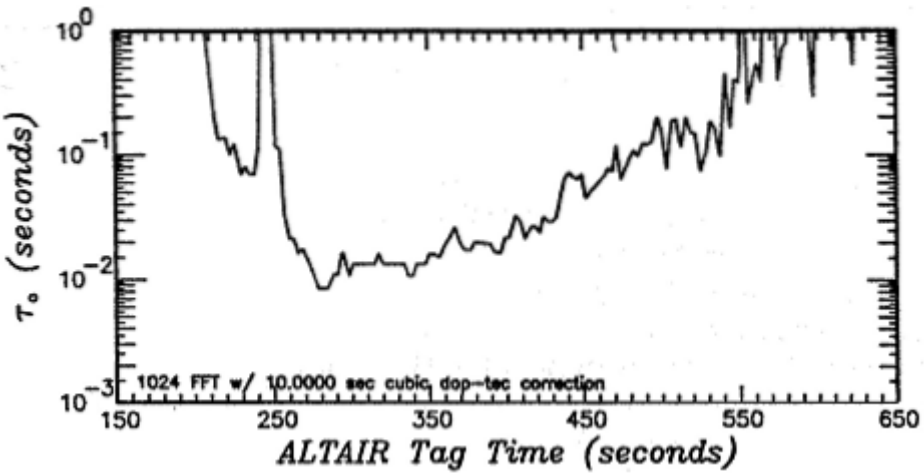

Figure D10. Decorrelation time measured at VHF during PEAK2G.

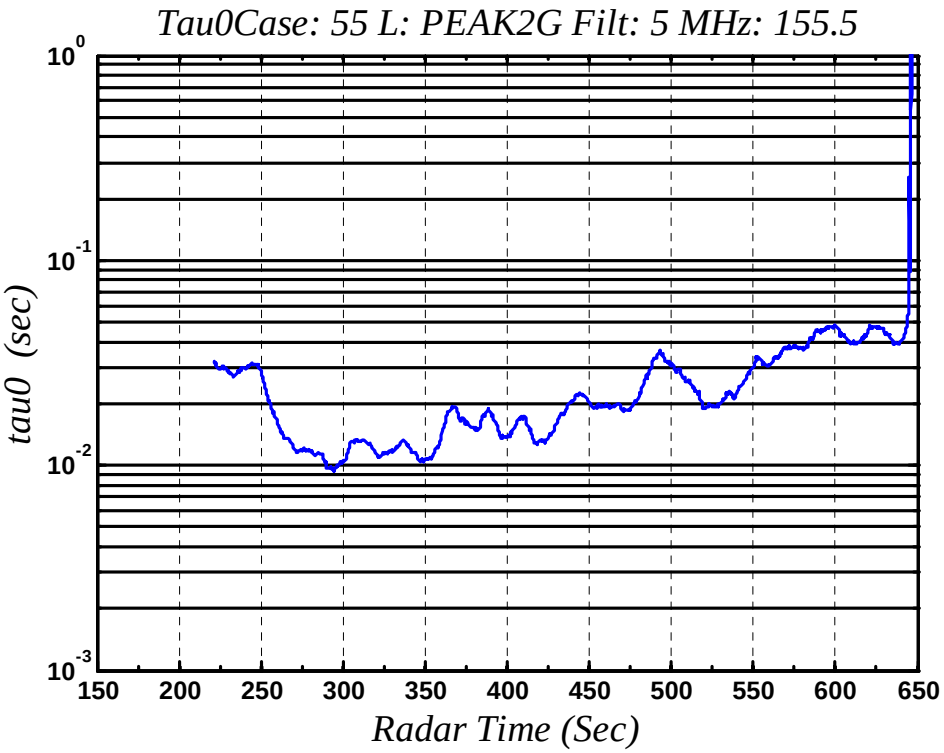

Figure D11. MPS calculation of decorrelation time at VHF.

The phase screen is scaled to the UHF frequency of 422 MHz and the propagation calculation proceeds exactly as described above. Figure D12 shows the power at UHF from the actual ALTAIR track and Figure D13 shows the power measured in the MPS simulation. A comparison of the two figures shows a basic similarity of results.

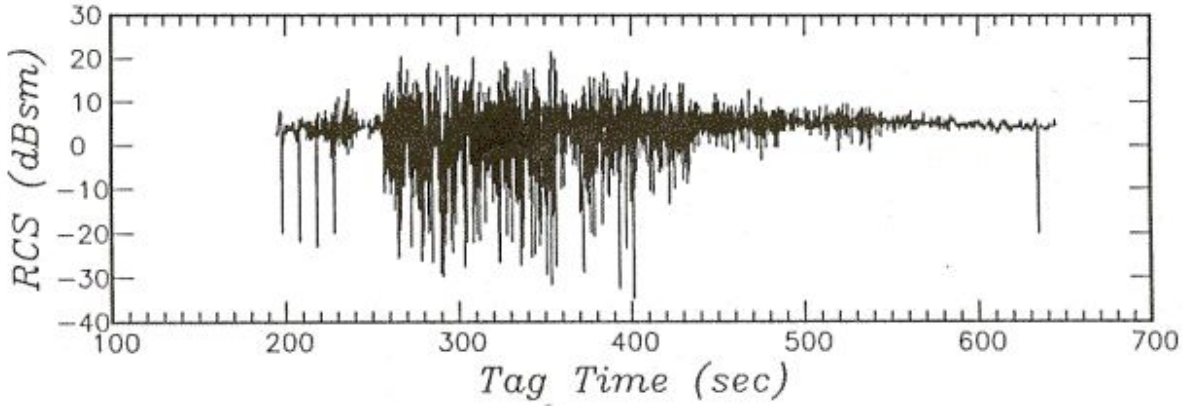

Figure D12. RCS at UHF measured during PEAK2G.

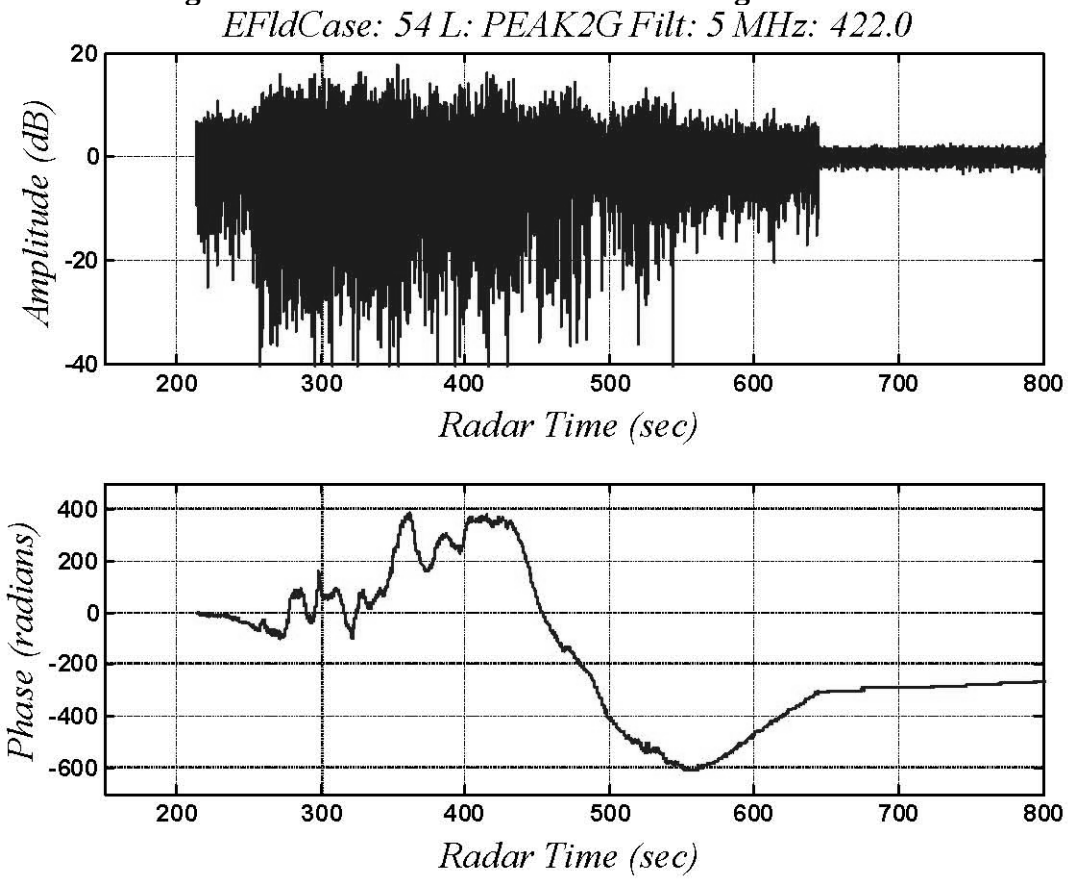

Figure D13. MPS calculation of UHF power and phase.

The overall results indicate that this type of analysis could be a useful approach in applying the ALTAIR data to other radar problems. However, the contribution to noise in the TEC measurements remains important and cannot be removed or filtered very well.

The effects of the noise could be overcome by another approach. ALTAIR also collects coherent amplitude and phase data. It is this data that was used to measure the decorrelation time shown above. Consider the phase history that consists of the measured phase as a function of target position during a satellite pass observed by the radar. There are two contributions to the

phase; one due to the target range and the second due to the ionization. The contribution due to range could be accurately estimated by using a trajectory fitting code to filter the range data and obtain the phase history due solely to range effects. Subtraction of the phase due to range from the measured phase would yield the phase due to ionization. This remainder could be used to generate accurate phase screen realizations of the ionosphere.

Similar techniques have been tried using differential GPS phase and in the analysis of Transit satellite data to measure TEC. The phase obtained in this fashion is a good measure of the ionospheric phase only if the scintillation index of the data is less than 0.75 and the sampling rate is sufficiently high [Knepp, 2004]. The sampling rate criteria appear to be met by the ALTAIR data.

D.2 Example and Validation of the MPS Code

In this section we describe the application of the Multiple Phase Screen (MPS) code to wide bandwidth calculations of propagating signals. This report presents results from a two-dimensional MPS calculation that computes numerical realizations or sample functions of the electric field after propagation through the ionosphere. The MPS code solves the parabolic wave equation and allows for direct computation of realizations of the received signal. The ionization is represented by a series of random phase screens that characterize the severity and spectrum of the electron density fluctuations. The user can also design their specific phase screen to represent a deterministic ionosphere. For wide bandwidth signals, the MPS code is exercised for many frequencies over the bandwidth of the propagating signal; Fourier transform techniques are used to obtain the propagating signal in the time domain.

The MPS simulation is quite general, and may be applied to problems involving numerous, separated, layers of ionization characterized by spatially varying electron density power spectra. MPS techniques can handle all levels of ionospheric disturbances from the least severe, where only small phase fluctuations occur, to the most severe case of frequency selective scintillation.

To validate the MPS simulation in this report, a number of calculations are repeated and the realizations are averaged to obtain the two-frequency, two-position mutual coherence function, which is the Fourier transform of the generalized power spectrum. The MPS results are compared with analytic results obtained using Nickisch's [1992] phase screen diffraction method (PDM).

Small Scale Ionization

Small-scale electron density irregularities can cause random variations of the amplitude, phase, angle-of-arrival, and time-of-arrival of a propagating signal. These variations are collectively referred to as scintillation. Their impact on a radar or communications system is a function of the in-situ ionospheric structure, the characteristics of the propagating signal, and the radar or communications system design. Since the index-of-refraction in a plasma is frequency-dependent, signals at lower transmission frequencies and wider bandwidth will generally experience more severe effects in comparison to signals with higher transmission frequencies.

The severity of the ionospheric structure depends on the local ionospheric weather conditions. In the equatorial region, strong scintillation can be important at VHF and UHF.

Equatorial scintillation begins in post-sunset and can last past local midnight. In the polar regions, scintillation can be important anytime of the day or night.

MPS Calculation

In this report, we apply a multiple phase screen (MPS) technique [Knepp, 1983] to calculate the effects of small scale ionization on a propagating wide bandwidth signal. The results from averaging many Monte Carlo realizations are compared to the Phase-Screen Diffraction Method (PDM) of Nickisch [1992]. This is part of an effort to validate the new Matlab implementation of the MPS code.

To obtain the solution for wide bandwidth propagation, the MPS code is applied to a spectrum of discrete frequencies over the bandwidth of the signal of interest. Note that the MPS realizations provide, in engineering terminology, the transfer function of the ionospheric propagation channel at a specific transmission frequency.

A useful time domain signal to use for illustrative purposes is the triangular function given by $p(t) = 1 - |\tau|/T_c$ for $-T_c < \tau < T_c$. The Fourier transform is $P(f) = T_c \sin^2(\pi f T_c)/(\pi f T_c)^2$. This function has nulls at frequencies that are multiples of $2/T_c$. To represent this function adequately, we use MPS frequencies ranging over $-2n/T_c \leq f \leq 2n/T_c$ where n is an optional integer, usually 1 or 2.

The phase screen diffraction method (PDM) [Nickisch, 1992] technique uses split-step Fourier transforms to solve the equation for the mutual coherence function under the strong scattering assumption. This assumption is not a limitation of the MPS calculation. The PDM calculation is three-dimensional, allows for phase screens that move in time with different velocities, is extremely fast with a minimum of computer resources required, and is an excellent choice for comparison to MPS calculations for strong scattering cases.

In the following, we apply the MPS propagation simulation to calculate some important features of signals that propagate through structured regions of the ionosphere. First consider the example of propagation through a single cloud of structured ionization. A similar example was considered in Knepp [1983]. Figure D14 shows an example realization of the single phase screen used to represent the ionosphere.

The phase screen representation here consists of a combination of two major features; a large Gaussian lens (to model the gross cloud) with a half-size of 5 km, a peak phase of 200 radians (which gives a gross propagation delay of $t_d = 200/2\pi f_c = 0.32$ microsec) and superimposed structured ionization. The large cloud is centered in the MPS calculation grid that consists of 524,288 points and whose length is 50 km. The structured portion of the phase of the cloud is represented with a power-law power spectral density (PSD) with q^{-3} slope (which corresponds to a q^{-4} for the 3D N_e spectrum), an outer scale of 390 meters, an inner scale of 10 meters, and a phase standard deviation of 4 radians. These values are not realistic for the natural ionosphere, but are chosen for the purpose of this example. A total of 64 spectral components (frequencies) are calculated over a total bandwidth of 20 MHz centered at a carrier frequency of $f_c = 100$ MHz. The propagation geometry consists of this single phase screen to represent the

ionization. The plane wave signal, $p(\tau)$, propagates a distance of 100 km to the receiver. The value of T_c is about 100 nsec.

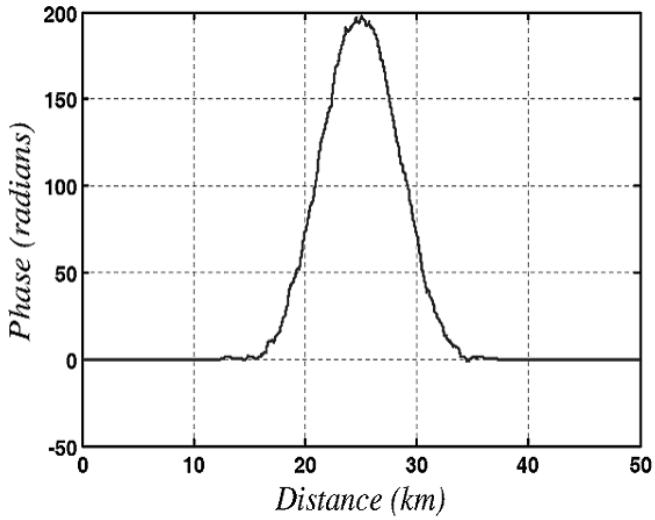

Figure D14. Phase screen representation of a cloud of ionization.

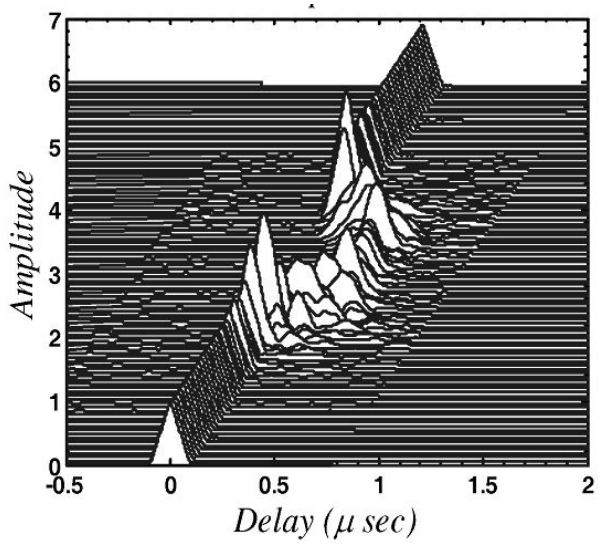

Figure D15. Time-domain signal after propagation 100 km past the cloud of ionization. Distance along the MPS grid increases from top to bottom.

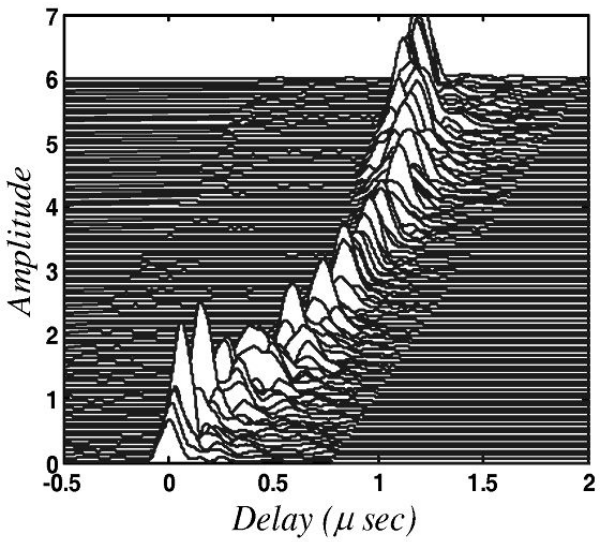

Figure D16. Close up of the central portion of the time-domain signal from 15 to 35 km along the MPS grid.

Figure D14 shows the phase of the single phase screen as a function of distance along the numerical MPS grid. Figure D15 shows a realization of the resulting time domain waveform as a function of distance along the MPS grid. In Figure D15, 100 plots of amplitude versus time are shown selected uniformly from the entire MPS grid of 2^{19} points. At the edges of the grid, at the top and bottom of the figure, the triangular pulses are not affected. The amplitude is near unity and the pulses are undistorted.

In the middle, the delay is greatest where the ionization structure is highest. At the edges of the smooth Gaussian, there is also some focusing where the signal levels are noticeably larger than unity. The smooth Gaussian ionization acts like a defocusing lens with a minimum near the center and peaks near the two edges (around 20 and 30 km). In the center of the grid there is significant time delay jitter which is caused by random angular scattering that is a function of the ionization and the transmission frequency. Figure D16 shows a close up of the interior portion of the MPS grid from 15 to 35 km.

The MPS propagation code contributes usefully to the analysis of the effects of the ionosphere on propagating wideband signals. For wideband signals, representation of the propagating signal consists of a complex valued function of both time and frequency. For a complete signal representation, one essentially needs, at a single instant, the amplitude and phase of the signal at each spectral component within the system bandwidth. Useful tools to help understand the impact of the ionosphere on wide bandwidth transmission systems are the impulse response function and its Fourier transform, the ionospheric transfer function. For wide bandwidth signals, the MPS code directly calculates realizations of the complex I&Q signal components across the signal spectrum. This calculation gives the ionospheric transfer function. This frequency-domain function is then multiplied by the transfer function of the receiver filters; then, the product is Fourier transformed to obtain the time domain signal that is input into the receiver of a radar or communications system.

Figure D17 shows an example of the transfer function and impulse response from this MPS calculation. Simultaneous portrayal of the magnitude of the transfer function and that of the impulse response function is very useful in understanding the effects of the ionosphere on the propagating wide band signal. One is able to associate effects in the time and frequency domains and to obtain an understanding of the spatial variation of the signal fluctuations. It is also possible to employ the MPS code to obtain other useful statistical averages of the propagation channel. Here, the MPS realizations are analyzed to calculate the mutual coherence function $\Gamma(x,f)$. This is accomplished by Fourier techniques involving multiple crosscorrelations of each frequency component in a multi-frequency realization with the realization at the carrier frequency. This result is then Fourier transformed to obtain the generalized power spectrum $S(q,\tau)$.

Figure D18 shows $S(q,\tau)$ for another example of an MPS calculation. For this calculation, the transmission frequency is 300 MHz and the MPS code propagates 128 frequency components over a total two-sided bandwidth of 40 MHz centered at a carrier frequency of 300 MHz. The propagation geometry consists of a thick scattering layer 420 km in thickness, which is modeled using 10 equally spaced phase screens. The MPS grid has a length of 100 km and consists of 2^{17} points. The signal then propagates an additional 420 km to the receiver plane. The total rms phase of the thick layer is 170 radians. A q^{-3} PSD is used to represent the phase fluctuation with an outer scale of 5 km and inner scale of 10 m. To obtain the averages, the code is exercised 50 times using a different random seed each time.

Figure D19 shows the phase screen diffraction method (PDM) [Nickisch, 1992] solution for the same propagation geometry as that used to create Figure D18. The two figures are quite similar and validate the MPS calculation.

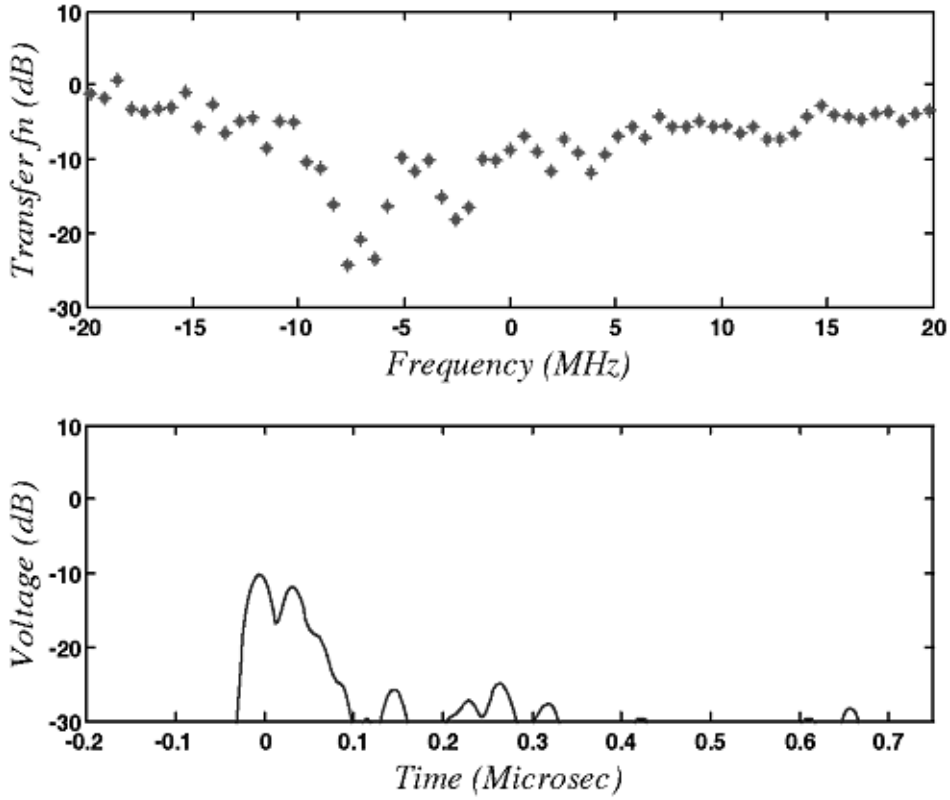

Figure D17. Example of the transfer function and impulse response function at a point along the MPS grid.

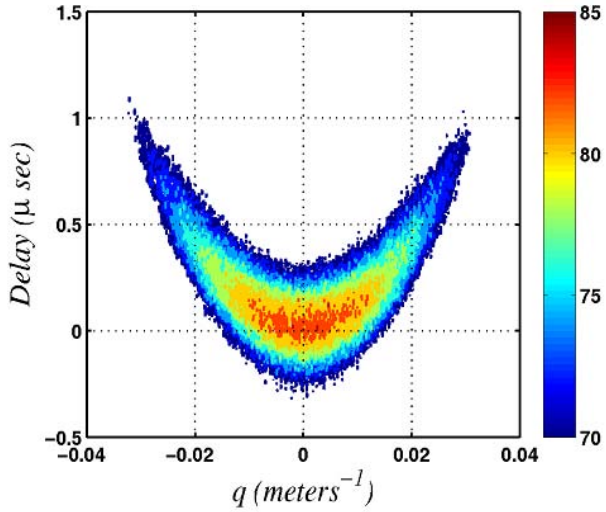

Figure D18. MPS measurement of the generalized power spectrum obtained as the average of 50 realizations.

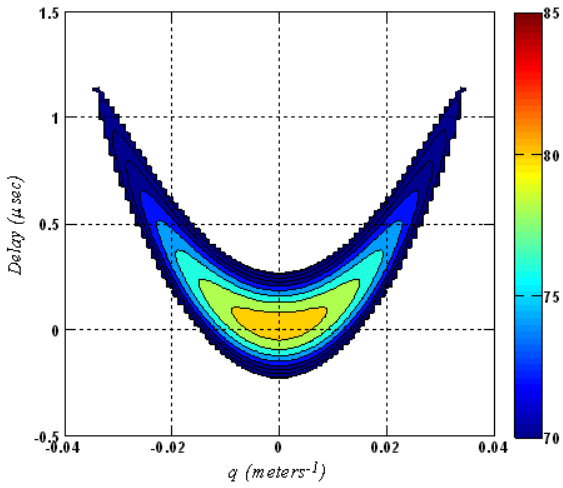

Figure D19. PDM calculation of the generalized power spectrum.

We have presented a comparison of the multiple phase screen results for the generalized power spectrum $S(q,\tau)$ with results from the phase screen diffraction method (PDM). The agreement is very good and we have validated the Matlab implementation of the MPS code. In addition, we have demonstrated a calculation that may be of specific interest to space based radar where both dispersion and diffraction is important.

Appendix E
Applications of GPS TEC Analysis Tools

Tools developed by NWRA under previous contract efforts and extended under the current contract were used to address various topics of interest of the USAF. In this Appendix we describe these efforts. In particular, we supplied ray-tracing expertise and code, and we provided analyses based on our ionospheric inversion algorithms (GPSII and CREDO, described below). The applications included AFRL testing of various ionospheric models, support for the MDA Early Launch Detection and Tracking program, demonstration of potential performance enhancements for a specific system of interest, analysis for a proposed Next Generation OTH radar system, and ionospheric calibration testing for Upgraded Early Warning Radar.

E1. Ionospheric modeling and Ray Tracing

NWRA delivered ray-tracing software and several post-processing routines to 2nd Lieutenant Shayne Aune of AFIT at Wright-Patterson AFB. Lt. Aune was preparing a master's thesis in which he was to demonstrate the effect of the ambient ionosphere upon radio wave propagation. We gave him an executable version of the Jones-Stephenson ray-tracing program that we have been using and refining for our own use for many years. We gave instructions in the use of this code, and acted as "tech support" for the questions that came up in using it.

Among the output generated by the ray-tracing program are binary files containing ray trajectories. We developed and provided Matlab scripts that could display these ray trajectories in an easily understood format. Figure E1 illustrates one example: a fan of rays has been shot at several different initial elevation angles and a single azimuth. We see that rays with low elevation angles are reflected back to ground, while higher-angle rays penetrate the ionosphere. The color contours show the electron density of the ambient ionosphere in the same plane as that of the ray fan.

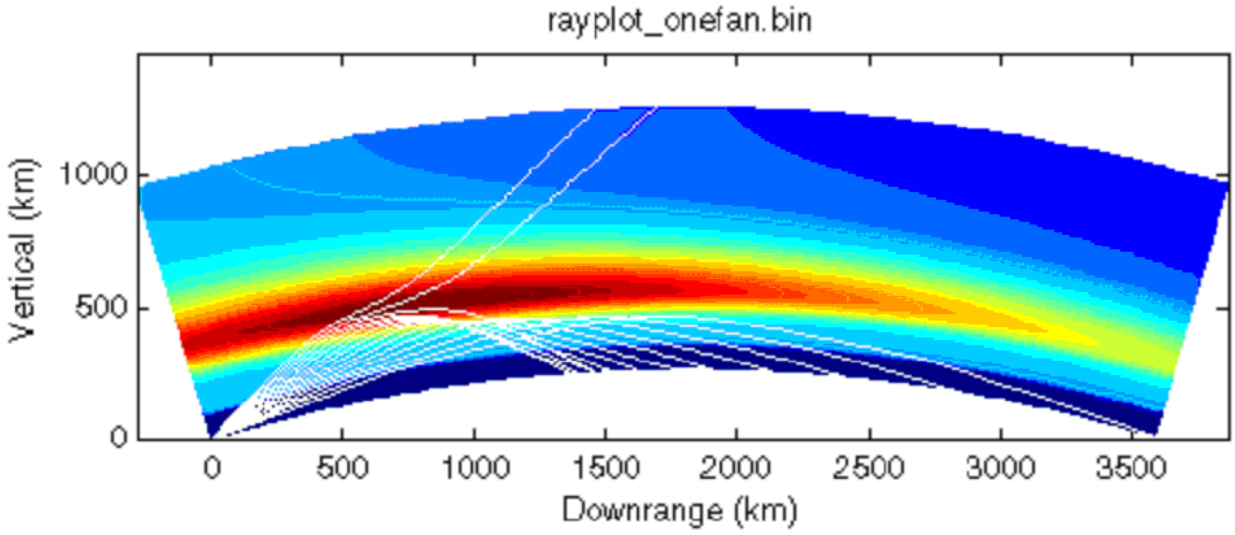

Figure E1. A fan of ray trajectories, with the ambient ionosphere shown.

We also provided a version of our executable program MakeIRItable. This program acts as a front end to the IRI-2001 model of the ionosphere. The user inputs his choice of a latitude and

longitude grid, sunspot number, and time and date, and the program creates a three-dimensional table of ionospheric electron densities. The table is in a format that our ray-tracing program can read. The color contours in the above figure show an example of MakeIRItable output.

Program MakeIRItable was delivered to AFRL/RVBXP. The intent was to produce tables of ionospheric density that could be used for ray-tracing studies to compare the results of the predicted IRI model ionospheres to other models, such as GAIM. AFRL has also been examining the IRI predictions for other purposes. They noticed a peculiarity in the dependence upon sunspot number which revealed a bug in our MakeIRItable front end. This bug was fixed, and the improved version of MakeIRItable was delivered to AFRL. Issues regarding having our ray tracing codes run successfully at AFRL were resolved.

NWRA provided AFRL with our GPS Ionospheric Inversion code, GPSII [*Fridman, et al.*, 2006; *Nickisch, et al.*, 2006]. AFRL, with our assistance, applied this code in a Direction Finding (DF) test. The GPSII algorithm was refined and tested, and a User's Manual was prepared to allow users at AFRL to run GPSII. We consolidated various subroutines that had appeared in slightly modified forms between our CREDO (referenced below) and GPSII codes; we made single versions that are compatible with both of these codes to maintain version control.

We extended the GPSII algorithm to incorporate relative TEC data from LEO satellites. Any number of LEO TEC receivers may now be processed simultaneously within GPSII together with data from GPS receivers and vertical sounders. The GPSII system automatically estimates data noise using sliding windows. Presently the system reads LEO satellite data from FORTRAN binary files. We created Matlab scripts for converting LEO satellite data from the NetCDF format to FORTRAN binary files. We tested the operation of the algorithm by simultaneously processing data from 19 GPS receivers and 2 LEO receivers. GPSII is still capable of working in real time on a 2GHz Pentium PC. We also incorporated a more general RINEX data reading capability and the option to use C1 data when P1 data is unavailable. The GPSII user's manual was updated to reflect the addition of the LEO capability.

We delivered the new version of GPSII with the capability of incorporating beacon data from LEO satellites. The GPSII User's Guide, updated for the LEO capability, was delivered as well. Assistance on GPSII operation was provided, on several occasions to Lt. Curtis Baragona. Assistance on both GPSII and RAYTRACE operation was provided to Lt. Joshua Warner. A significant upgrade to GPSII was also delivered. In this upgrade, certain memory-intensive matrix manipulations were performed in a new way that does not require the full expansion of sparse matrices. It makes much more efficient use of allocated memory than prior versions, resulting in a much smaller memory footprint and a reduced chance of crashing due to a fragmented memory heap. It is also significantly faster for large data sets that would have stressed the older version. For example, in a case that involved 26 RINEX receivers collecting data over 4 days, it took almost 22 hours to process with the old executable; the same case finished in 10 hours with the new executable.

NWRA also supported a MIMO experimental campaign conducted jointly by MIT Lincoln Laboratory and the Australian DSTO by providing predictions of propagation conditions for the planned campaign time and location. MIMO (Multiple Input Multiple Output), as applied to OTH radar, refers to the technique of transmitting orthogonal waveforms from the OTH transmitter elements, allowing transmit beams to be formed *after* signal reception. Experimental campaign planning required knowledge of HF skywave propagation mode elevation separations

to ensure that the antenna apertures were properly configured to be able to isolate the modes using MIMO. Using the FIRIC ionosphere model together with ray-tracing using our ray-homing algorithm, we provided the climatologically-predicted propagation mode details as a function of radar operating frequency. An example is shown in Figure E2..

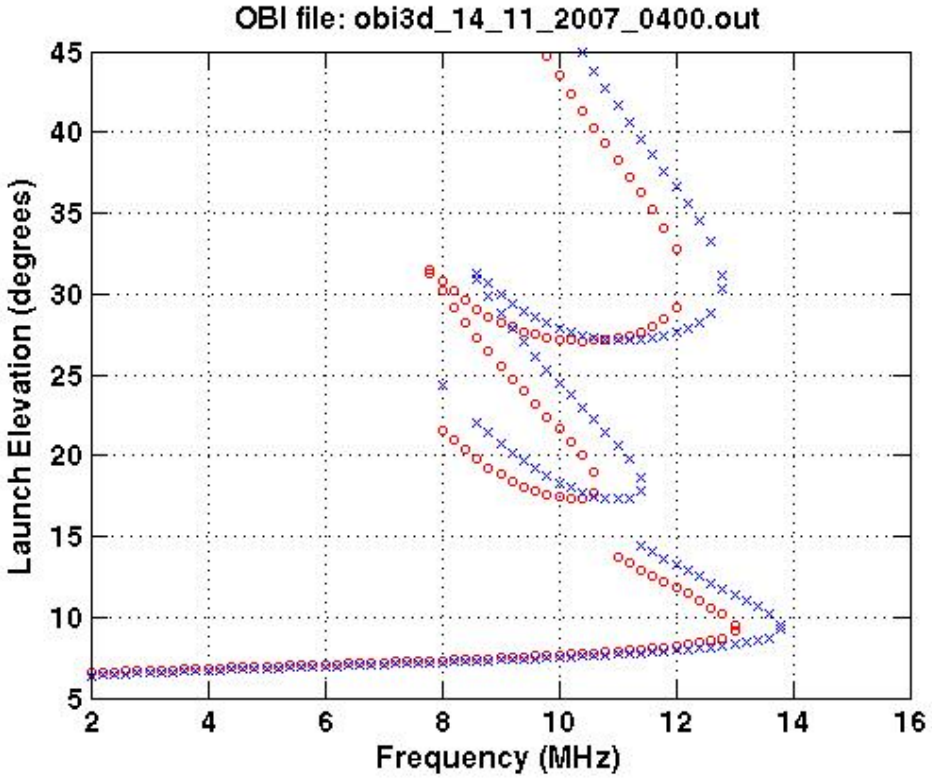

Figure E2. Predicted propagation mode elevations at the transmitter for the planned MIMO experimental link from JORN Laverton to Broome, Australia.

We also supported AFRL by providing examples of output from our ionospheric inversion code CREDO (referenced below) for briefings. Using ROTHR data for two 24-hour periods corresponding to low and high sunspot number, we created ionosphere models for each 24-hour period (with 12-min spacing) and made movies of critical plasma frequency over the geographical area of ROTHR coverage. An example of one of the movie frames is shown in Figure E3.

E2. Early Launch Detection and Tracking

Early Launch Detection and Tracking (ELDT) is a Missile Defense Agency program with the goal of providing a means to detect ballistic missiles immediately after launch. SkyLOS is a series of experiments supporting ELDT wherein forward-based receivers are used to detect HF reflections from missile launches that are illuminated by a remote transmitter.

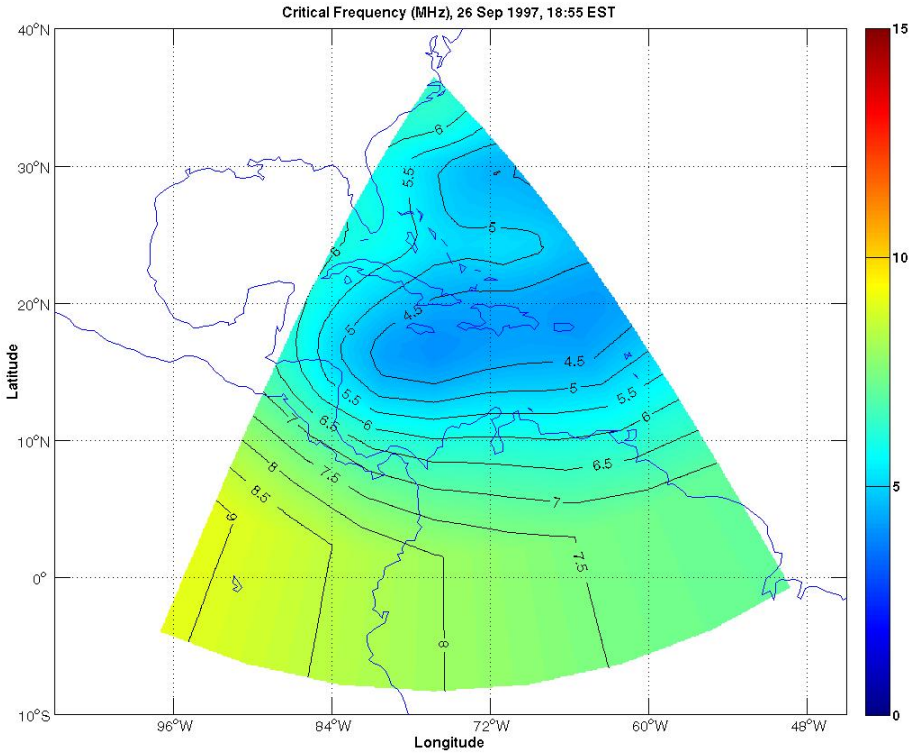

Figure E3. Contours of ionospheric critical frequency obtained by CREDO inversion of ROTHR Virginia sounding data.

Our approach was to use CREDO (Coordinate Registration Enhancement by Dynamic Optimization), a software package for the generation of ionosphere models from OTH radar soundings [*Fridman and Nickisch*, 2001]. With CREDO, we read in the VI and WSBI of each launch time, generated corresponding ionosphere models, and synthesized the OIs corresponding to the DSTO measurements. The synthetic OIs were overlain on the measured OIs to confirm the adequacy of the ionospheric solutions. A Matlab translation script was generated to convert the CREDO output model to the data format required by VTRPE, and the ionosphere models were delivered to Jim McGraw (Photon Research Associates; PRA) for VTRPE analysis. One of the two launch cases is shown in Figure E4, for 14 NOV 2005 at 2030 UT.

Figure E4 displays the WARF-measured VI. The synthetic VI generated from the CREDO solution ionosphere model is overlain, indicating that a good matching ionosphere model was obtained. Figure E5 displays the WARF Wide Sweep Backscatter Ionogram (WSBI). Overlain are the leading edges of major propagation modes from the fitted CREDO ionosphere model. Also overlain is the synthetic OI from the WARF transmit site to WSMR. Note that the endpoint of the WSBI is at the WARF receive site whereas the OI is transmitted from the WARF transmit site, which is why the nose of the OI does not exactly align with the WSBI leading edge.

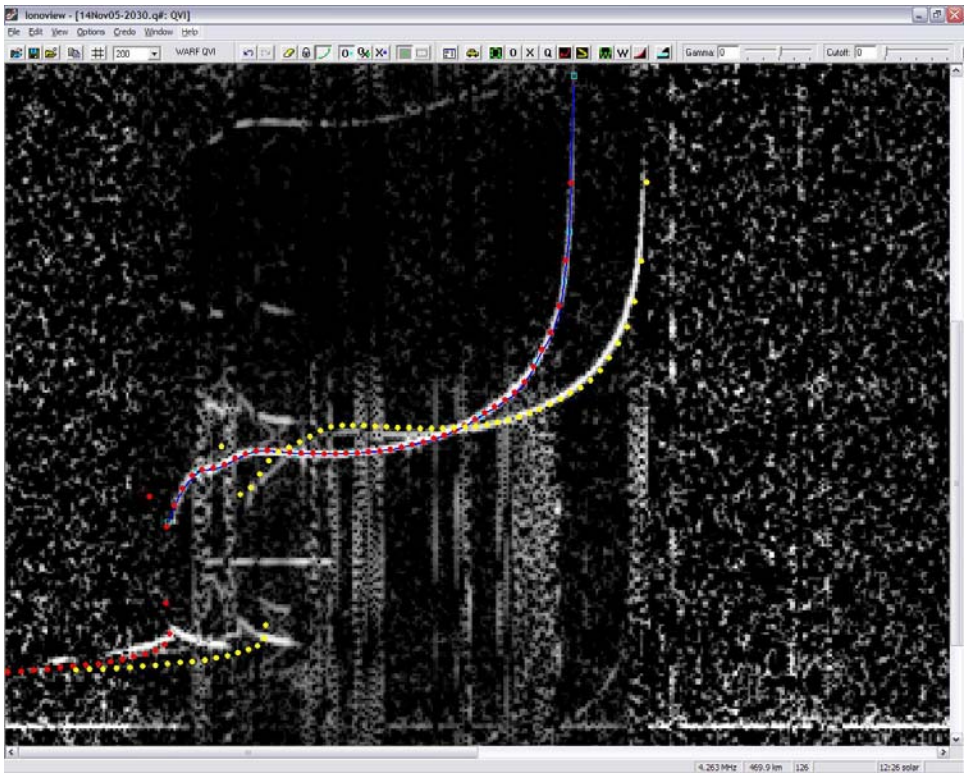

Figure E4. WARF VI with overlain CREDO solution.

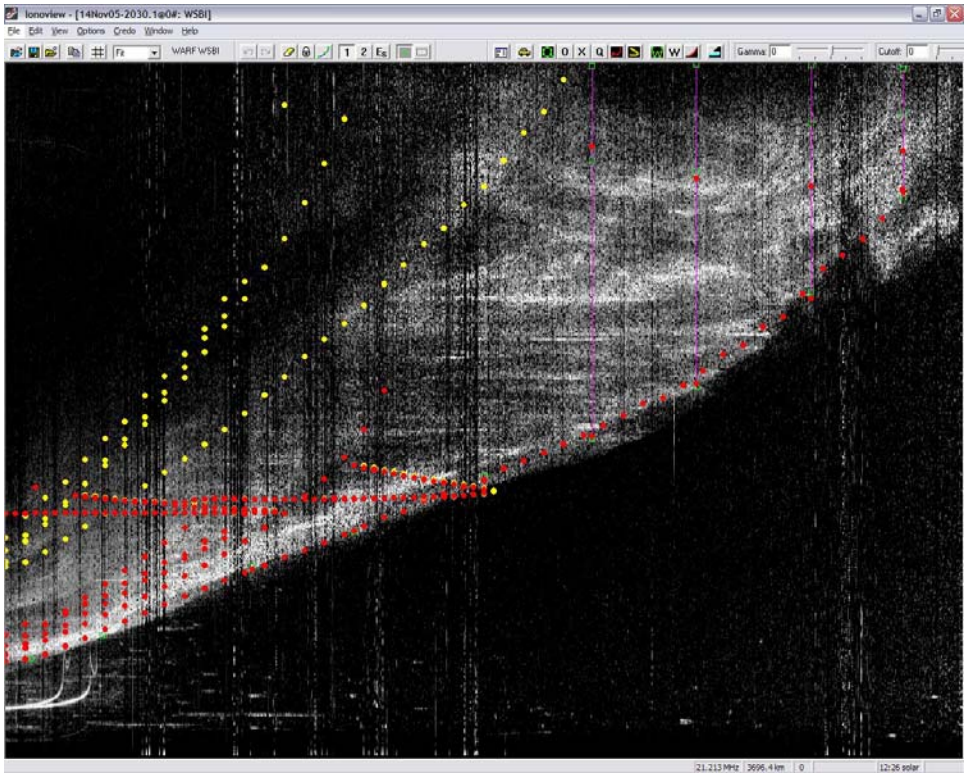

Figure E5. WARF WSBI with overlain CREDO propagation mode leading edges and synthetic OI.

Figure E6 shows the DSTO-measured OI with the synthetic CREDO-based OI overlain. Note the obvious Traveling Ionospheric Disturbance (TID) activity evident in the measurement, particularly as a ripple in the F2 high-ray trace and again at the OI F2 nose. These cannot be modeled in the CREDO ionosphere since the WSBI sounding bandwidth and antenna aperture size do not provide sufficient resolution. Aside from this, the match is quite good.

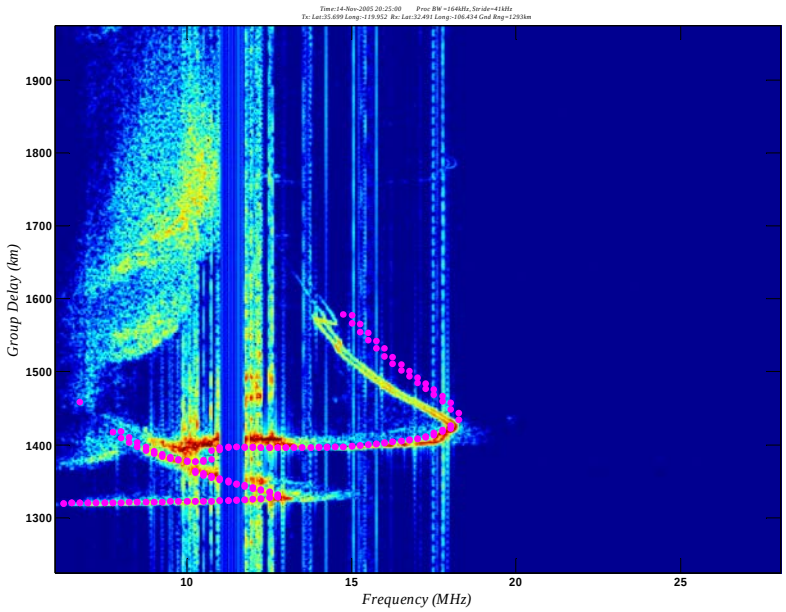

Figure E6. DSTO-measured OI and overlain CREDO synthetic OI.

Figure E7 shows the CREDO ionosphere model, plotted as plasma frequency in MHz. Figure E8 displays the signal strength (relative to free-space propagation) of the full wave VTRPE code using the CREDO ionosphere model. The transmit antenna elevation profile was assumed to be that of a vertical dipole. Near the bottom right hand corner of the plot is the trajectory of the missile launch. Ongoing analysis is being carried out at PRA to determine how well the CREDO ionosphere model predicts measured values of SkyLOS parameters like time-difference of arrival and frequency-difference of arrival.

The SkyLOS IV campaign was conducted in June 2006. Again, the WARF OTH radar transmitter in California was used to illuminate two missile launches from White Sands Missile Range (WSMR). For the previous SkyLOS III campaign discussed above, Vertical Incidence (VI) and Wide-Sweep Backscatter Ionograms (WSBIs) were collected by WARF to assist in modeling the ionosphere. These were unavailable for SkyLOS IV. However, Oblique Ionograms (OIs) were collected by the Australian DSTO on a path from the WARF transmit site to WSMR. We again were asked to provide ionospheric models based on these OIs that could be used in the full-wave propagation code VTRPE.

As with SkyLOS III, we used CREDO for generating the ionosphere models, but were hampered by the fact that CREDO takes as input VI and WSBI soundings, but not OIs, and VI and WSBIs from WARF were not available for SkyLOS IV (the WARF transmit site had been dismantled by this time). We resorted to converting the OIs to equivalent VIs using the well-known Equivalence theorems of ray tracing. These we supplemented with VIs at Pt. Arguello and Dyess AFB, which we obtained from DIDBase, an archive of vertical soundings maintained

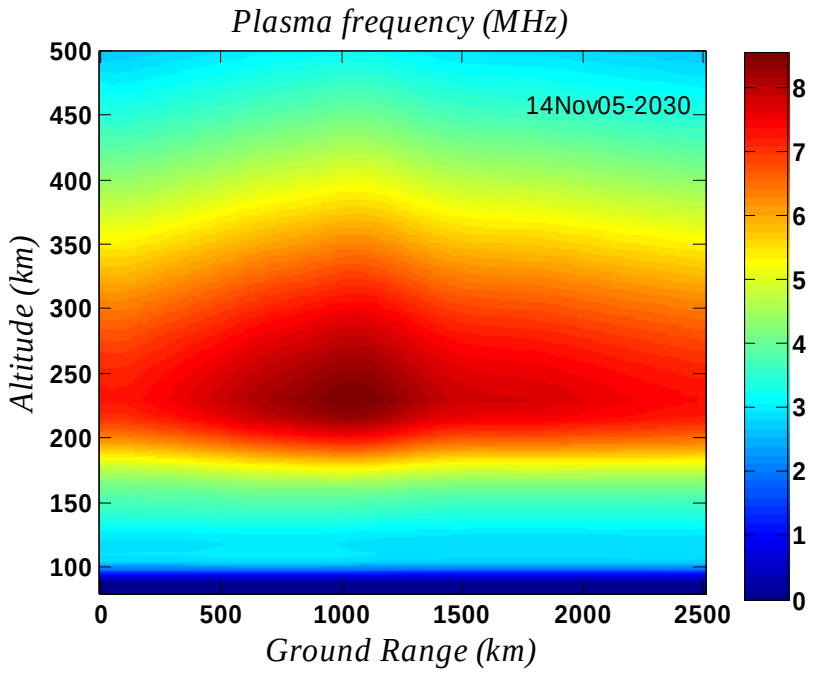

Figure E7. CREDO ionosphere model.

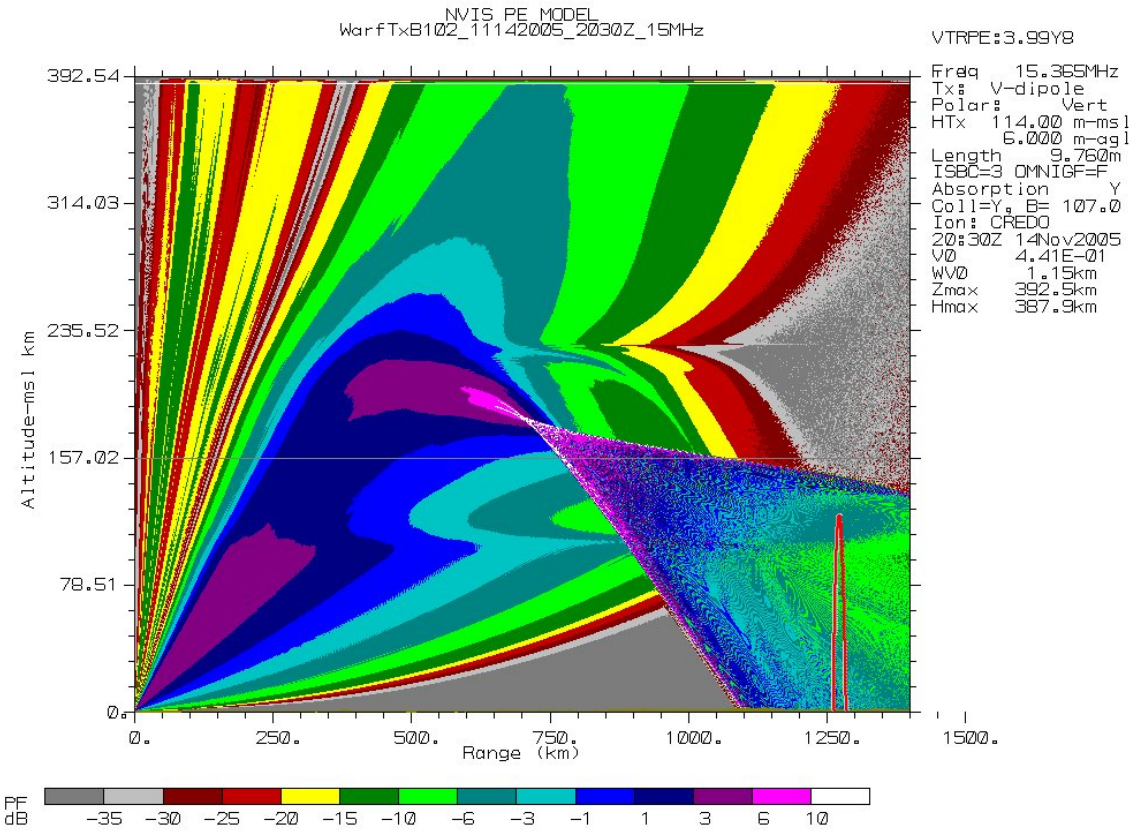

Figure E8. VTRPE full-wave signal strength plot in CREDO ionosphere.

by the University of Lowell Center for Atmospheric Research. We generated corresponding ionosphere models, and synthesized the OIs corresponding to the DSTO measurements. The synthetic OIs were overlaid on the measured OIs to confirm the adequacy of the ionospheric solutions. The CREDO output model was converted to the data format required by VTRPE, and the ionosphere models were delivered to Jim McGraw (Photon Research Associates; PRA) for VTRPE analysis. We also developed and supplied to PRA, a Hamiltonian magnetoionic 3D ray-tracing capability for their use in the SkyLOS data analysis. We assisted them in the proper use of the software.

NWRA assisted in planning for the SkyLOS V campaign. In SkyLOS V, the Relocatable Over-the-Horizon Radar (ROTHR) transmitter in Virginia was used to illuminate a launch of the space shuttle Endeavor from Cape Canaveral, FL. A fundamental issue with planning for SkyLOS V was determining what the area coverage would be from the Virginia ROTHR during the months May – September 2007. Our solution was to generate FIRIC model ionospheres for several dates within that period, using an assumed value for the sunspot number. Based upon the estimates available from NOAA, we estimated a most-likely sunspot number of about 12 for this time period. A few models were created with sunspot numbers 6 and 25, to test sensitivity to this parameter; we found that this variation had little effect upon the expected coverage area for any given frequency. We then ran our code "Raytrace" to follow the trajectories of rays launched into these ionosphere models. By launching fans of rays at numerous azimuths between the limits of ROTHR's coverage, we were able to estimate coverage at various frequencies by noting the landing locations of those rays that were reflected back to earth. We also developed a method to estimate the areal power density represented by these rays (i.e., received power per unit area at ground level) and display them upon a geographic map. An example is shown in Figure E9.

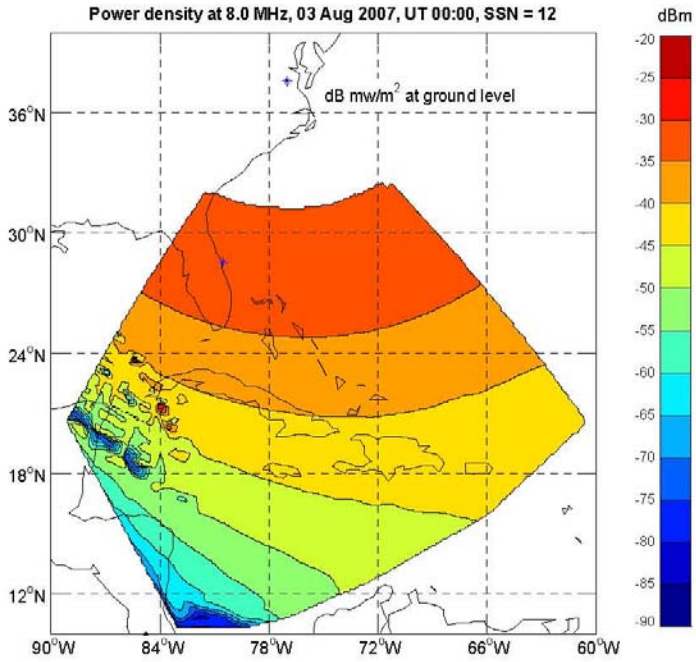

Figure E9. Sample coverage map generated for SkyLOS V.

Similar maps were generated for 24-hour time spans on several dates (August 3, June 28, and September 7). Frequencies were chosen to ensure that ample power reached the launch site at Kennedy Spaceflight Center (shown as a blue star on the figure above).

The possible effects and intensity of Sporadic-E (E_s) for the dates of interest were also estimated. A survey of literature and past ROTHR ionogram data allowed us to make probabilistic predictions of E_s intensity and frequency of occurrence; it appeared that E_s would likely be somewhat less of a problem than it was for the SkyLOS IV experiments. The effect of sporadic-E on individual measurements is of course unpredictable, but we can roughly estimate the effects of E_s upon coverage areas. We re-ran Raytrace with a very narrow, strong, E_s-like layer replacing the standard E layer. The almost mirror-like E_s reflection means that distances much closer to the antenna site can be reached at any given frequency. We then combined the power density for this simulation with the results of an E_s-free simulation to get a coverage map roughly representing 50% opacity of the layer. An example of the resulting coverage map is shown in Figure E10.

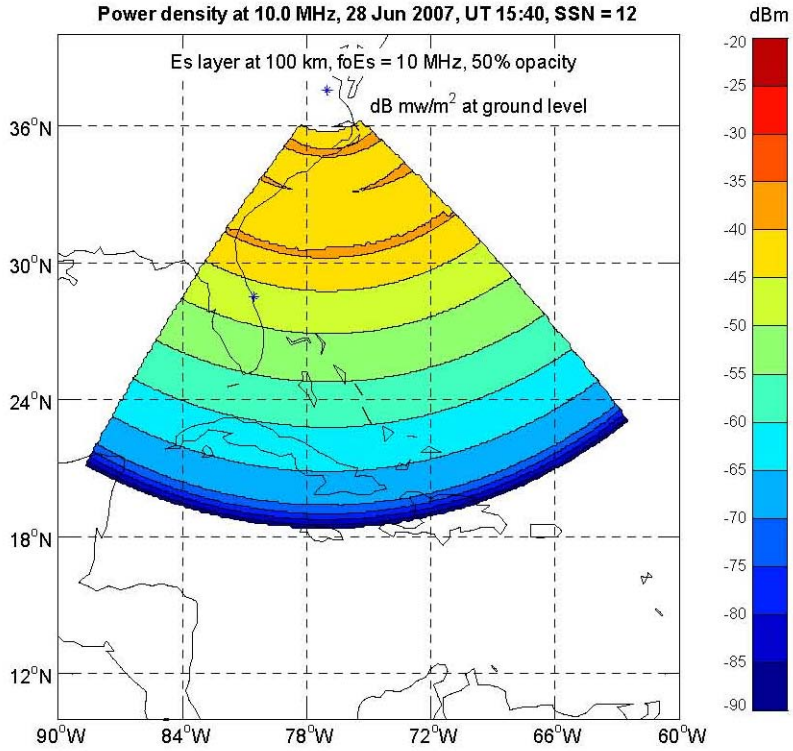

Figure E10. Coverage map combining power from E_s and normal propagation.

Using CREDO, we also developed a similar set of ionospheric HF propagation predictions for the SkyLOS V campaign using actual ROTHR-VA soundings for times of interest during the month preceding the actual launch on August 8, 2007. These were used by Photon Research Associates as the propagation environment for a VTRPE full wave analysis. Following the actual launch and data collect by the SkyLOS team, we received the ROTHR soundings and oblique ionograms collected by the Australian DSTO during the launch. These were used by us to develop models of the real ionosphere in effect during the SkyLOS V campaign, and were passed to PRA for VTRPE analysis and subsequent TDOA/FDOA measured trajectory analysis.

Consideration was given to the best means for automatic frequency management for SkyLOS. Thus far, the ionospheric modeling for SkyLOS has been performed using CREDO, which uses OTH radar soundings to determine the current ionospheric state, and which can be used to predict optimal frequencies for illumination of the launch site by a remote HF transmitter (as well as determining the HF propagation paths, a requirement for accurate FDOA geolocation). Ultimately, however, the SkyLOS concept must be viable for situations that are devoid of OTH radar support. We have suggested that the ionospheric modeling capability could be performed with GPSII, the NWRA GPS Ionospheric Inversion capability. GPSII uses GPS two-frequency beacon transmissions to model the current ionospheric state, optionally augmented with vertical sounding data. GPSII is a good candidate for SkyLOS because the SkyLOS transmitter and all receiver sites are already equipped with GPS receivers (for timing purposes).

E3. CREDO Application to a Specific System

AFRL provided NWRA with sounding data from a specific system-of-interest. We developed the capability to read and display these data in Ionoview, the graphical user interface for our CREDO capability (Coordinate Registration Enhancement by Dynamic Optimization). We made modifications to our CREDO code in order to be able to develop three-dimensional ionosphere models from these sounding data. These were used to perform a demonstration of CREDO's capability of providing high-fidelity coordinate registration for this system. All of the ionograms that we received were examined. A time sequence of ionosphere models was made for the relevant geographic region covering the three-hour period for which ionogram data were available.

CREDO was extended to allow the generation of three-dimensional ionosphere models, even when no Backscatter Ionogram (BI) data are available, or when only single sector BIs are available (in addition to vertical soundings). This makes CREDO useful in regions where vertical sounding data are available, but where there may be no OTH radar to provide backscatter ionograms, or for special systems with only a single BI sector. Previously, CREDO worked with single-sector WARF radar soundings, but provided only a two-dimensional (range-altitude) ionosphere model in the direction of the single-sector BI. The extended version of CREDO uses the underlying FIRIC ionosphere model to initiate the ionosphere model beyond the single sector, expanding to nine sectors covering 90 degrees of azimuth. That initial model is then adjusted to derive an ionosphere model that matches the single-sector BI data and available vertical sounding data.

We applied this capability to data from this system. We also developed new code for Coordinate Registration (CR) of targets using CREDO-generated ionosphere models. The CR routine computes fans of rays from the transmitter and receiver locations, allowing the construction of all possible two-way propagation modes to given target radar slant coordinates (delay and azimuth-of-arrival at the receiver). A mode association algorithm is applied that seeks to minimize the variance of inferred target ground coordinates as weighted by computed mode signal strength. The procedure was applied to test data with GPS truth. The CREDO improvement over the currently implemented method was documented and delivered to the customer.

E4. Next Generation OTH Radar Analysis

NORAD/NORTHCOM is promoting the development of a next-generation OTH radar, dubbed NexGen. The initial phase of this endeavor is to develop a NexGen Roadmap that defines the requirements for such a system. We were asked to support the definition of the Coordinate Registration function of the NexGen system.

A new capability of the NexGen system will be backscatter soundings received on a two-dimensional aperture, allowing some measure of the received elevation angles of the backscattered propagation modes. We developed a simulation capability for generating such backscatter ionograms. We resurrected the Clutter Effects Model (CLEM) code [*Lauer, et al.*, 1998], which models OTH radar clutter, including Spread Doppler Clutter (SDC) caused by naturally occurring small-scale ionization structure. Ultimately, we hope to use the algorithms in CLEM as the basis for a detailed NexGen simulator. For the current effort, however, we concentrated on the simulation of Elevation Backscatter Ionograms (EBIs). Backscatter Ionograms (BIs) of current OTH radars can provide only frequency-delay information about the propagation mode environment. Unfolding this information in receive elevation will provide a considerable additional constraint on inverse-processing solutions for the current ionosphere model, which should significantly improve Coordinate Registration accuracy. Using CLEM, we were able to synthesize an EBI to illustrate this extra information. Figure E11 displays a synthetic BI created using CLEM, but displayed in the traditional frequency-delay format. In Figure E12, the view is rotated to expose the receive elevation axis. Note that E-mode returns are separated from the F-mode returns in this view and are easily distinguished.

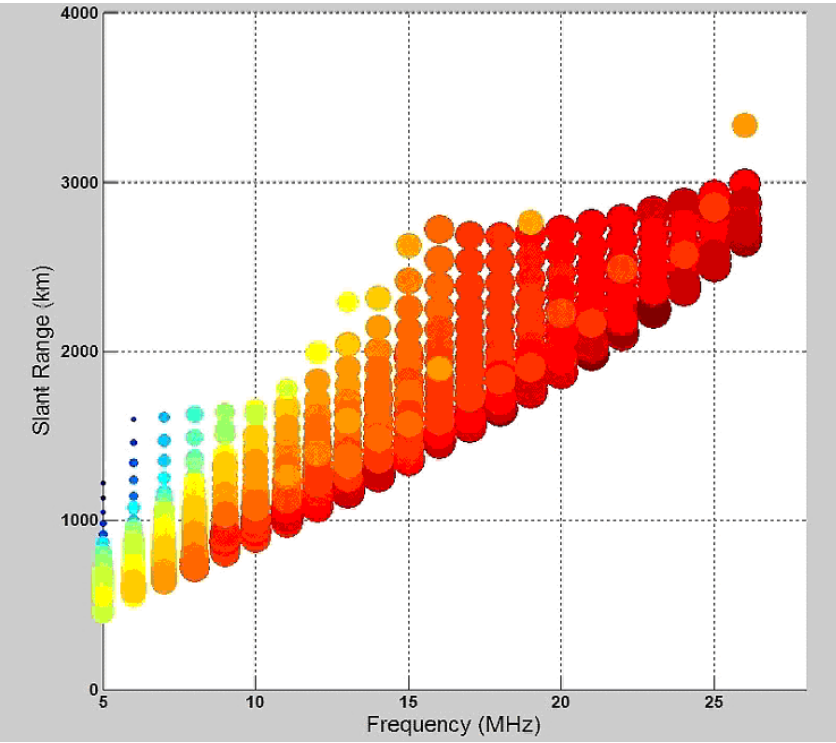

Figure E11. Synthetic Backscatter Ionogram in traditional frequency-delay (slant range) format.

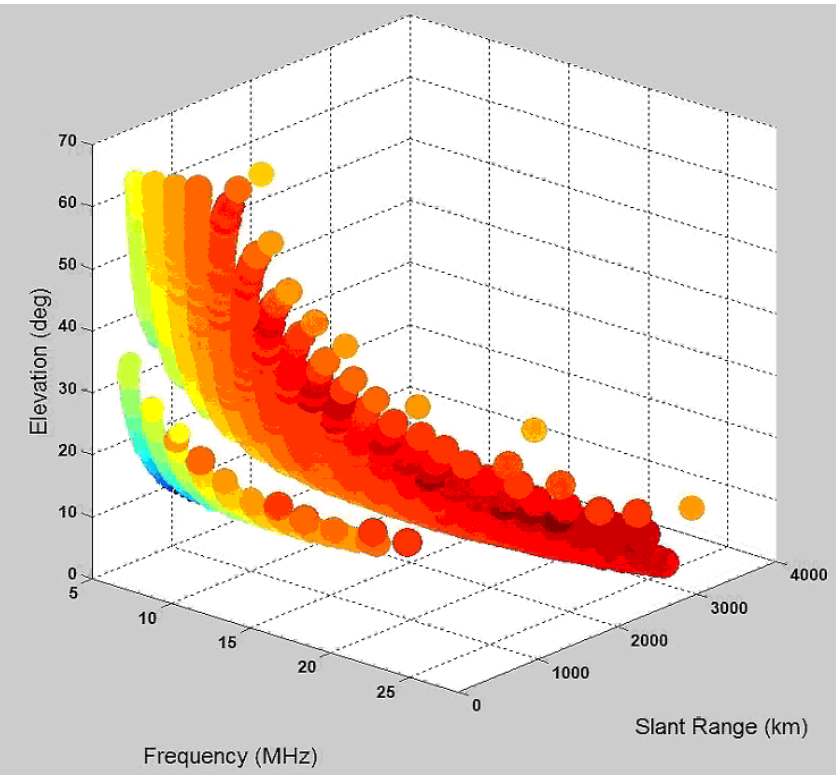

Figure E12. Synthetic Elevation Backscatter Ionogram.

Appendix F
Example Output From the SCORE Implementation

This appendix provides examples of graphical displays that were developed under this contract effort to provide tools for better assessment of the accuracy of GPS observations derived from measurements of ionospheric group-delay and phase-advance. As described in Section 3.2.1. of this report, these tools were developed to provide better assessment of the performance of the SCORE system and, once it is ready, for the SCORPION system.

Three different types of plots are generated by the standard GPS TEC processing:

a. Latitude-slice plots of TEC as a function of time and IPP latitude as a function of time. Typically, more than one latitude-slice plot is generated per station-day. Figure F1 shows an example of an "all" latitude slice, and Figure F2 is an example of a "center" latitude slice showing the inclusion of the average TEC and +/- one standard deviation from the average (heavy and light black curves, respectively).

b. Bias comparison plots, plotting the biases derived in the SCORE processing against the biases from the AIUB files. Figure F3 is an example of this plot.

c. By-PRN TEC average and variation plots. This is a plot, by satellite, of the average difference and standard deviation between the TEC for that satellite and the mean TEC calculated from the "center" latitude slice. Figure F4 is an example of this plot. The two horizontal dashed lines are the average standard deviation for the entire data set, and the vertical bars at the bottom indicate the relative number of points by PRN.

We were able to use TEC observations from the Jason-1 satellite-based altimeter for comparisons with the GPS TEC data as part of the quality control and uncertainty assessment processes. Two different types of plots are generated in the GPS-Jason comparison:

a. A "composite" plot showing a variety of parameters from the comparison. Figure F5 shows an example of this (in geographic coordinates). The red triangles are the sub-satellite latitude and longitude for the Jason points used in the comparison, the blue circles are the (smoothed and resampled) Jason-1 TEC values as a function of latitude, the black bars indicate the weighted GPS average and standard deviation TEC as a function of latitude, and the green diamonds are the weighted average difference between the Jason-1 and GPS TEC. The bias file used to create the GPS TEC data, and the settings for the parameters used to control the comparison process are given at the bottom-left of the plot.

b. A "multiple" plot showing four different views of the data included in the composite plot. There are two versions of this, one which has a plot of the azimuth and elevation of both the GPS and Jason TEC points and one which has a plot of the latitude and longitude of these points. Figure F6 is an example of the first type, and Figure F7 is an example of the second type. These plots show individual data points, not averages. In each plot, the Jason data are shown as black triangles and the GPS data are shown as colored circles, with the color indicating which satellite the data came from. The other three plots on each figure are, from bottom left clockwise, local time as a function of latitude, TEC as a function of latitude, and TEC as a function of local time.

We also developed a set of after-the-fact plots providing various views of the behavior of the satellite and receiver biases as derived from both the raw GPS data during the SCORE analysis and by comparison with biases obtained from the AIUB.

a. A pair of plots for a specific station showing the variation with time of (1) the nominal receiver bias derived from fitting the SCORE-produced biases with AIUB biases, and (2) the slope of the linear fit derived from comparing the SCORE-produced biases with AIUB biases (the slope of the linear fit shown in Figure F3). Figure F8 is an example of this plot for the station at Neah Bay, WA. Note that the receiver bias plotted is the difference between each individual day's estimated receiver bias and the mean bias for the full set shown in the plot. Sudden changes in the character of these plots, such as the jump in the receiver bias on day 94, can be used to watch for the need to use a new set of biases.

b. A plot for a specific station of the combined satellite+receiver bias for each PRN as a function of time. Figure F9 is an example of this plot for Neah Bay, WA, for the same time period covered by the data in Figure F8. As in the receiver-bias plot in Figure F8, shown plotted is the difference between the combined bias for each day and the mean bias for the entire period for that PRN. A sudden change in all PRNs, such as occurs at day 94, can indicate a change in the receiver bias, while a change in only one PRN may indicate either a change in that satellite's bias or a change in the local propagation environment which results in a change in the multipath characteristics for that PRN.

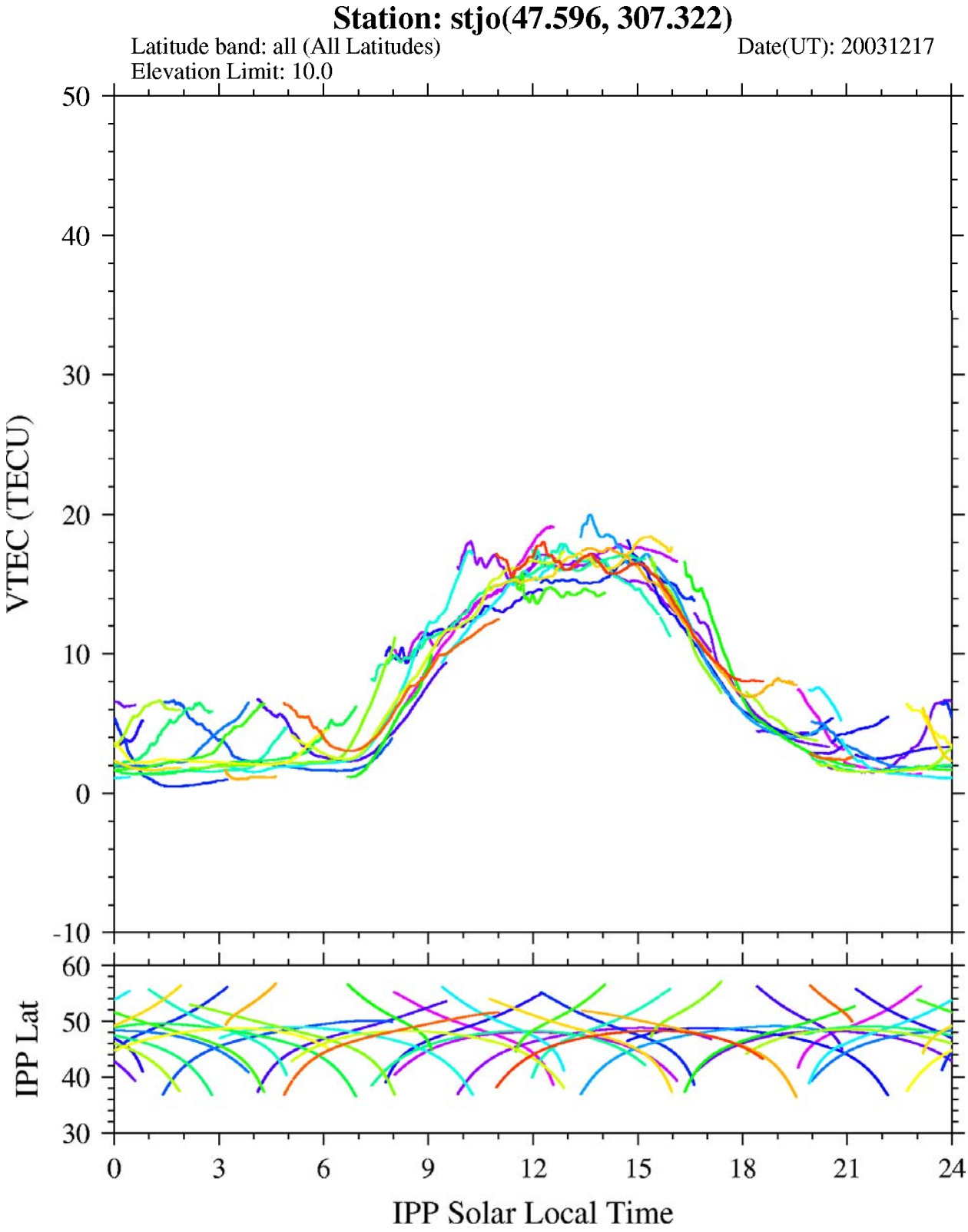

Figure F1. Sample SCORE "all" latitude slice plot.

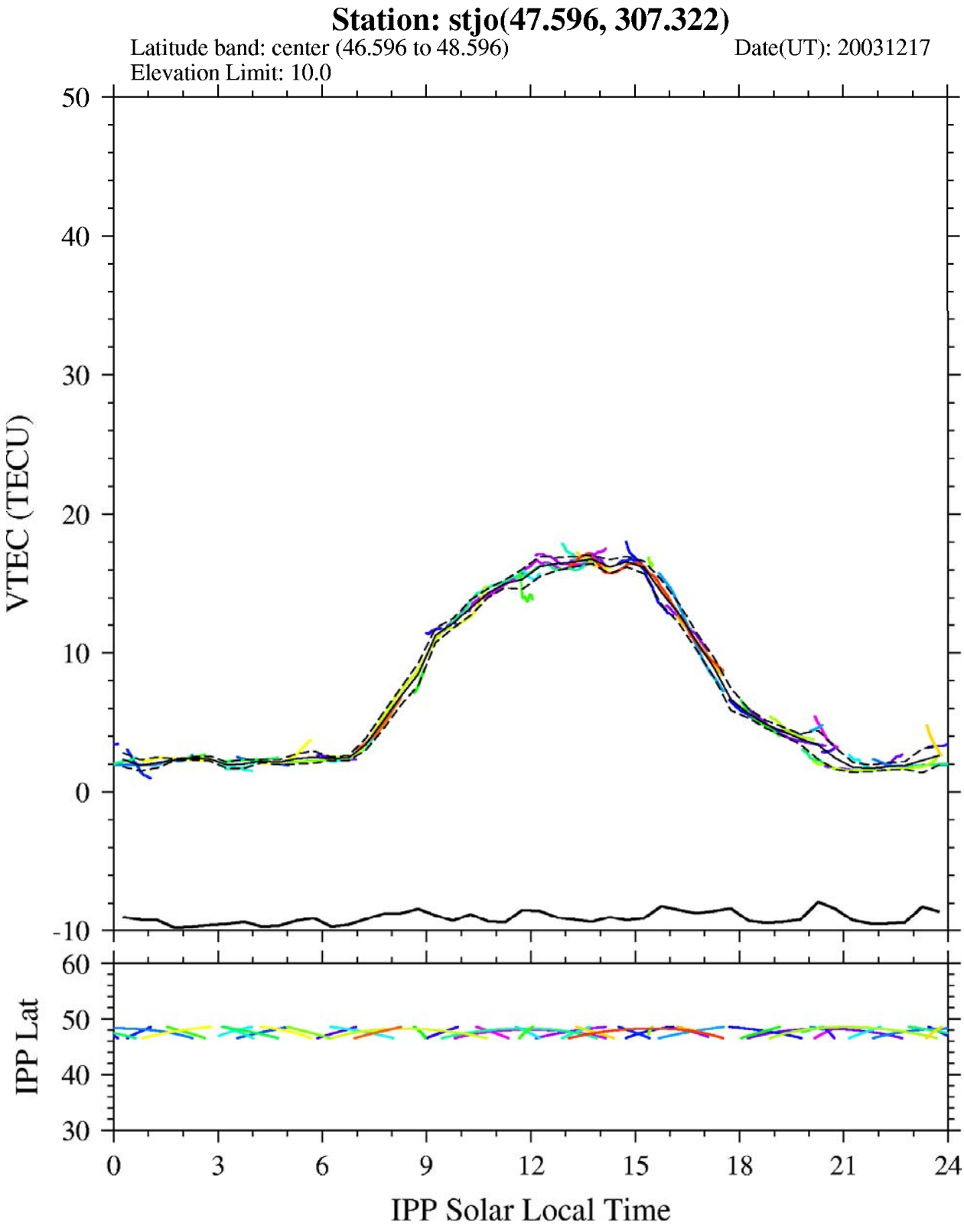

Figure F2. Sample SCORE "center" latitude slice plot.

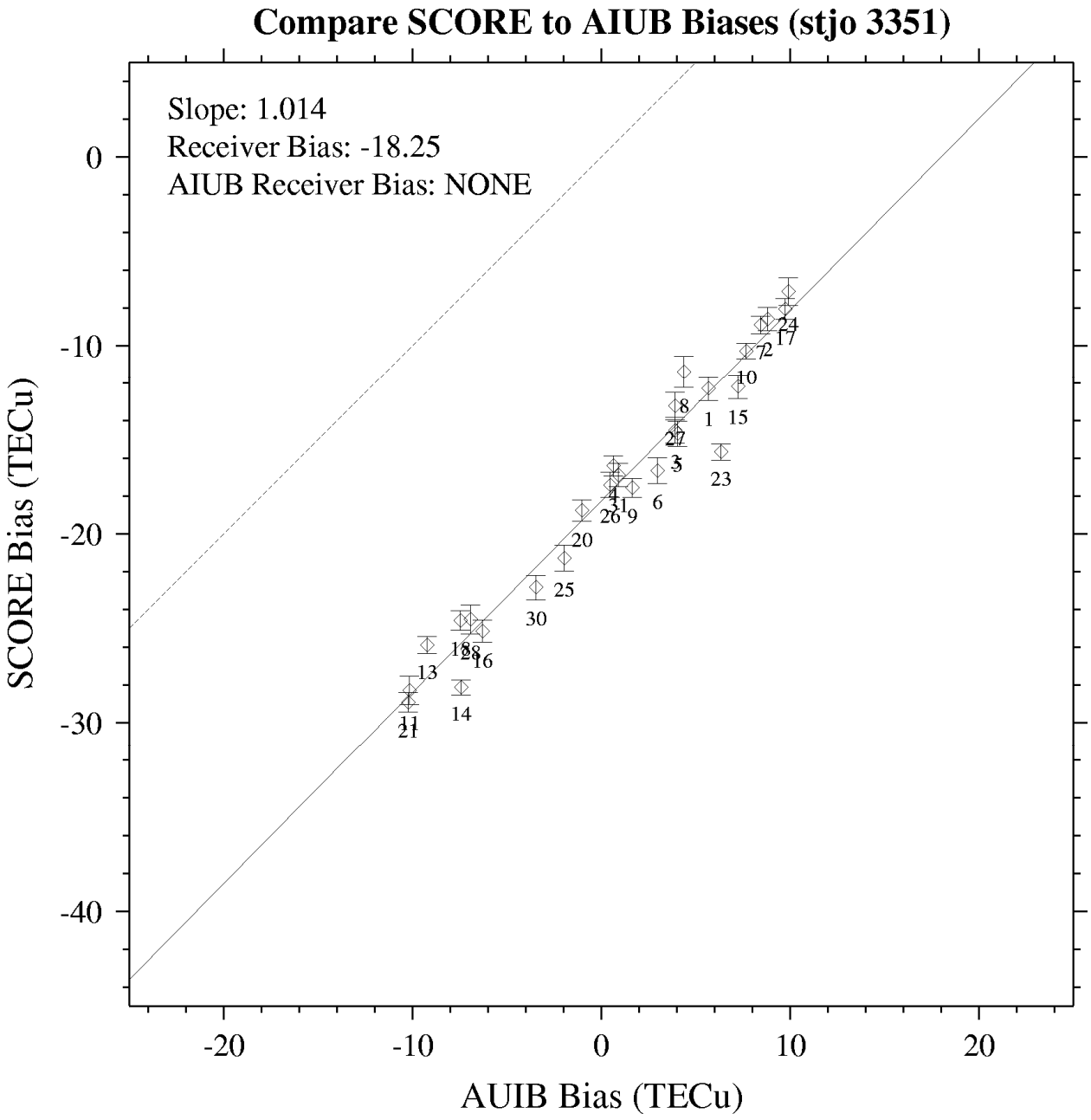

Figure F3. Sample SCORE AIUB bias comparison plot.

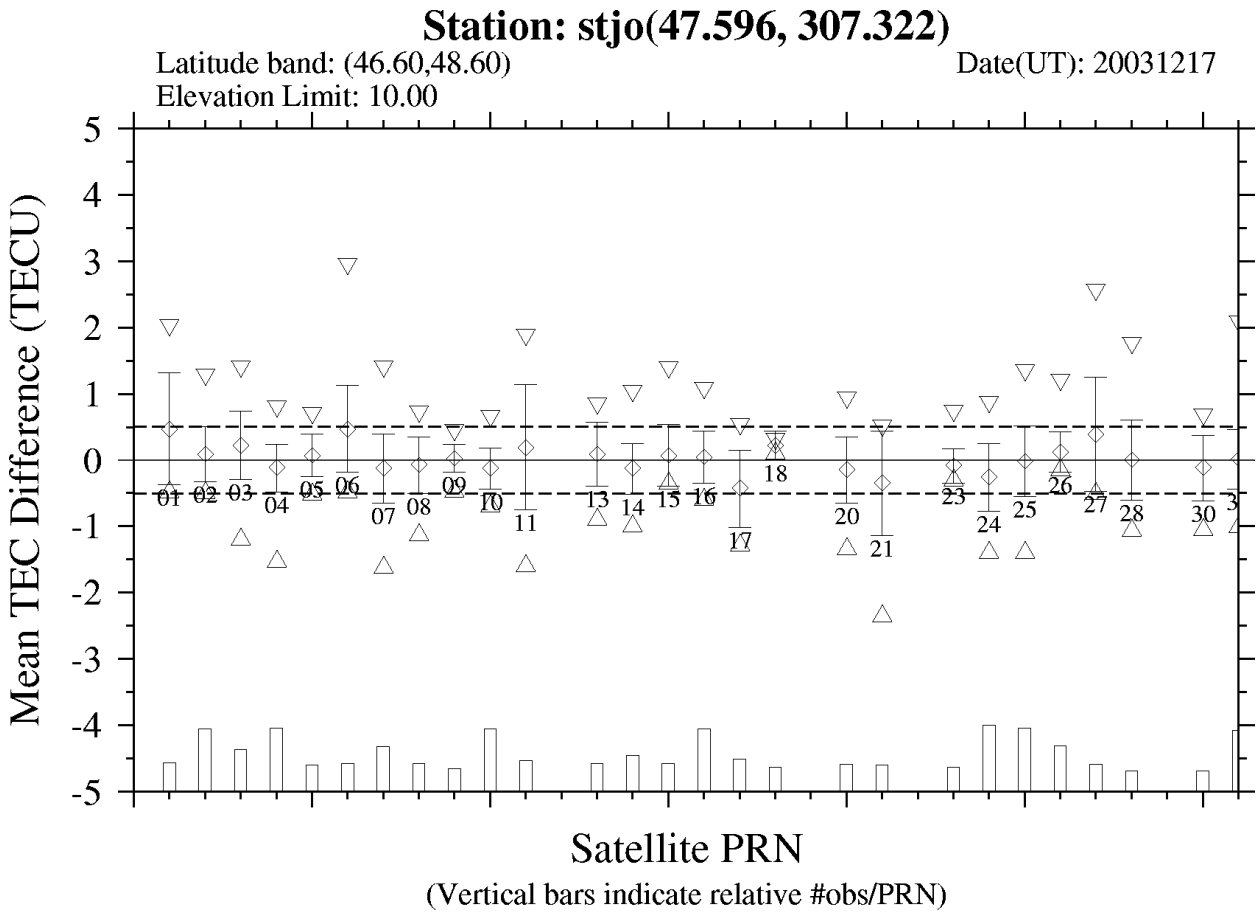

Figure F4. Sample SCORE by-PRN quality-control plot.

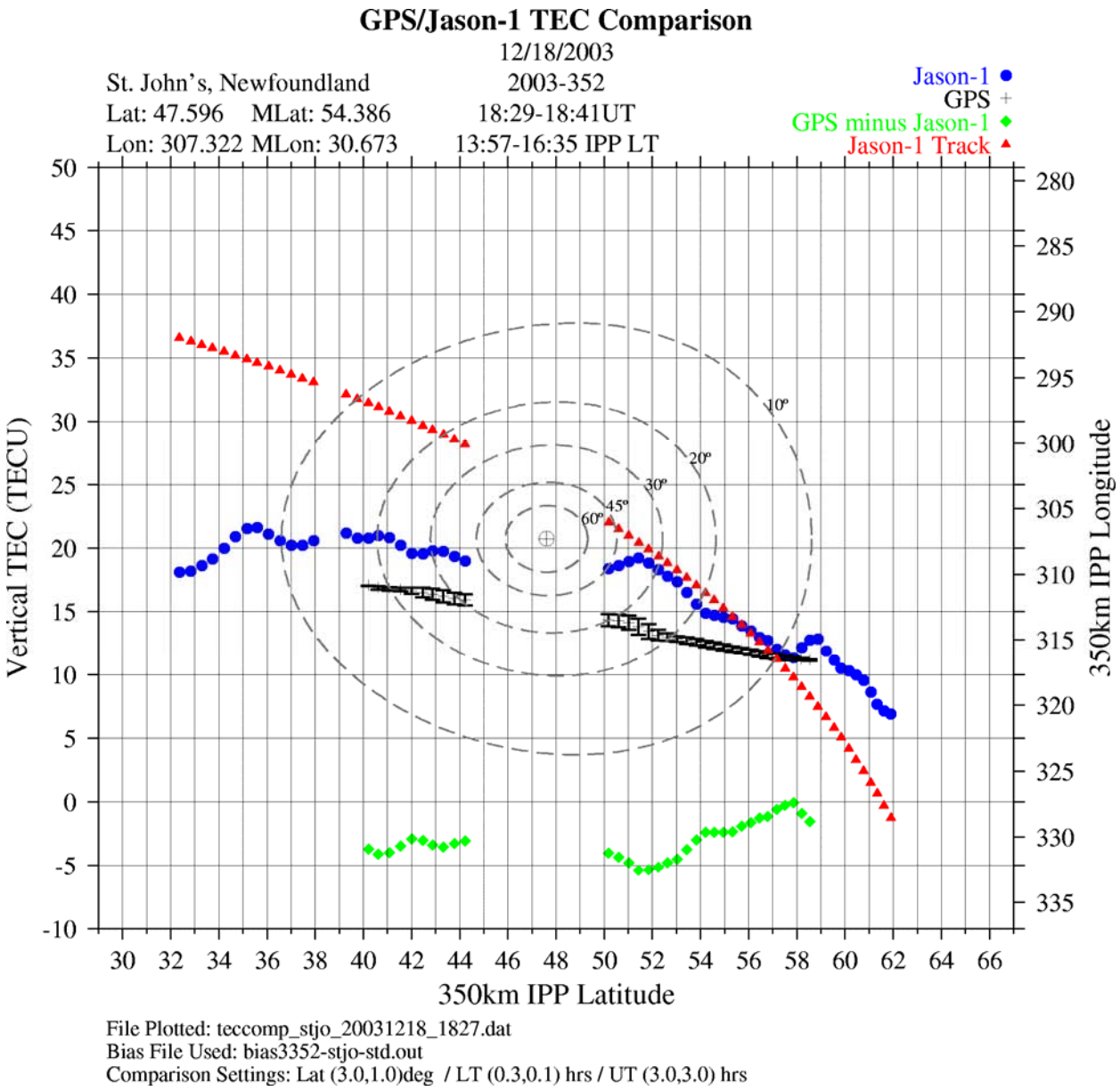

Figure F5. Example of the GPS-Jason comparison composite plot.

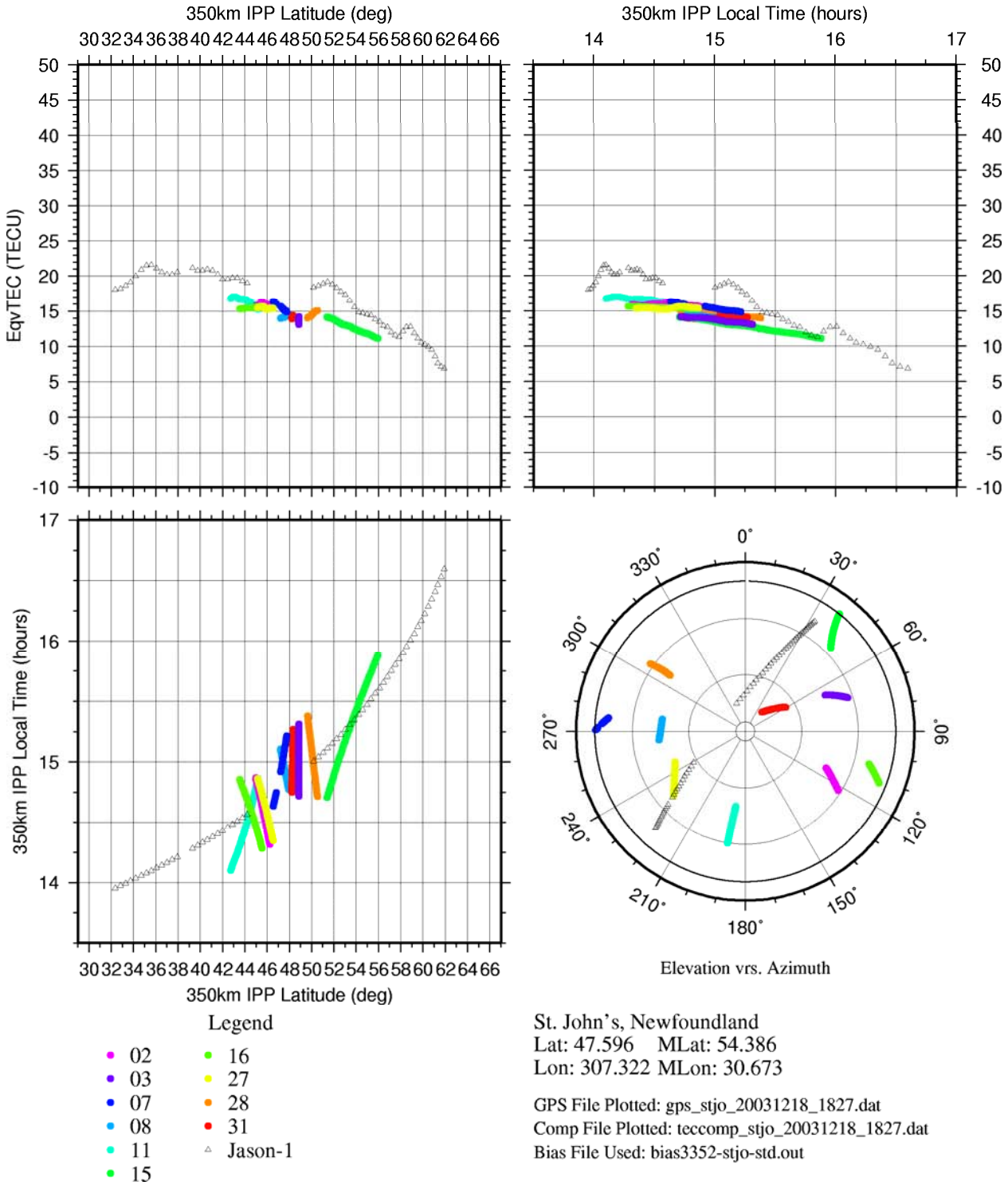

Figure F6. Example of the GPS-Jason multiple plot (with elevation-by azimuth option).

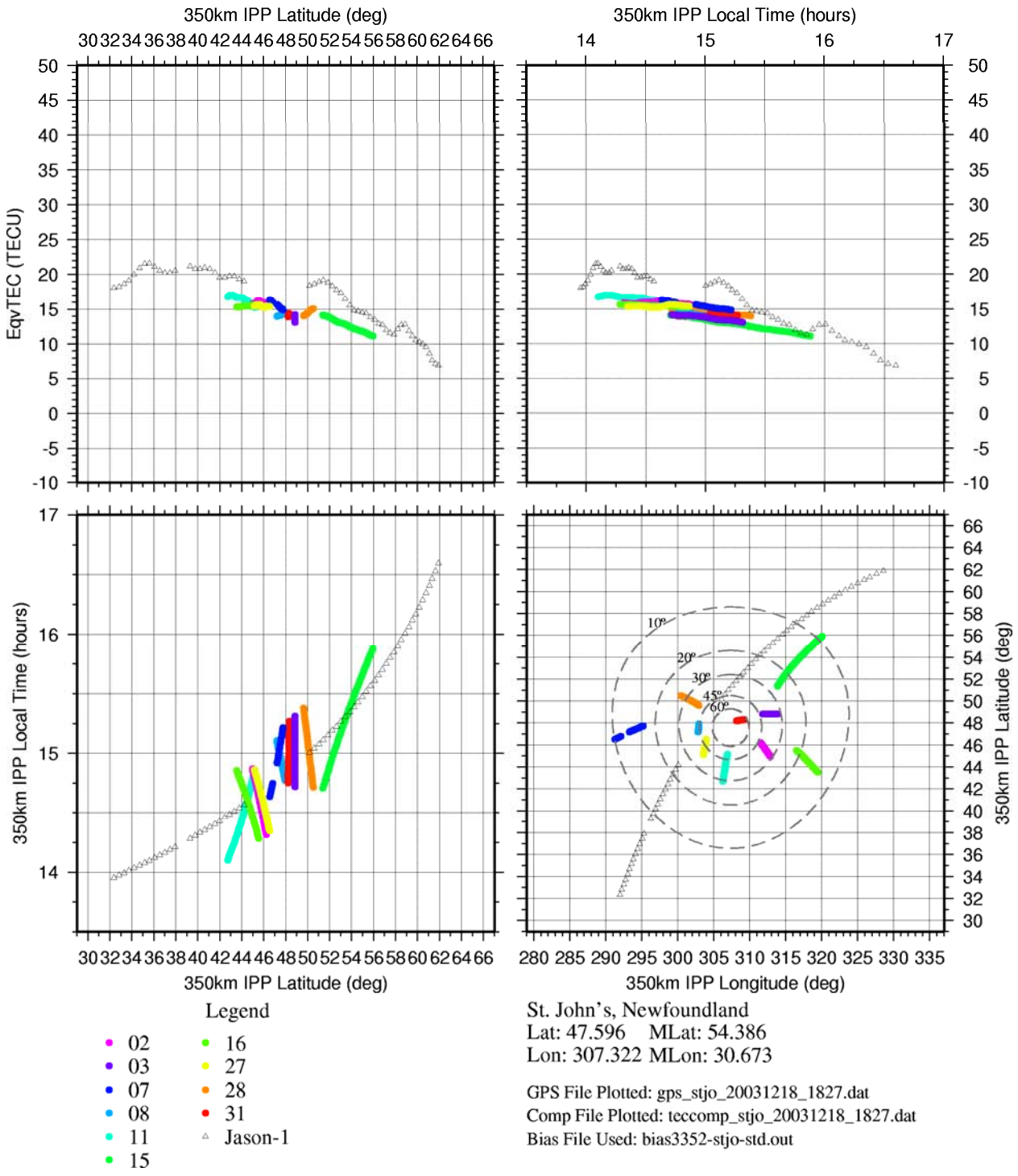

Figure F7. Example of the GPS-Jason multiple plot (with latitude-by-longitude option).

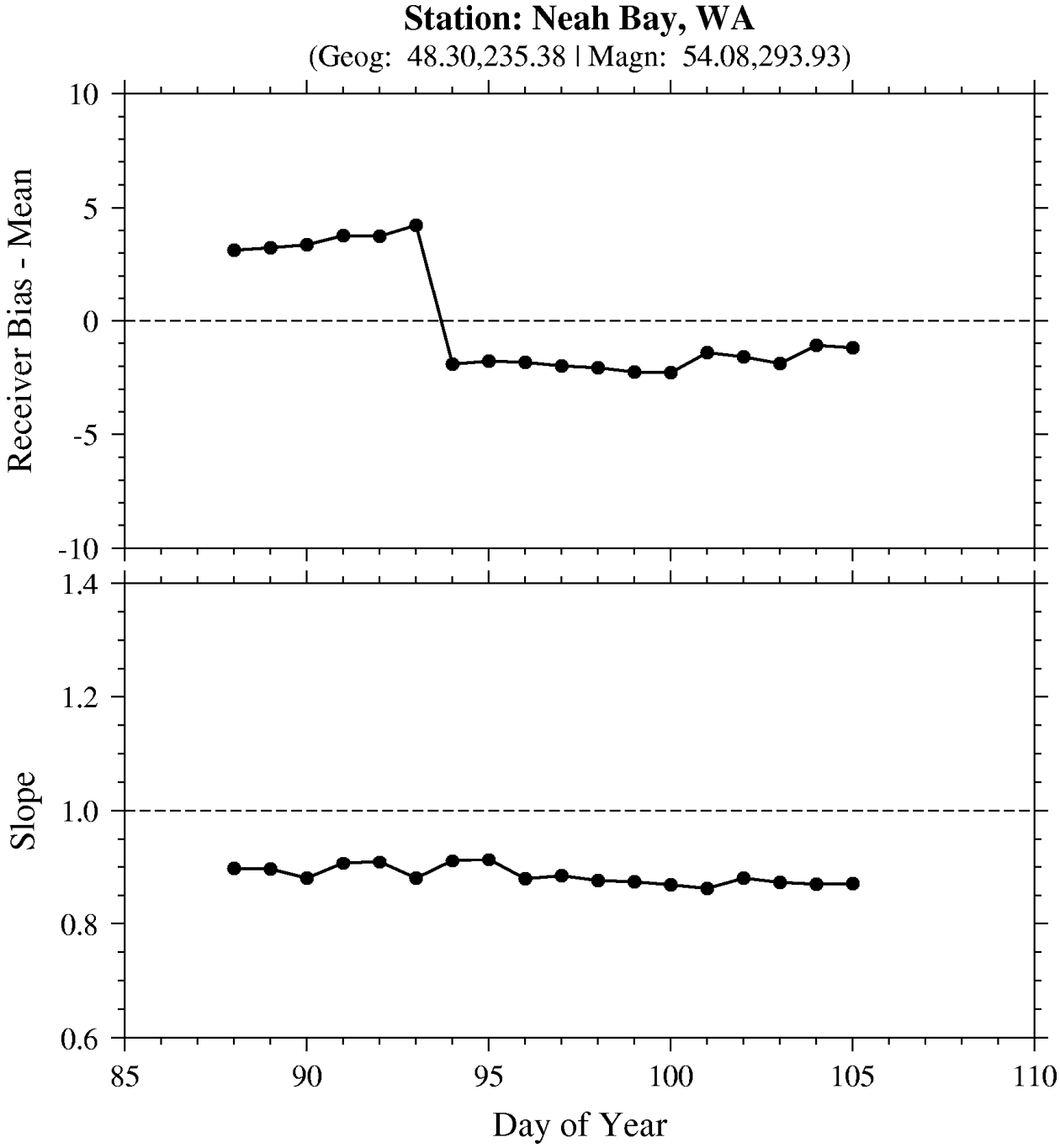

Figure F8. Example of an individual station plot of receiver bias and slope as derived from fitting the station's biases to the AIUB biases.

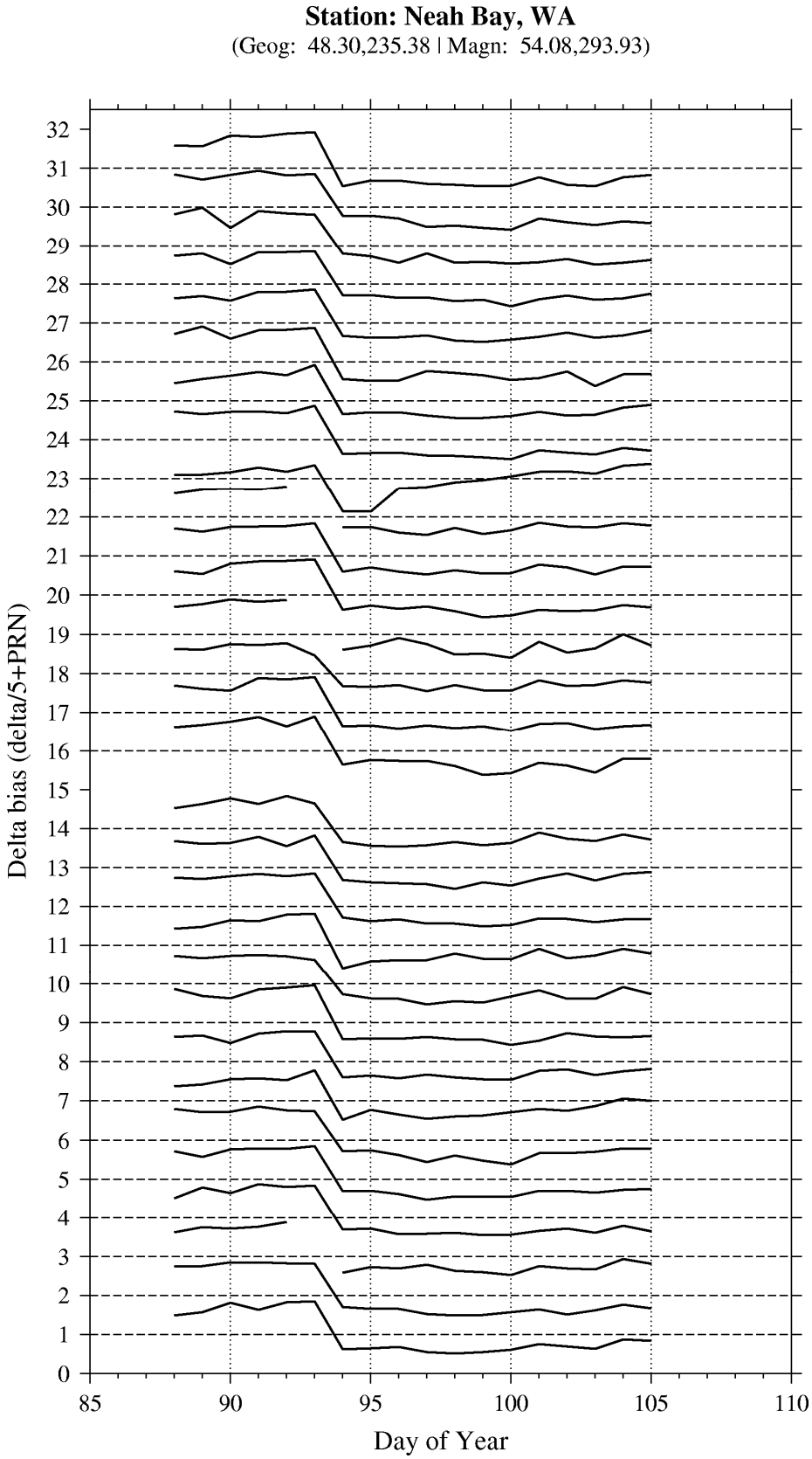

Figure F9. Example of an individual station plot of the variation of satellite+receiver biases with time.

Appendix G
Report on Research by Dr. Spencer Kuo

The following report was provided by Dr. Spencer Kuo, describing work he completed as a consultant to NWRA on this contract. Note that further details of the reported work can be found in the publications with Dr. Kuo as author or co-author in Section 4.

G1. Introduction

Several prominent issues relevant to the applications of the HAARP heating facility at Gakona, Alaska were addressed. Specifically, the topics of research included 1) Extremely/very low frequency (ELF/VLF) wave generation, generation mechanisms, and locating the electrojet source region, 2) precipitation of magnetospheric energetic electrons by whistler waves, which may be generated by the HAARP HF heater, 3) parametric instabilities and cascades of Langmuir waves and upper hybrid waves, which produce energetic electrons responsible for airglow enhancements, and 4) filamentation instability exciting large-scale field-aligned density irregularities and geomagnetic micropulsations. Most of the finished works have been published in journal articles.

G2. Extremely/Very Low Frequency (ELF/VLF) Wave Generation

The conductivity of the polar electrojet can be modulated temporally, through Ohmic heating by power-modulated HF heating waves, to set up the ionospheric antenna current for radiation. The dependency of the radiation intensity of this virtual ionospheric antenna on the HF wave modulation frequency has been measured in HAARP heating experiments. The field intensity of the ELF wave is shown to be affected strongly by the near field effect (for the modulation frequency $f_1 < 50$ Hz) and cavity resonance effect (for $f_1 \sim 2$ kHz). When the two effects are included in the numerical model, the experimentally measured frequency dependency of the radiation intensity, shown in Figure G1, can be reproduced numerically. On the other hand, the experimental results have validated the numerical model on ELF wave generation by the HF modulated electrojet.

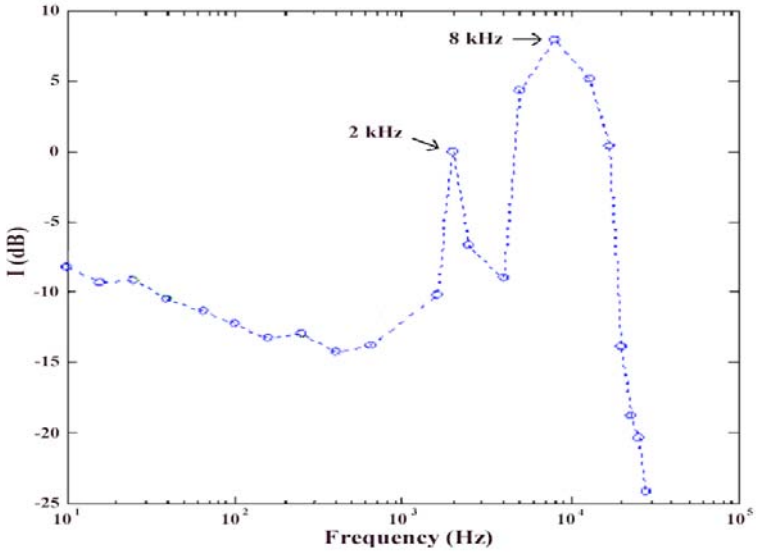

Figure G1. Frequency dependency of ELF/VLF radiation intensity; rectangular wave modulation scheme was used in the experiments.

Experiments using the intensity-modulated HF heating waves to interact with electrojet currents for the generation of VLF waves were also conducted. An unexpected large increasing rate from 4 to 8 kHz in the frequency dependency of the VLF radiation intensity, shown in Figure G1, was observed. The peak value at 8 kHz was intense (about 7.5 dB above that of the 2 kHz signal used as a marker) and the wave intensity from 5 to 17 kHz appeared to be abnormally high (i.e., stronger than that at 2 kHz). In the experiments, we also observed the enhancement of spread-E irregularities at electrojet current altitudes due to the amplitude-modulated heater wave. These results and theoretical analyses suggest that temporally modulated electrojet currents mix with heater wave-excited density irregularities to form whistler mode currents, which generate VLF whistler waves directly with much larger intensities and better directivity than a Hertzian dipole can.

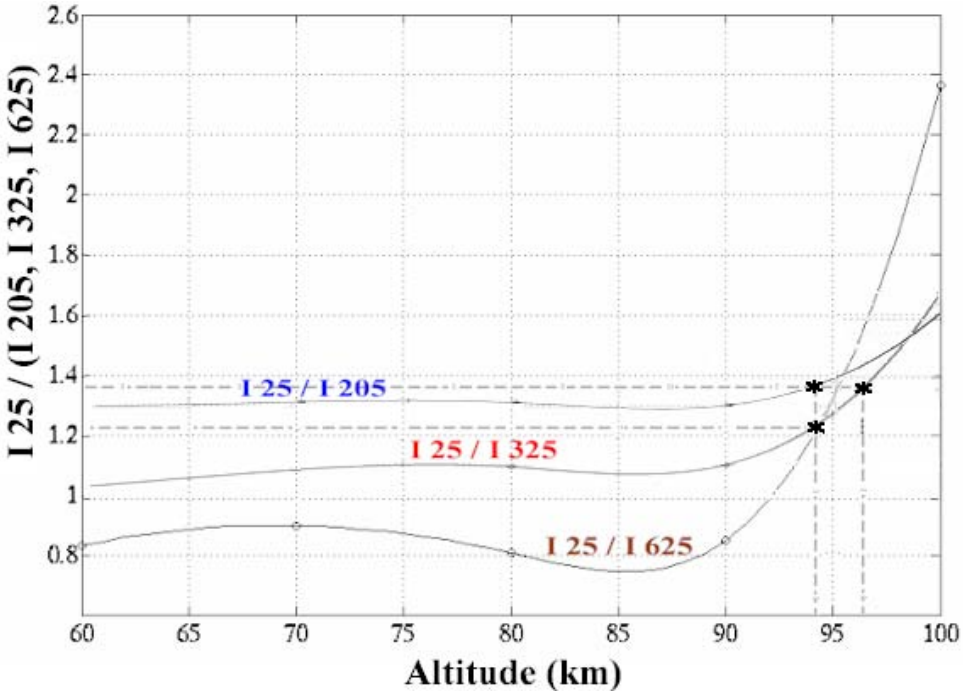

Figure G2. Radiation intensity ratios (I25/I205, I25/I325, and I25/I625) versus altitude of ELF source in the electrojet current, The experimental measurements at the three ratios are marked by "*" on the corresponding plots.

The numerical model on ELF wave generation can be used to determine the altitude dependency of a ratio of the ELF radiation intensities at two different frequencies. With the aid of the numerical plot on the altitude dependency of an intensity ratio, the experimentally measured single value of a similar ratio can provide unambiguous information on the height of the electrojet contributing to the ELF radiation. The numerical plots of three independent intensity ratios (25 Hz/205 Hz, 25 Hz/325 Hz, and 25 Hz/625 Hz) are presented in Figure G2; these plots are used to demonstrate this new diagnostic technique. Each ratio of the measured ELF radiation intensities is also marked on the corresponding plot, with the same pair of frequencies, by a symbol "*****". The location of this mark is determined by the intersection point of a horizontal dashed line, determined by the measured ratio, and the plot. The altitude of the source region is then found from the position of this marked point on the horizontal axis. Ideally, the three plots should result to a same height. In reality, various errors in the experimental

measurements and in the parameters used in the simulations can cause some variations. Indeed, as seen in Figure G2, the determined source region is at an altitude approximately between 94 Km and 97 Km from the ground level. However, the range of uncertainty is relatively small, demonstrating the capacity of this diagnostic technique.

G3. Mitigation of Energetic Electrons in the Magnetosphere

An optimal approach reducing the population of MeV electrons in the magnetosphere has been explored. It invokes a double resonance condition; whistler wave is simultaneously in cyclotron resonance with keV and MeV electrons. Thus, the injected whistler waves can first be amplified by the background keV electrons via loss-cone negative mass instability to become effective in precipitating MeV electrons via cyclotron resonance elevated chaotic scattering.

The theory describing the amplification of whistler wave by (tens of keV) energetic electrons in the magnetosphere through loss-cone negative mass instability is formulated. The numerical results, presented in Figure G3a, show that a small amplitude whistler wave can be amplified by more than 25 dB. The amplification factor reduces only about 10 dB with a 30-dB increase of the initial wave intensity. As the wave field exceeds the threshold for the commencement of chaos, cyclotron resonance-enhanced chaotic scattering can precipitate deeply trapped MeV electrons into loss cones. The numerical results, presented in Figure G3b, demonstrate that a 1.5 MeV electron can be scattered from an initial pitch angle of 86.5^0 to a pitch angle $<50^0$ by a whistler wave with the magnetic field amplitude of 0.08% of the background magnetic field, which is about 20 times smaller than that without invoking cyclotron resonance. This percentage converts to about 3100 pT at L=2, and 200 pT at L=5, which reduce to 550 pT and 36 pT, respectively, after taking advantage of the 15-dB gain.

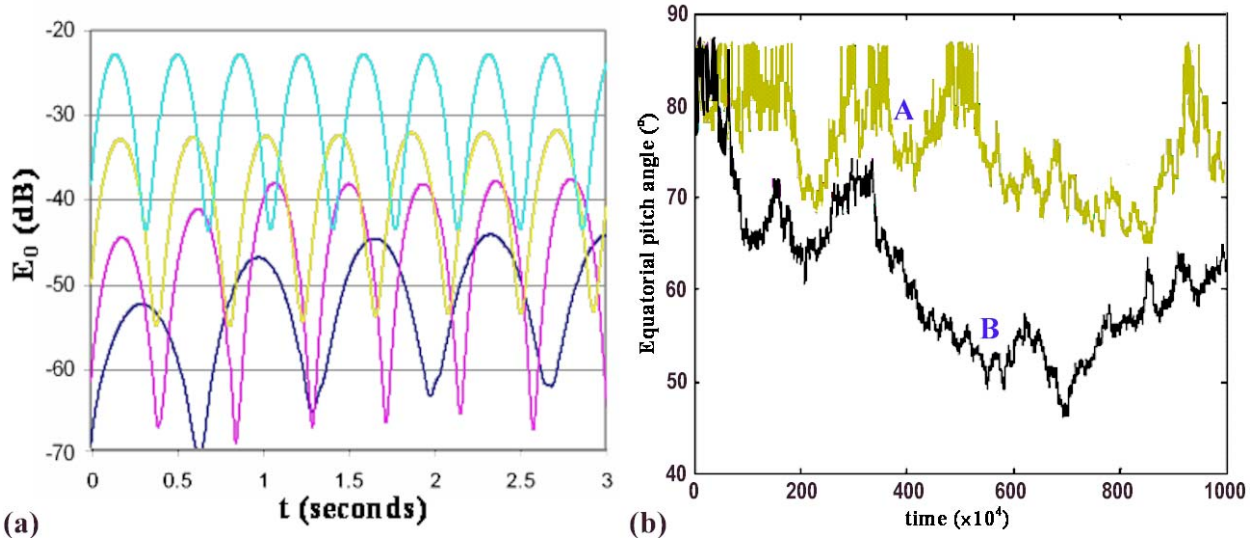

Figure G3. (a) Wave amplitude versus time for four different incident wave intensities and (b) temporal evolution of the pitch angle of a 1.5 MeV electron interacting with a whistler wave at Doppler shifted cyclotron resonance. Plots A and B correspond to wave magnetic field B1 = 7 ´ 10-4 B0 and 8.1 ´ 10-4 B0 cases, respectively.

G4. Parametric Instabilities and Cascades of Langmuir Waves

Parametric instability, which produces cascade spectra of HF enhanced plasma lines (HFPLs) in HAARP HF heating experiments, is studied. In each cascade, a Langmuir mother wave decays into a Langmuir daughter wave and an ion acoustic wave; The Langmuir daughter appears to be an HFPL at consecutively decreasing altitudes. Thus, the cascade lines in the HFPLs spread over a range of altitude, and the threshold pump field in each cascade is increased by the additional propagation loss of the Langmuir mother wave. The dominant factors, which determine the number of cascade lines in the HFPLs, include the ion-to-electron temperature ratio, T_i/T_e, the background plasma inhomogeneity scale length, and the heating wave field intensity.

The ratio T_e/T_i (= η) depends on the HF heating power (i.e., $\propto E_p^2$), as well as the operating mode of the HF heater. Assuming that the HF heater is operated at a cw mode, electron heating is expected and is modeled by a function $\eta(E_p) = 1 + 1.5\times[(E_p - 0.5)/4.5]^2$. Using this heating model, this function $N(E_p; \eta(E_p))$ is plotted in Figure G4. As shown, the first cascade can happen only when $E_p > 0.8$ V/m. To achieve two cascades, E_p has to exceed 1.8 V/m. As the heating power increases, the electron heating gives a positive feedback to further increase the number of cascade lines in the HFPLs. At the maximum heating power of 1 GW ERP (i.e., $E_p \sim 3$ V/m), 4 discrete cascade lines are expected to appear in the spectrum of HFPLs, which have a bandwidth exceeding 40 kHz. These lines spread in altitude over a 0.5-km range. If the HF heater is operated at low duty cycle pulsed mode, electron heating is insignificant even at a very high power case. Thus, $\eta \sim 1$, and $N_0 < 3$, even in the maximum power case (i.e., $E_p \sim 3$ V/m).

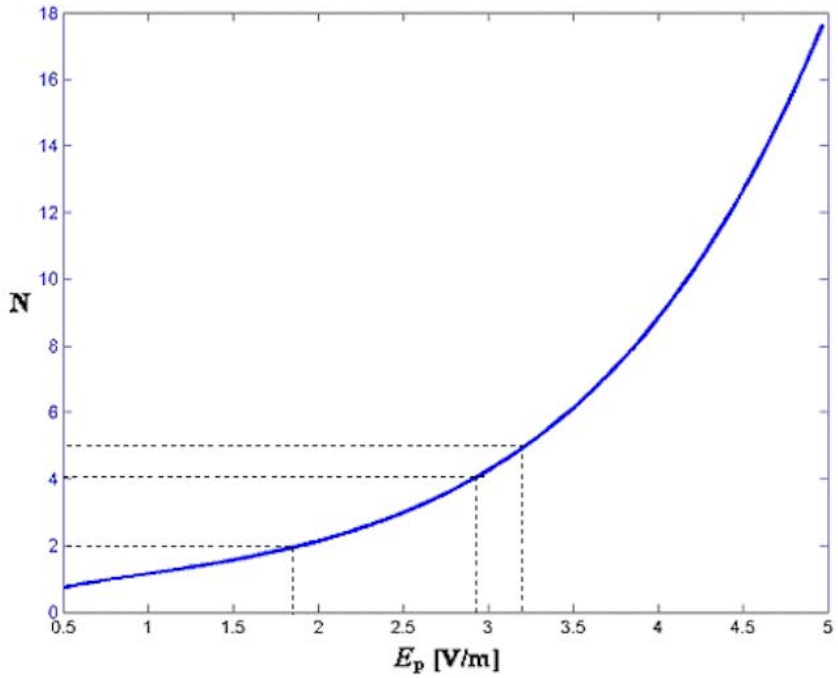

Figure G4. The number of the cascade lines N0 = Integer (N) in the HFPLs as a function of the heating wave amplitude Ep, for h(Ep) = 1 + 1.5´[(Ep –0.5)/4.5]2.

G5. Filamentation Instability Exciting Large-scale Field-aligned Density Irregularites and Geomagnetic Micropulsations

The generation of large-scale density irregularities by the filamentation instability near the HF reflection height was evidenced by the variation of the reflection height of the sounding waves in the frequency region around the HF heater frequency. Significant anomalous absorption (i.e., reducing the backscattering) of the sounding waves by the generated density irregularities caused the return trace of the sounding waves in the ionogram to disappear. From UTC 22:00 to 23:00, heater wave frequency was 4.5 MHz. As shown in Figure G5a, the return of the sounding waves recorded in the ionogram from 4.4 to 4.6 MHz was reduced considerably. After UTC 23:00, the heater frequency was switched to 2.7 MHz, the return of the sounding waves reappeared in the ionogram. Similarly, as shown in Figure G5b, the return trace from 2.5 to 3 MHz in the ionogram disappeared during the period from 23:00 to 01:00 UTC when the heater was run at 2.7 MHz. Again, one could see that the return trace reappeared after the heater was turned off.

Moreover, as shown in Figure G5c, the magnetic field variations in D and Z directions were recorded by the fluxgate magnetometer during the HF heater on period. These results presented in Figure G5, showing the simultaneous generation of large-scale density irregularities and geomagnetic field fluctuations, evidence the excitation of filamentation instability.

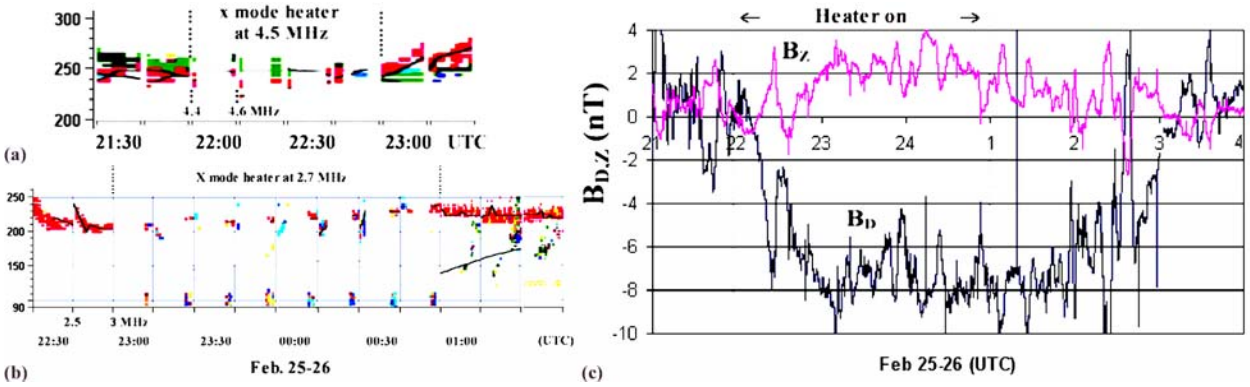

Figure G5. Composite ionograms showing the variation of the reflection height of the sounding waves from (a) 4.4 to 4.6 MHz and (b) 2.5 to 3 MHz every 15 minutes. The sounding waves appeared to be anomalously absorbed when the x mode HF heater at 4.5/2.7 MHz was turned on; (c) magnetic field variations in D and Z directions recorded by the fluxgate magnetometer.

References

Al'pert, Ya. L., F. F. Dobryankova, E. F. Chudesenko, and B. S. Shapior, Some results of a determination of the electron content in the outer region of the ionosphere from observations of the radio signals received from the first earth satellite, *Uspekhi Fiz. Nauk., 65,* 161, 1958.

Andreasen, A. M., J. Begenesich, E. Fremouw, E. Holland, A. J. Mazzella, Jr., J. Ostergaard, J. Rasmussen, J. A. Secan, A. L. Snyder, Ionospheric Measurements in the Wake of Solar Maximum, Final Report, *AFRL-VS-HA-TS-2004-1125,* Air Force Research Laboratory, Hanscom AFB, MA, 2004.

Bishop. G. J., D. O. Eyring, K. D. Scro, S. Deissner, D. J. Della-Rose, W. Cade, N. Ceaglio, and M. Collello, Air Force Ionospheric Measuring System supports global monitoring and mitigation of effects on AF systems, *Proceedings of ION GPS-94*, The Institute of Navigation, Washington, DC, 1994.

Bishop, G.J., A.J. Mazzella, and E.A. Holland, Self-Calibration of Pseudorange Errors by GPS Two-Frequency Receivers, *Proceedings of 1995 National Technical Meeting*, The Institute of Navigation, Washington, D.C., January 1995.

Bishop, F. J., J. A. Secan, and S. Delay, GPS TEC and the Plasmasphere, Some Observations and Uncertainties, presented at the 12th International Ionospheric Effects Symposium (IES 2008), Alexandria, VA, 2008.

Damon, T., and F. R. Hartranft, *Ionospheric Electron Density Profile Model, Tech. Memo. 70-3,* USAF Air Weather Service, 4th Weather Wing, Ent AFB, CO, July 1970.

Flattery, T. W., and A. C. Ramsay, Derivation of Total Electron Content for Real-Time Global Applications, in *Effect of the Ionosphere on Space Systems and Communications*, US GPO, Springfield, VA, 1975.

Fremouw, E.J., J. A. Secan, and B. M. Howe, "Application of Stochastic Inverse Theory to Ionospheric Tomography," *Rad. Sci.* **27** (5), 721-732, Sept,-Oct. 1992.

Fremouw, E.J., J. A. Secan, R.M. Bussey, and B. M. Howe, "A Status Report on Applying Discrete Inverse Theory to Ionospheric Tomography," *Int. J. Imaging Syst. & Tech.* **5** (2), 97-105, Sept,-Summer 1994.

Fridman, S. V. and L. J. Nickisch, Generalization of ionospheric tomography on diverse data sources: Reconstruction of the three-dimensional ionosphere from simultaneous vertical ionograms, backscatter ionograms, and total electron content data, *Radio Science, Vol. 36*, Number 5, September-October 2001.

Fridman, S. V., L. J. Nickisch, Mark Aiello, and M. A. Hausman, Real-time reconstruction of the three-dimensional ionosphere using data from a network of GPS receivers, *Radio Science, 41, RS5S12,* doi:10.1029/2005RS003341, 2006.

Houpis, H. L. F. and L. J. Nickisch, An ionospheric propagation and prediction method for low latitudes and mid-latitudes, *Radio Science*, Vol. 26, No. 4, pp. 1049-1057, July-August 1991.

Kennedy, E. J., J. S. Secan, and A. L. Snyder, Report on the HAARP 2008 Winter Campaign Focusing on Artificial Ionospheric Irregularities and Optical Emissions, Scientific Report #3, *AFRL-RV-HA-TR-2009-1024*, Air Force Research Laboratory, Hanscom AFB, MA, 2008.

Knepp, D. L., Multiple phase-screen calculation of the temporal behavior of stochastic waves, *Proc. IEEE*, Vol. 71, No. 6, pp. 722-737, June 1983.

Knepp, D. L. and H. L. F. Houpis, ALTAIR VHF/UHF Observations of Multipath and Backscatter Enhancement, *IEEE Transactions on Antennas and Propagation*, Vol. 39, No. 4, pp. 528-534, April 1991.

Knepp, D. L. and H. L. F. Houpis, , Kwajalein 1988 Propagation Effects Experiment Assessment and Results, Defense Nuclear Agency, DNA-TR-91-180, December 1992.

Lauer, Carl, L. J. Nickisch, and William Wortman, Prediction of over-the-horizon radar clutter using the clutter effects model, *Radio Science, Vol. 33*, Number 4, July-August 1998.

Lunt, N., L. Kersley, G. J. Bishop, A. J. Mazzella, and G. J. Bailey, The effect of the protonosphere on the estimation of GPS TEC: Validation using the SUPIM model, *Radio Sci., 34*, 1261, 1999.

Mazella, A. J. Jr., E. A. Holland, A. M. Andreasen, C. C. Andreasen, G. S. Rao, and G. J. Bishop, Autonomous estimation of plasmasphere content using GPS measurements, *Radio Sci., 37*, 1092, 2002.

Medillo, M., and J. A. Klobuchar, Investigations of the ionospheric *F* region using multistation total electron content observations, *J. Geophys. Res., 80*, 643, 1975.

Milikh, G., A. Gurevich, K. Zybin, and J. Secan, Perturbations of GPS signals by the ionospheric irregularities generated due to HF-heating at triple of electron gyrofrequency, submitted to *Geophys. Res. Lett.*, 2008.

Nickisch, L. J., Non-uniform motion and extended media effects on the mutual coherence function: An analytic solution for spaced frequency, position, and time,' *Radio Science*, Vol. 27, No. 1, pp. 9-22, Jan-Feb 1992.

Nickisch, L. J., Sergey V. Fridman, Mark A. Hausman, and James A. Secan, Ionospheric Effects Mitigation for Radar Systems Using GPS Ionospheric Inversion (GPSII), *AFRL Technical Report AFRL-VS-HA-TR-2007-1064*, 1 December 2006.

Rao, S., *Plasmaspheric and Enhanced Ionospheric Total Electron Content Monitoring, NWRA-BeCR-04-R286, AFRL-VS-HA-TS-2005-1043*, NorthWest Research Associates, Inc., Redmond, WA, 2004.

Rao, S., and A. J. Mazzella, Jr., *Plasmaspheric and Enhanced Ionospheric Total Electron Content Monitoring, NWRA-BELL-07-R364,* Final Report for SBIR Phase II Contract FA8718-05-C-0026, NorthWest Reseach Associates, Inc., Redmond, WA, 2007.

Secan, J. A., *WBMOD Ionospheric Scintillation Model, An Abbreviated User's Guide (Version 15), NWRA-CR-94-R127/R6,* NorthWest Research Associates, Inc., Bellevue, WA, 30 September 2004.

Secan, J. A., *Comparison of the WBMOD Ionospheric Scintillation Model to Scintillation Observations at Gakona, Alaska, NWRA-BELL-05-R311,* NorthWest Research Associates, Inc., Redmond, WA, 2005.

Secan, J. A., and E. J. Fremouw, TEC and Scintillation Observations During HAARP Daytime Operations, poster presented at the 12th Annual Ionospheric Interactions Workshop, Santa Fe, NM, April 2006.

Secan, J. A., E. J. Fremouw, A. J. Mazzella, Jr., J. Rasmussen, A. L. Snyder, *Investigation of Plasma Phenomena in the Ionosphere Under Natural Conditions and Under Conditions Artificially Perturbed by HAARP, AFRL-VS-HA-TR-2005-1207,* Air Force Research Laboratory, Hanscom AFB, MA, 17 August 2005.

Titheridge, J. E., Determination of ionospheric electron content from the Faraday rotation of geostationay satellite signals, *Planet. Space Sci., 20,* 353, 1972.

List of Symbols, Abbreviations, and Acronyms

3D	Three dimensional
AEU	Antenna Element Unit
AFB	Air Force Base
AFCRL	Air Force Cambridge Research Laboratory (now AFRL)
AFIT	Air Force Institute of Technology
AFRL	Air Force Research Laboratory
AFWA	Air Force Weather Agency
AFS	Air Force Station
AK	Alaska
ALTAIR	ARPA Long-Range Tracking and Instrumentation Radar
AMISR	Advanced Modular Incoherent Scatter Radar
APTI	Advanced Power Technology, Inc.
ARPA	Advanced Research Projects Agency
AWS	Air Weather Service (now AFWA)
BI	Backscatter Ionogram
BMEWS	Ballistic Missile Early Warning Radar
cal/val	Calibration and Validation
CLEM	Clutter Effects Model
COSMOS	Designator for a certain class of Russian satellites
CREDO	Coordinate Registration Enhancement by Dynamic Optimization
DF	Direction Finding
DIDBase	Digital Ionogram Data Base
DMSP	Defense Meteorological Satellite Program
DSTO	Defence Science Technology Organisation
EBI	Elevation Backscatter Ionogram
ELDT	Early Launch Detection and Tracking
ELF	Extremely Low Frequency
EOFs	Empirical Orthonormal Functions
E_s	Sporadic-E ionosphere layer
eV	Electron volt
f_oF2	Critical frequency (O-mode) of the F2 layer (MHz)
FAIM	Fully Analytic Ionosphere Model
FDOA	Frequency Difference of Arrival

FIRIC	FAIM-IRI-Chapman ionosphere model
FFT	Fast Fourier transform
GAIM	Global Assimilative Ionospheric Model (JPL version)
GAIM	Global Assimilation of Ionospheric Measurements (Utah State version)
GIOS	NWRA GPS Ionospheric Observing System software
GPS	Global Positioning System
GPSII	GPS Ionospheric Inversion
HAARP	High-frequency Active Auroral Research Program
HF	High Frequency
I&Q	In-phase and quadrature-phase
IMS	Ionospheric Measuring System
IPP	Ionospheric Penetration Point
IPT	Integrated Product Team
IRI	International Reference Ionosphere model
IRI	Ionospheric Research Instrument (located at HAARP facility)
ITS	Ionospheric Tomography System
JPL	Jet Propulsion Laboratory
K	Kelvin (degrees)
kHz	Kilohertz (10^3 cycles/seconds)
kW	Kilowatt (10^3 watts)
L-band	Radio frequency band covering 1.0 GHz to 2.0 GHz (nominal)
LEO	Low earth orbit
MDA	Missile Defense Agency
MHz	Megahertz (10^6 cycles/seconds)
MIMO	Multiple Input Multiple Output
MPS	Multiple phase screen
NetCDF	Network Common Data Format
NexGen	Next Generation OTH radar
NIMS	Navy Ionospheric Monitoring System
NNSS	Navy Navigational Satellite System
NOAA	National Oceanic and Atmospheric Administration
NORAD	North American Aerospace Defense Command
NORTHCOM	US Northern Command
NRE	Northwest Research Engineering

NRL	Naval Research Laboratory
NTIA	National Telecommunications and Information Administration
NWRA	NorthWest Research Associates
O&M	Operations and Maintenance
OI	Oblique Ionogram
ONR	Office of Naval Research
OTH, OTHR	Over-the-Horizon Radar
PC	Personal Computer
PCA	Polar Cap Absorption
PDM	Phase screen diffraction method
PDR	Powerful Diagnostic Radar
PSD	Power spectral density
PEAK	Propagation Effects Assessment – Kwajalein
PMFIC	Performance Monitoring, Fault Isolation, and Calibration
pot	Potentiometer
PRA	Photon Research Associates
PRN	Pseudo-Random Noise (GPS identification signature)
RCS	Radar cross section
RFP	Request for Proposal
RINEX	Receiver Independent Exchange (data format)
rms, RMS	root mean square
ROTHR	Relocatable Over-the-Horizon Radar
ROTHR-VA	Relocatable Over-the-Horizon Radar located in Virginia
S-band	Radio frequency band covering 2.0 GHz to 4.0 GHz (nominal)
SAO	Standard Archiving Output
SCORE	Self-Calibration of Range Errors
SCORPION	SCORE for Plasmasphere and Ionosphere
SDC	Spread-Doppler Clutter
SEE	Stimulated Electromagnetic Emission
SkyLOS	Skywave Line of Sight
SNR	Signal-to-noise ratio
SOW	Statement of Work
SPAWAR	Space and Naval Warfare Systems Center
sps	samples per second

SRII	SRI International
SSIES	Special Sensor for Ions, Electrons, and Ions (DMSP sensor package)
SSUSI	Special Sensor Ultraviolet Spectrographic Imager (DMSP sensor package)
SSN	Sunspot Number
SSPA	Solid state power amplifier
TAC	Technical Advisory Committee
TDOA	Time Difference of Arrival
TEC	Total Electron Content (el/m^2)
TECU	TEC unit ($1.0x10^{16}$ el/m^2)
TLE	Two-Line Element satellite ephemeris set
UEWR	Upgraded Early Warning Radar
UHF	Ultra High Frequency radio band (300 MHz – 3 GHz)
UK	United Kingdom
UML	University of Massachusetts at Lowell
UPS	Uninterruptible Power Source
UT	Universal Time
VI	Vertical Incidence
VHF	Very High Frequency radio band (30 MHz – 300 MHz)
VLF	Very Low Frequency radio band (3 kHz – 30 kHz)
VTEC	Vertical (or equivalent vertical) TEC (el/m^2)
VTRPE	Variable Terrain Radio Parabolic Equation
WARF	Wide Aperture Research Facility
WBMOD	WideBand MODel (NWRA ionospheric scintillation model)
WDLS	Weighted, Damped, Least-Squares
WSBI	Wide-Sweep Backscatter Ionogram
WSMR	White Sands Missile Range
σ_ϕ	Ionospheric phase scintillation index (radians)